博士論文

Nanoscale magnetic properties and spin-dependent transport in Ge-based ferromagnetic epitaxial films

(Geをベースとした強磁性エピタキシャル薄膜における ナノスケール磁気物性とスピン依存伝導)

平成 28 年 12 月 1 日提出
指導教員　大矢　忍　准教授

東京大学大学院工学系研究科
電気系工学専攻
37-147067
若林　勇希

Table of Contents

Chapter 1: Introduction and the purpose of this study

1. 1. Semiconductor Spintronics

Generally, electronic charges and spins are controlled separately. The electronic charges are utilized for semiconductor-based data processing devices, such as very large scale integration (VLSI), central processing unit (CPU), dynamic random access memory (DRAM), etc. Also, the electronic charges are utilized for optical devices, such as light emitting diode (LED) and semiconductor laser, in which interband or intraband transition of electron is used. On the other hand, the electronic spins are utilized for data storage devices, such as hard disc drives (HDDs), which are realized using nonvolatile hysteresis of the magnetization of ferromagnetic (FM) materials. Almost all computers are composed of both the high-frequency data processing components and the data mass-storage components. Although the electrons are utilized in both components, they have been developed independently for a long time.

In 1988, giant magneto-resistance (GMR) was discovered in FM metal / nonmagnetic metal multilayers by Fert *et al.*[1] and Grünberg *et al.*[2] independently. GMR was observed in multilayers composed of at least two FM layers separated by a nonmagnetic metal spacer layer. The resistance depends on the alignment of magnetization vectors of the FM layers, which means that the *charge transport* can be controlled by the direction of spins. This is the concept of spintronics. The GMR has been applied to a magnetic head of HDD and has dramatically extended the data storage capacity. The GMR device is thus a milestone of spintronics, and Fert and Grünberg received the Novel Prize in Physics in 2007.

The purpose of semiconductor spintoronics is realization of new functional devices, like a spin-metal-oxide-semiconductor field effect transistor (spin-MOSFET),[3,4] by utilizing the electronic charges and spins simultaneously. In a MOSFET, paramagnetic (PM) semiconductors are used as the source and drain electrodes, and a current flows in the semiconductor channel region. In the spin-MOSFET, FM materials are used as the source and drain electrodes, and a spin polarized current flows in the semiconductor channel region. The spin-MOSFET is expected to add novel functionalities required for low power consumption (e.g. non volatile data storage, reconfigurable logic, and power gating) to the conventional data processing semiconductor devices. To realize such semiconductor spintronic devices, FM materials which can be grown on existing semiconductors and have a high compatibility with the existing semiconductor technology are needed.

1. 2. Ge-based ferromagnetic epitaxial films; the ferromagnetic semiconductor $Ge_{1-x}Fe_x$ and the $Ge_{1-x}Mn_x$ granular films

The choice of a base semiconductor is important to develop semiconductor-based FM materials which can be grown on existing semiconductors and to realize semiconductor spintronic devices. In this study, Group-IV semiconductor Ge is selected as the base semiconductor. Ge has a diamond type single crystal structure. It can be epitaxially grown on Si substrates. Furthermore, both electron and hole have higher mobilities than those of Si. Therefore, it is expected to be a next-generation high performance semiconductor material, which has a high compatibility with mature Si technology.[5-7] There are two typical FM materials that can be epitaxially grown on Ge substrates; ferromagnetic semiconductors (FMSs) and granular films.

In FMSs, magnetic atoms substitute for a portion of the host atoms of the base semiconductor. They have the following features.

(1) High quality single crystals, which have a base semiconductor's crystal structure and can be epitaxially grown on the base semiconductor without any precipitates.

(2) The conductivity can be controlled by carrier doping.

Owing to these advantages, in the sight of device processing and integration, FMSs have a high compatibility with the current semiconductor technology. For real applications of the FMSs, following requirements exist.

(A) The Curie temperature (T_C) should be higher than room temperature.

(B) It should have a large spin polarization at the Fermi energy (E_F).

However, currently, no FMSs satisfy the above requirements.

Group-IV-based FMS $Ge_{1-x}Fe_x$ (GeFe) is expected to be an efficient spin injector and detector which are compatible with Si- and Ge-based devices, because it can be epitaxially grown on Si[8] and Ge[9] substrates without a disordered interfacial layer or formation of ferromagnetic intermetallic Fe-Ge precipitates (Fig. 1). One of the important characteristics of GeFe is that the conductivity can be controlled by boron (B) doping independently of the Fe concentration x (Fig. 2).[10] Therefore, when a spin current is injected from GeFe to a nonmagnetic semiconductor, we can avoid the conductivity mismatch problem and suppress the spin-flip scattering at the interface. However, the T_C value of GeFe is currently at the highest 170 K. Furthermore, detailed microscopic understanding of the ferromagnetism and the magnetization process in GeFe, which is vitally important for room-temperature applications, is lacking.[9,11,12] In addition, the presence of spin-polarized carriers at E_F in

GeFe has not been confirmed.

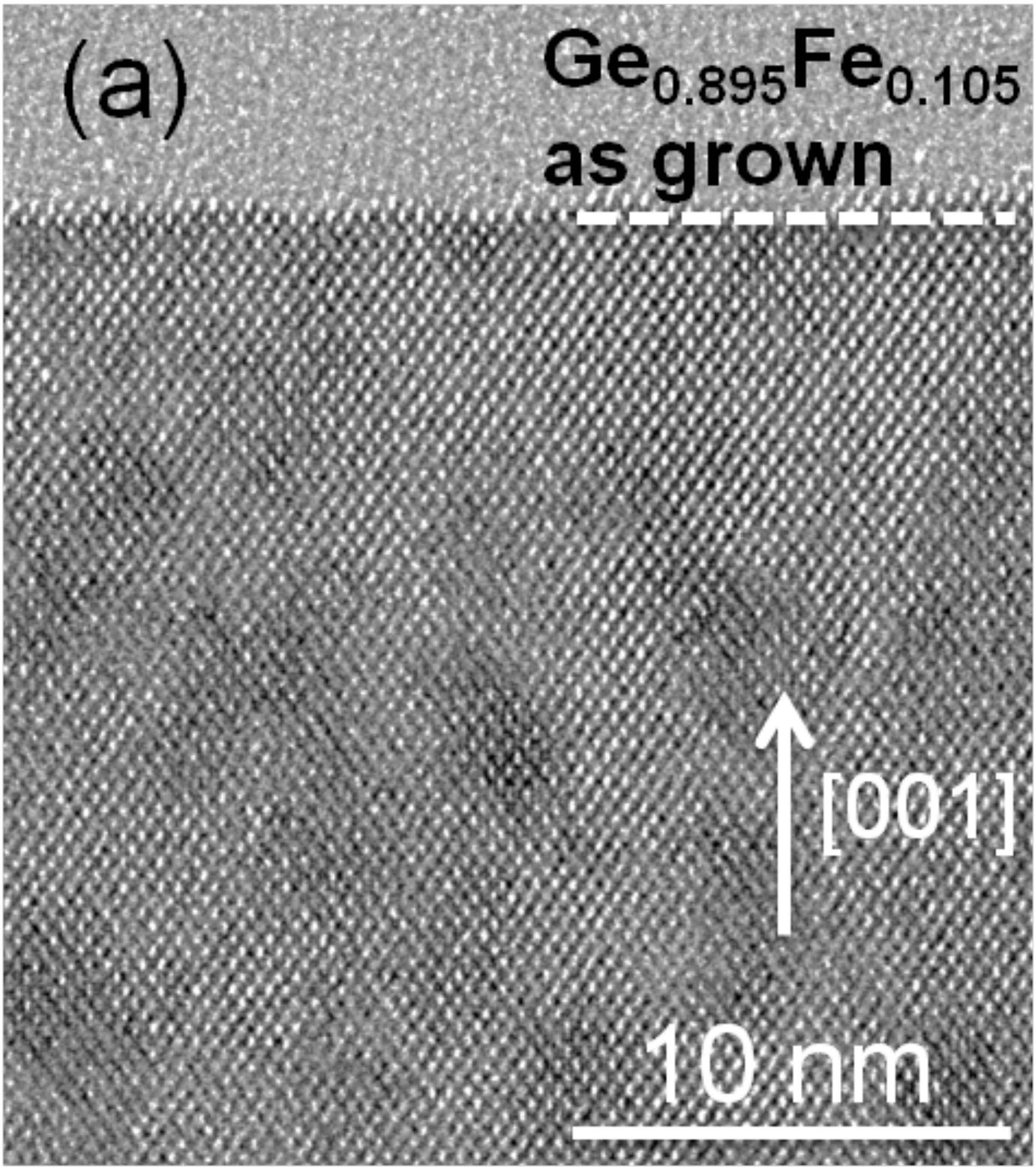

Fig. 1. High resolution transmission electron microscopy (HRTEM) lattice image projected along the Ge[110] axis of the $Ge_{0.895}Fe_{0.105}$ epitaxially grown on a Ge (001) substrate. [Y. K. Wakabayashi *et al.*, Physical Review B **90**, 205209 (2014).]

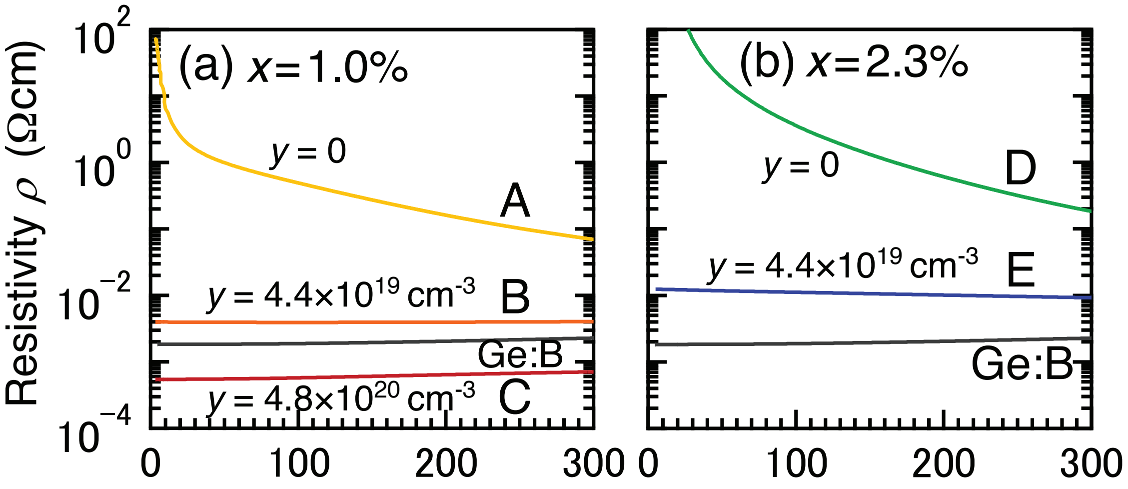

Fig. 2. (a),(b) Temperature dependence of the resistivity of the $Ge_{1-x}Fe_x$ films with the Fe concentration (a) x = 1.0% and (b) 2.3%, with or without boron doping. The boron doping concentrations y of the $Ge_{1-x}Fe_x$ films (x = 1.0%) are y = 4.4 × 10^{19} cm^{-3} (orange), 4.8 × 10^{20} cm^{-3} (red), and 0 (undoped, yellow), and those of the $Ge_{1-x}Fe_x$ films (x =2.3%) are y = 4.4 × 10^{19} cm^{-3} (blue) and 0 (undoped, green). The temperature dependence of boron-doped Ge at the B concentration of y = 4.4 × 10^{19} cm^{-3} on an SOI (001) substrate is also shown as a reference. [Y. Ban, Y. K. Wakabayashi *et al.*, AIP advances **4**, 097108 (2014).]

Another typical FM material that can be epitaxially grown on semiconductor substrates is ferromagnetic granular films. They are nanocomposite materials which have magnetic nanoparticles embedded in a nonmagnetic matrix. They show various large magnetoresistance (MR) effects such as GMR and magnetic field-dependent avalanche breakdown. Owing to these MR effects, they are expected to be a high sensitive magnetic sensor. In addition, they can be applied to a high density perpendicular magnetic recording medium because of their high stability of heat.

$Ge_{1-x}Mn_x$ (GeMn) granular thin films have attracted much interest for spintronic applications owing to their large positive MR, which can be as high as ~280% (under 5 T at 40 K) and to their compatibility with existing semiconductor technology.[13–21]

1. 3. Non-uniformity of magnetic atoms in Ge-based ferromagnetic epitaxial films

Non-uniformity of magnetic atoms in FMSs and granular films influences their physical properties, such as electronic structure, magnetization process, T_C, magneto-optical property, and spin-dependent transport, etc.[22] The non-uniformity of the magnetic atoms can be controlled by selecting appropriate growth conditions, layers' layout, and/or codoping.[22] For example, when the non-uniformity of the magnetic atoms in the FMS becomes larger than a threshold such as the solubility limit, second-phase magnetic precipitates appear in the matrix, namely, the FMS becomes a granular film. Thus, controlling the non-uniformity of magnetic atoms can be viewed as a new class of bottom-up approach to nanofabrication. To develop the spin-dependent functionality in the FMSs and granular films, understanding the correlation of the non-uniformity of the magnetic atoms with nanoscale magnetic properties and spin-dependent transports is necessary.

In the equilibrium phase diagram of the crystalline Fe-Ge system, there are several compounds, such as $FeGe_2$, FeGe (monoclinic, hexagonal, and cubic), Fe_6Ge, and Fe_3Ge (hexagonal and cubic).[23] The Fe content x of $Ge_{1-x}Fe_x$ films studied in this thesis is 6.5 and 10.5%. These values are in the range between those of Ge (0%) and $FeGe_2$ (33.3%), and we do not see any known phases in this region of x. Thus our GeFe films are a new material, which can be realized only at the non-equilibrium growth condition.[9] It is known that the GeFe films grown by low-temperature molecular-beam epitaxy (LT-MBE) have a diamond-type single crystal structure with a non-uniform distribution of Fe atoms and stacking-fault defects in locally high-Fe-concentration regions.[9] However, their relevance to the magnetic properties has not been clarified yet.

Previous studies of GeMn have suggested that the large MR is related to the nanoscale spinodal decomposition of GeMn into the FM metallic Mn-rich nanoparticles and the PM Mn-poor matrix.[14,15,19,20] However, the microscopic origin of the MR has not yet been clarified over the past decade since the first report of GeMn, although understanding the microscopic origin of the MR is vitally important for the development of spin-dependent functionality in granular films.

1. 4. Purpose of this study

Purpose of this study is understanding the correlation of the non-uniformity of the magnetic atoms with nanoscale magnetic properties and spin-dependent transports in the Group-IV-based FMS GeFe and the GeMn granular films. All the films studied in this thesis are epitaxially grown on Ge substrates by LT-MBE with various growth conditions. Comprehensive studies of the crystal structures, magnetic properties, electronic structures, and magnetotransport characteristics are carried out. We have also grown magnetic tunnel junctions (MTJs) composed of epitaxial $Fe/MgO/Ge_{0.935}Fe_{0.065}$ trilayer structure to examine the spin-dependent transports. The existence of the spin-polarized carriers at E_F in both Group-IV-based FMS GeFe and GeMn granular film is confirmed by the spin-dependent transport measurements.

Chapter 2: Principle of Measurements

2. 1. X-ray magnetic circular dichroism (XMCD)

In XMCD measurements,[24] we measure the difference of the absorption between right- and left- circularly polarized X-ray (Fig. 3). Figure 4 shows a schematic diagram of the relative transition probabilities between the 2*p* core levels and the 3*d* down-spin states of Fe. Here, relative transition probabilities between the 2*p* core levels and the 3*d* up-spin states of Fe are not shown for simplicity, because most of the 3*d* up-spin states are occupied in Fe atoms. The degeneracy of the 2*p* core levels is resolved by the spin-orbit interactions, which results in the two-fold degenerated $2p_{1/2}$ and the four-fold degenerated $2p_{3/2}$ levels. The magnetic moment of Fe reflects the difference of the occupancies between the up-spin states and down-spin states of the 3*d* levels. In XMCD, this difference of the occupancy is detected as the difference of the absorption between the right- and left- circularly polarized X-rays. XMCD has following large advantages. First, we can detect element-specific magnetic moments using 2*p*-3*d* absorption edges which depend on elements. Second, we can separately estimate orbital and spin magnetic moments using the XMCD sum rules. In addition, the sum of the absorptions is called X-ray absorption spectroscopy (XAS). Using XAS, we can estimate a valence of atoms.

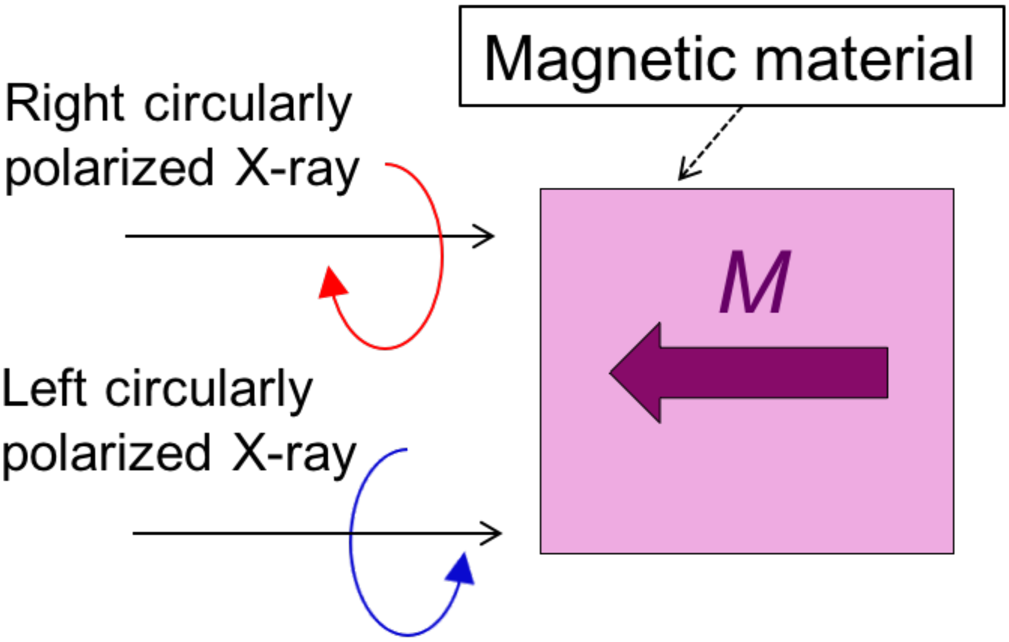

Fig. 3. Schematic structure of the XMCD measurements.

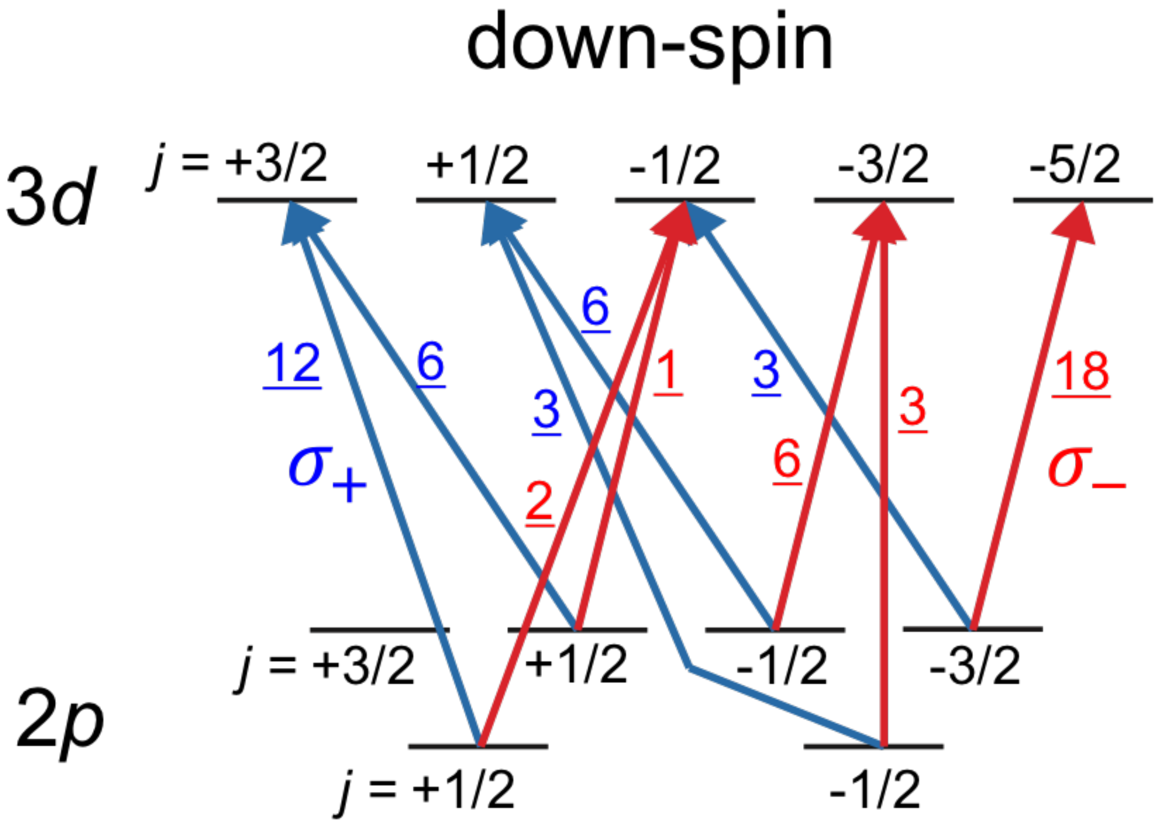

Fig. 4. Schematic diagram of the relative transition probabilities between the $2p$ core levels and the $3d$ down-spin states of Fe.

See the section 3.3 and 5.3 for detailed explanations of the XMCD sum rules and examples of its application.

2. 2. Angle resolved photoemission spectroscopy (ARPES)

Angle resolved photoemission spectroscopy (ARPES) is a powerful technique to observe the electronic structure of solids using the photoelectric effect.[25,26] Figure 5 shows the experimental configuration of the ARPES measurements. In the ARPES measurements, we detect numbers, kinetic energies, and the directions of the photoelectrons escaping from the sample surface when the X-ray is irradiated to the sample surface. In the ARPES measurements, we can observe the density of states and the band dispersion.

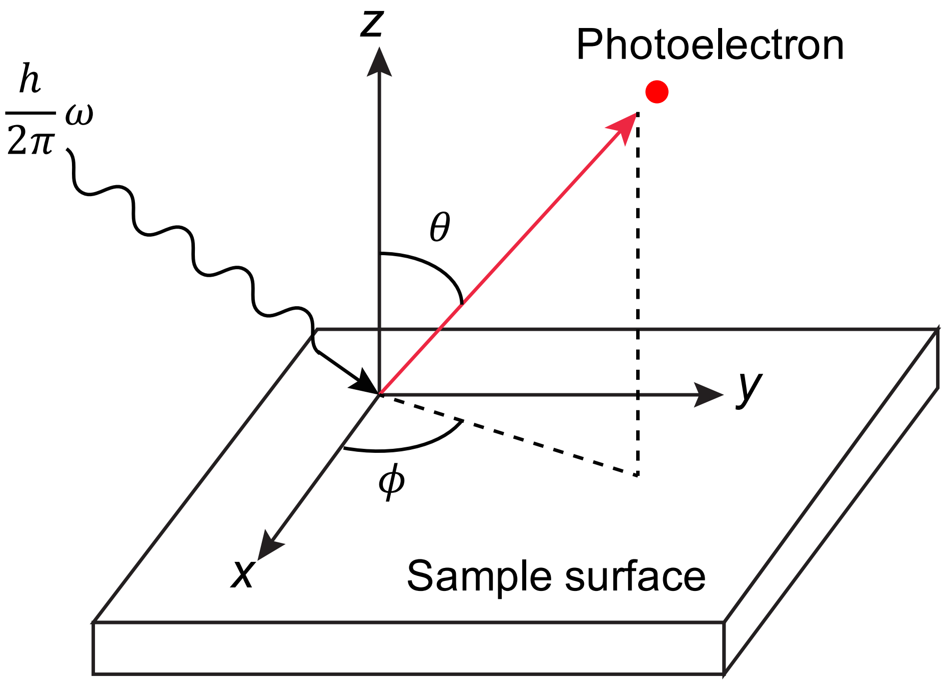

Fig. 5. Experimental configuration of the ARPES measurements. The red arrow represents the direction of the photoelectron escaped from the sample surface. The angle θ represents the polar angle between the normal line of the sample surface and the the direction of the photoelectron. The angle ϕ represents the azimuthal angle in the sample surface.

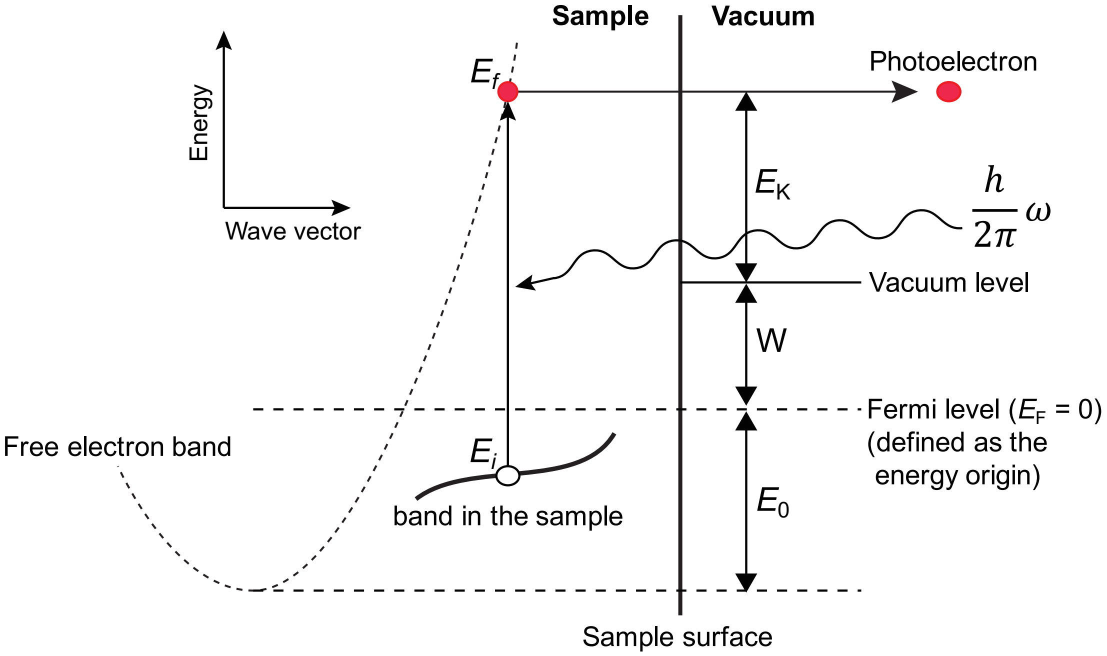

Fig. 6. Schematic illustration of the energy conservation in ARPES.

Figure 6 shows the schematic illustration of the energy conservation in ARPES. The principle of ARPES can be explained in accordance with Fig. 6.

The electron on the energy band in the sample is excited to the final state, whose energy is E_f, from the initial state, whose energy is E_i, by irradiating the X-ray with the photon energy of $(h/2\pi)\omega$. In this process, the following energy conservation is kept.

$$\frac{h}{2\pi}\omega = E_f - E_i. \tag{1}$$

We can view the electron at the final state to be a free electron. Here, E_0 is defined as the energy difference between the Fermi level (E_{F}) and the bottom of the energy band of the free electron. Here, E_{F} is defined as the energy origin. Thus, E_f is expressed as follows.

$$E_f = \frac{\hbar^2({k_\parallel}^2 + {k_\perp}^2)}{2m} - E_0, \tag{2}$$

where, $k_\perp$ and $k_\parallel$ represent the perpendicular and in-plane components of the wave number of the electron at the final state.

In addition, the following energy conservation between the electron at the final state and the photoelectron escaped from the surface is kept.

$$E_f = E_{\mathrm{K}} + W, \tag{3}$$

where, E_{K} and W represent the kinetic energy of the photoelectron escaped from the surface and the work function of the sample, respectively.

The perpendicular ($K_\perp$) and in-plane ($K_\parallel$) components of the wave number of the photoelectron escaped from the surface are expressed as follows.

$$K_\perp = \frac{\sqrt{2mE_{\mathrm{K}}}}{\hbar}\cos\theta, \tag{4}$$

$$K_\parallel = \frac{\sqrt{2mE_{\mathrm{K}}}}{\hbar}\sin\theta, \tag{5}$$

where, θ represents the polar angle shown in Fig. 5.

When the sample surface is flat, the in-plane component of the wave number does not change, e.g.

$$K_\parallel = k_\parallel, \tag{6}$$

By solving eqs. (1)-(6), we can obtain the following equations.

$$k_\parallel = \frac{\sqrt{2m\{E_i + \hbar\omega - W\}}}{\hbar}\sin\theta. \tag{7}$$

$$k_{\perp} = \frac{\sqrt{2m\{E_i + \hbar\omega - W\}\cos^2\theta + E_0 + W}}{\hbar}. \tag{8}$$

In addition, x and y components of the wave number of the electron at the final state are expressed as follow.

$$k_x = k_{\parallel} \cos\phi, \tag{9}$$

$$k_y = k_{\parallel} \sin\phi, \tag{10}$$

In the ARPES measurements, we observe θ, ϕ, and E_{K}. In addition, we obtain the W value by reference measurements typically for Au electrically contacting the sample. Thus, by using eqs. (1) and (3), we can obtain E_i. In addition, by using eqs. (7)-(10), we can determine the band dispersion of the sample. The E_0 value is treated as a fitting parameter in the ARPES measurements. In this thesis, the energy resolution of the ARPES measurements is estimated to be 170 meV. Note that the accuracy of the energy position of the E_{F} is much higher (typically ∼10 meV). This can be determined by the shape of the photoemission spectrum near E_{F} for Au.[27]

2. 3. Tunneling magnetoresistance (TMR)

MTJs are tunnel junctions composed of two FM electrodes and a insulating tunnel barrier.[28] TMR occurs in MTJs. The directions of the magnetizations of the two FM electrodes can be controlled separately by an external magnetic field or a spin transfer torque. When the magnetizations are aligned parallel, the tunneling probability of the electrons is higher than that when the magnetizations are aligned antiparallel. Therefore, MTJs can be switched between high and low resistance states. The TMR is applied to the magnetic head of the HDD and the magnetoresistive random access memory (MRAM). Observation of the TMR in MTJ is direct evidence of a finite spin polarization of the FM electrodes because the TMR originates from the spin polarization of the FM electrodes as explained below.

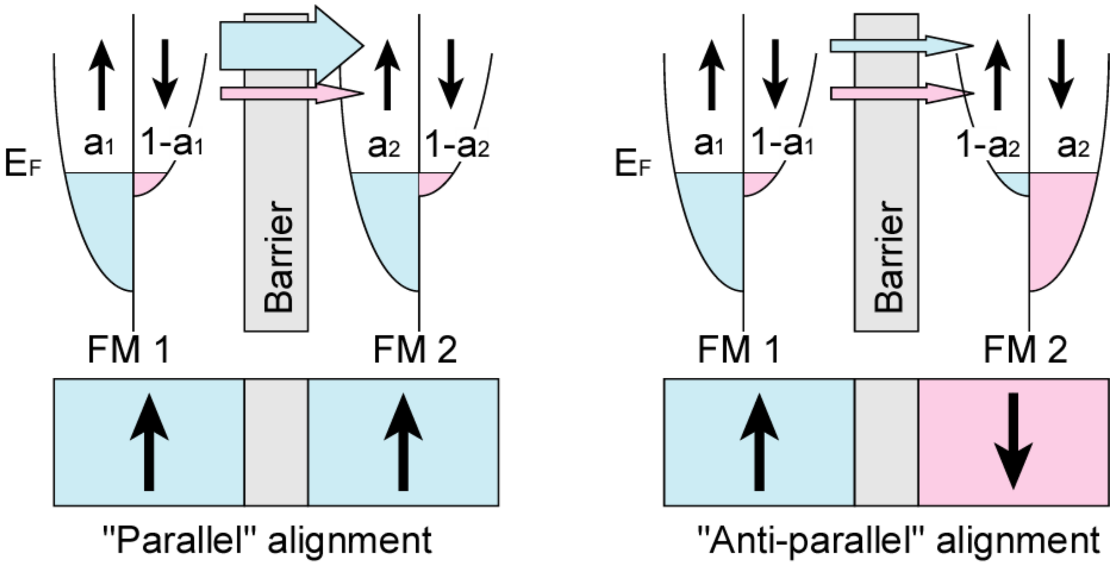

Fig. 7. Schematic illustration of the spin-dependent tunneling process at the parallel alignment and antiparallel alignment of the two FM electrodes in the MTJ, where carriers tunnel from FM1 electorde to FM2 electrode through the tunnel barrier, and a_1 and a_2 represent the existence probability of the majority spin at the E_F for the FM1 and FM2, respectively.

Assuming that carriers tunnel without spin flip, up-spin carriers of one FM layer are allowed to tunnel only into the up-spin state of the other FM layer, and down-spin carriers are allowed to tunnel only into the down-spin state of the other FM layer. The tunneling probability of the up-spin (down-spin) carriers depends on the density of states (DOS) of the up-spin (down-spin) band of both FM layers. Figure 7 shows the schematic illustrations of the spin-dependent tunneling process in the parallel magnetization alignment and antiparallel magnetization alignment of the two FM electrodes in the MTJ, where carriers tunnel from FM1 electorde to FM2 electrode through the tunnel barrier, and a_1 and a_2 represent the ratio of the density of the majority spin at the E_F to that of the sum of the majority and minority spins for FM1 and FM2, respectively. The tunnel conductances of carriers in parallel magnetization (G_P) and anti-parallel magnetization (G_{AP}) are described as follows.

$$G_{\mathrm{P}} \propto a_1 a_2 + (1 - a_1)(1 - a_2). \tag{11}$$

$$G_{\mathrm{AP}} \propto a_1(1 - a_2) + (1 - a_1)a_2. \tag{12}$$

Using the resistance in the parallel magnetization (R_P) and the one of anti-parallel magnetization (R_{AP}), the TMR ratio is given by the following equation,

$$TMR = \frac{R_{\mathrm{AP}} - R_{\mathrm{P}}}{R_{\mathrm{P}}} = \frac{G_{\mathrm{P}} - G_{\mathrm{AP}}}{G_{\mathrm{AP}}}, \tag{13}$$

where $R = 1/G$ is used. Defining the spin polarization P as $P_{1,2} = a_{1,2} - (1 - a_{1,2}) = 2a_{1,2} - 1$, Eq. (13) is transformed as,

$$TMR = \frac{2P_1P_2}{1-P_1P_2}. \tag{14}$$

Eq. (14) means that the FM electrodes with a high spin polarization will give a high TMR ratio.

Chapter 3: Crystal Structure, Annealing Effect, Magnetic Properties, and Electronic Structure of the Ferromagnetic Semiconductor $Ge_{1-x}Fe_x$

3. 1. Crystal structure and magnetic properties

In this section, we present the growth temperature (T_S) dependence of T_C, the lattice constant, the non-uniformity of Fe atoms, and the stacking-fault defects of GeFe films, that are investigated by magnetic circular dichroism (MCD), X-ray diffraction (XRD), high-resolution transmission electron microscopy (HRTEM), and spatially resolved transmission electron diffraction (TED) combined with energy dispersive X-ray spectroscopy (EDX). Also, we employ channeling Rutherford backscattering (c-RBS) and channeling particle induced X-ray emission (c-PIXE) characterizations to investigate the location of the Fe atoms in the GeFe lattice.[29]

We have epitaxially grown $Ge_{1-x}Fe_x$ thin films with the Fe concentration x of 0.065 and 0.105 on Ge(001) substrates by LT-MBE. Figure 8(a) shows the schematic structure of the samples. The growth process is described as follows. After the Ge(001) substrate was chemically cleaned and its surface was hydrogen-terminated by buffered HF solution, it was introduced in the MBE growth chamber through an oil-free load-lock system. After degassing the substrate at 400°C for 30 minutes and successive thermal cleaning at 900ºC for 15 min, we grew a 30-nm-thick Ge buffer layer at 200ºC, which was followed by the growth of a 120-nm-thick $Ge_{0.935}Fe_{0.065}$ layer at T_S = 160-280ºC (8 samples) or a 120-nm-thick $Ge_{0.895}Fe_{0.105}$ layer at T_S = 200-280ºC (6 samples). After that, we grew a 2-nm-thick Ge capping layer at 200ºC to avoid the surface oxidation of the GeFe layer. We used *in-situ* reflection high-energy electron diffraction (RHEED) to monitor the crystallinity and surface morphology of the Ge buffer layer, GeFe layer, and Ge capping layer during the growth. Figure 8(b)-(d) shows the RHEED patterns of (b) the Ge buffer layer surface, (c) 120-nm-thick $Ge_{0.935}Fe_{0.065}$ layer surface grown at T_S = 240°C, and (d) 2-nm-thick Ge capping layer surface with the electron-beam azimuth along the <110> direction of the Ge(001) substrate. The diffraction pattern of the Ge buffer layer surface showed intense and sharp 2 × 2 streaks, which indicate a 2-dimensional growth mode and exhibit a diamond-type single crystal structure, and also the weak Kikuchi lines indicating good crystallinity. The GeFe layer surface showed intense and sharp 2 × 2 streaks but with no clear Kikuchi lines. The Kikuchi lines appeared again after the growth of the Ge capping layer.

(a)

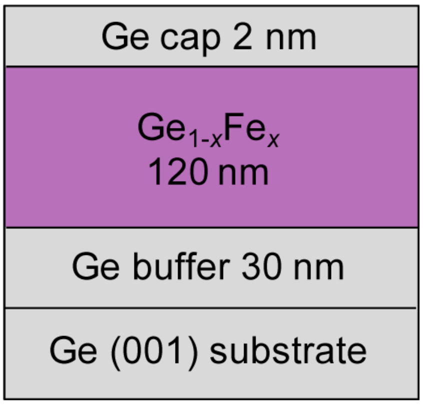

(b) Ge buffer

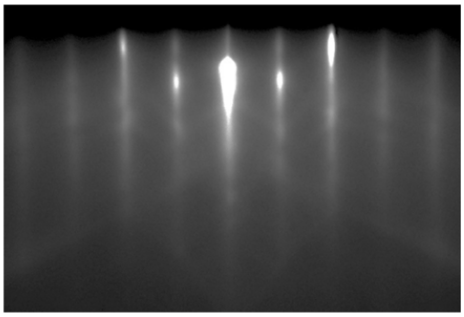

(c) $Ge_{0.935}Fe_{0.065}$, T_S = 240ºC

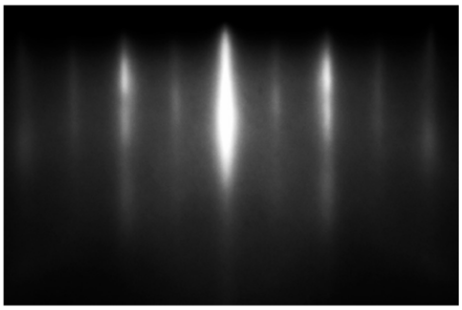

(d) Ge capping layer

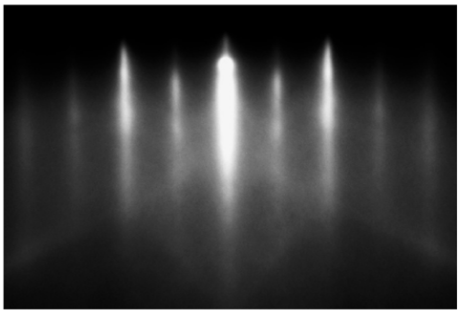

Fig. 8. (a) Schematic structure of the samples consisting of Ge cap (2 nm) / $Ge_{1-x}Fe_x$ (120 nm) / Ge buffer (30 nm) / Ge(001) substrate. (b)-(d) RHEED patterns of (b) the Ge buffer layer surface, (c) 120-nm-thick $Ge_{0.935}Fe_{0.065}$ layer surface grown at T_S = 240°C, and (d) 2-nm-thick Ge capping layer surface with the electron-beam azimuth along the <110> direction of the Ge (001) substrate. [Y. K. Wakabayashi *et al.*, Journal of Applied Physics **116**, 173906 (2014).]

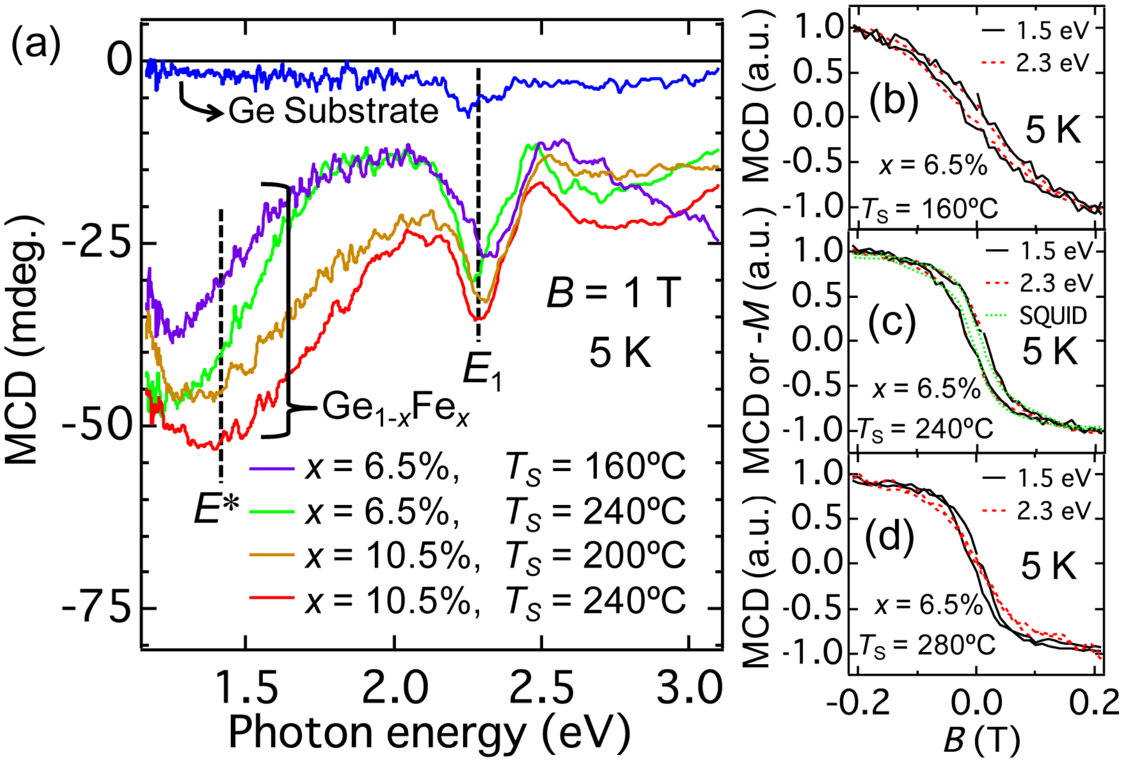

Fig. 9. (a) MCD spectra of the Ge substrate (blue curve), of the $Ge_{0.935}Fe_{0.065}$ (x = 0.065) films grown at T_S = 160ºC (violet curve) and T_S = 240ºC (green curve), and of the $Ge_{0.895}Fe_{0.105}$ (x = 0.105) films grown at T_S = 200ºC (brown curve) and T_S = 240ºC (red curve), with a magnetic field B of 1 T applied perpendicular to the film plane at 5 K. (b)-(d) MCD intensity as a function of B measured at 5 K with the photon energies of 1.5 eV (black curve) and 2.3 eV (red dotted curve) for the $Ge_{0.935}Fe_{0.065}$ films grown at (b) T_S = 160ºC, (c) T_S = 240ºC, and (d) T_S = 280ºC. In (c), the green dotted curve expresses the B dependence of $-M$ measured by SQUID. [Y. K. Wakabayashi *et al.*, Journal of Applied Physics **116**, 173906 (2014).]

We have carried out magneto-optical measurements on the GeFe films to investigate the T_S dependence of T_C. MCD, which is defined as the difference between the optical reflectances of right- and left- circular polarized lights, is a powerful tool to investigate the magnetic properties of FMSs.[30] This is because the MCD intensity is proportional to the *s*,*p*-*d* exchange interaction, which is considered to be the origin of the ferromagnetism in FMSs, and also proportional to the vertical component of the magnetization (M) in FMSs. Figure 9(a) shows the MCD spectra of the Ge substrate (blue curve), of the $Ge_{0.935}Fe_{0.065}$ films grown at T_S = 160ºC (violet curve) and 240ºC (green curve), and of the $Ge_{0.895}Fe_{0.105}$ films grown at T_S = 200ºC (brown curve) and 240ºC (red curve), with the magnetic field B of 1 T applied perpendicular to the film plane at 5 K. All the GeFe samples show the E_1 peak at around 2.3 eV corresponding to the L point of the bulk Ge as we can see in the MCD spectrum of the Ge substrate. These E_1 peaks, that are enhanced by the *s*,*p*-*d* exchange interaction in all the GeFe films, are the characteristic property of FMSs.[31] The broad peak (E^*) at around 1.4 eV observed in all the GeFe samples is thought to be related to the Fe-related impurity bands or *d*-*d* transitions.[32] Figure 9(b)–(d) shows the *B* dependence of the MCD intensities measured at 5 K with the incident photon energies of E^* (1.5 eV, black curve) and E_1 (2.3 eV, red dotted curve) for the $Ge_{0.935}Fe_{0.065}$ films grown at (b) 160ºC, (c) 240ºC, and (d) 280ºC. Figure 9(c) also shows the *B* dependence of the normalized $-M$ (green dotted curve) measured by a superconducting quantum interference device (SQUID). Here, the diamagnetic signal of the Ge substrate was subtracted from the raw *M* data. As shown in Fig. 9(b) and (c), in the $Ge_{0.935}Fe_{0.065}$ films grown at 160ºC and 240ºC, the shapes of the MCD - *B* curves at 1.5 eV and 2.3 eV are identical with each other, which means that the MCD signals at 1.5 eV and 2.3 eV originate from the same FM phase of GeFe.[33] Moreover, Fig. 9(c) shows that the shapes of the MCD - *B* curves are the same as that of the $-M$ vs. *B* curve measured by SQUID. This indicates that the *M* data measured by SQUID has the same origin as that induces the spin splitting of the energy band of GeFe. These results indicate that the origin of the ferromagnetism is the single FMS phase of GeFe. In the $Ge_{0.935}Fe_{0.065}$ film grown at 280ºC, the shapes of the MCD - *B* curves at 1.5 eV and 2.3 eV are not identical with each other [Fig. 9(d)], indicating that there are two or more magnetic phases in the film. From the same analyses on other samples, we have found that the $Ge_{1-x}Fe_x$ films grown with the range of T_S from 160ºC to 260ºC have a single FMS phase for both of $x = 0.065$ and 0.105.

Figure 10(a) shows the *B* dependence of the MCD intensity of the $Ge_{0.935}Fe_{0.065}$ film grown at T_S = 240°C measured with the incident photon energy of 2.3 eV at 5 K (blue curve), 80 K (violet curve), 100 K (orange curve), and 110 K (red curve). In the inset of the close-up view near zero magnetic field, a clear hysteresis curve is observed up to 100 K. In Fig. 10(b), we have estimated T_C using the Arrott plots (MCD^2 - *B*/MCD) of the MCD-*B* curves measured with the incident photon energy of 2.3 eV at various temperatures for the $Ge_{0.935}Fe_{0.065}$ film grown at T_S = 240°C. In the plots, we can estimate the square of the spontaneous MCD ($\propto M$) by extrapolating the data in the high magnetic-field region (0.8-1.25 T), where the MCD^2 - *B*/MCD data is sufficiently linear for accurately estimating T_C. This method is well-established and convenient because it is free from the effect of the magnetic anisotropy which affects the low-magnetic-field properties and sometimes makes the accurate estimation of T_C difficult. The estimated T_C is 100 K in this film, and we can see that the same T_C value is obtained both from the hysteresis loop analysis shown in the inset of Fig. 10(a) and from the Arrott plots in Fig. 10(b).

In Fig. 10(a), the MCD-*B* curve at 110 K, that is above T_C (= 100 K), still has a large curvature, indicating that superparamagnetism appears above T_C. Because any second-phase precipitates are not observed either in the HRTEM lattice images, as shown later in Fig. 12, or in the MCD analyses in our GeFe films, this origin is not the FM intermetallic Fe-Ge precipitates. Meanwhile, because we see non-uniform distribution of the Fe atoms in these HRTEM lattice images of our films, the large curvature of the MCD - B curve indicates that the local FM regions are formed only in the high-Fe-concentration regions by the short-range interaction even above T_C. The similar local FM regions have been observed in III-V-based FMS (Ga,Mn)As[34] and II-VI-based FMS (Zn,Cr)Te.[35]

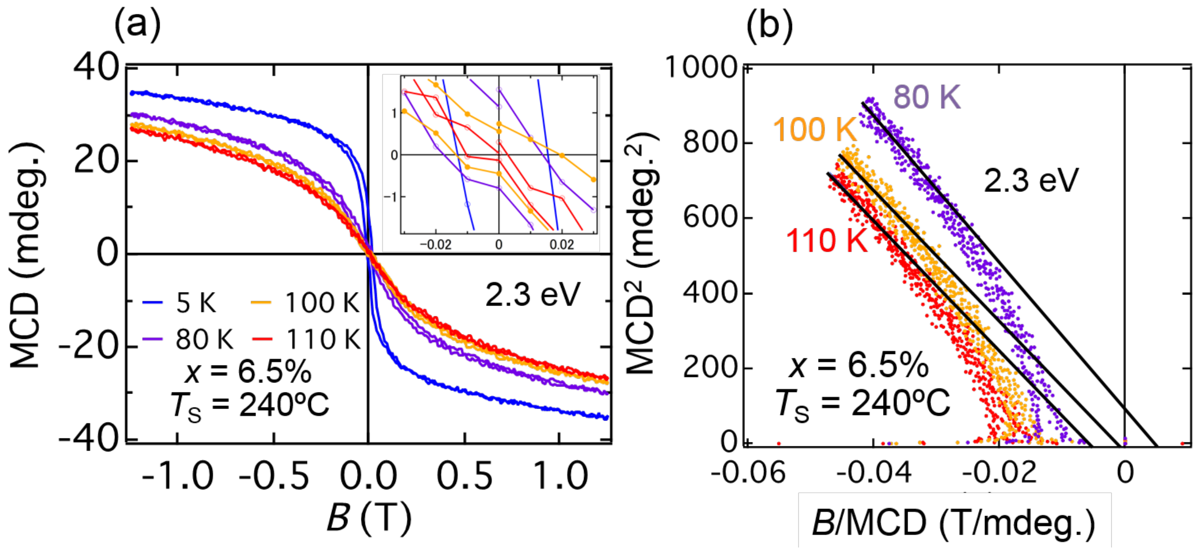

Fig. 10. (a) MCD intensity as a function of B of the $Ge_{0.935}Fe_{0.065}$ film grown at T_S = 240°C measured with the incident photon energy of 2.3 eV at 5 K (blue curve), 80 K (violet curve), 100 K (orange curve), and 110 K (red curve). The inset shows the close-up view near zero magnetic field. (b) Arrott plots of the MCD-B data measured with the incident photon energy of 2.3 eV at various temperatures for the $Ge_{0.935}Fe_{0.065}$ film grown at T_S = 240°C. [Y. K. Wakabayashi *et al.*, Journal of Applied Physics **116**, 173906 (2014).]

Figure 11(a) shows the T_S dependence of T_C of the $Ge_{0.935}Fe_{0.065}$ (x=0.065) films grown at T_S = 160-260ºC (blue circles) and the $Ge_{0.895}Fe_{0.105}$ (x=0.105) films grown at T_S = 200-260ºC (red squares). When $T_S \geq$ 280ºC (gray area), the GeFe films were phase-separated magnetically as mentioned above. Here, we estimated the T_C values using the Arrott plots of MCD at 2.3 eV. For both of x, the maximum T_C is achieved when T_S = 240ºC. The saturation magnetization M_S, that was obtained at 5 K by SQUID with a magnetic field of 1 T applied perpendicular to the film plane, in the $Ge_{0.935}Fe_{0.065}$ films grown at T_S = 160ºC (T_C = 20 K) and T_S = 240ºC (T_C = 100 K) is 0.7μ_B and 1.3μ_B per one Fe atom, respectively, where μ_B is the Bohr magneton. The M_S in the $Ge_{0.895}Fe_{0.105}$ films grown at T_S = 200ºC (T_C = 80 K) and T_S = 240ºC (T_C = 170 K) is 0.7 μ_B and 1.0 μ_B per one Fe atom, respectively. For both x, the magnetic moment increases with increasing T_C, which suggests that M_S is related to the ferromagnetic ordering.

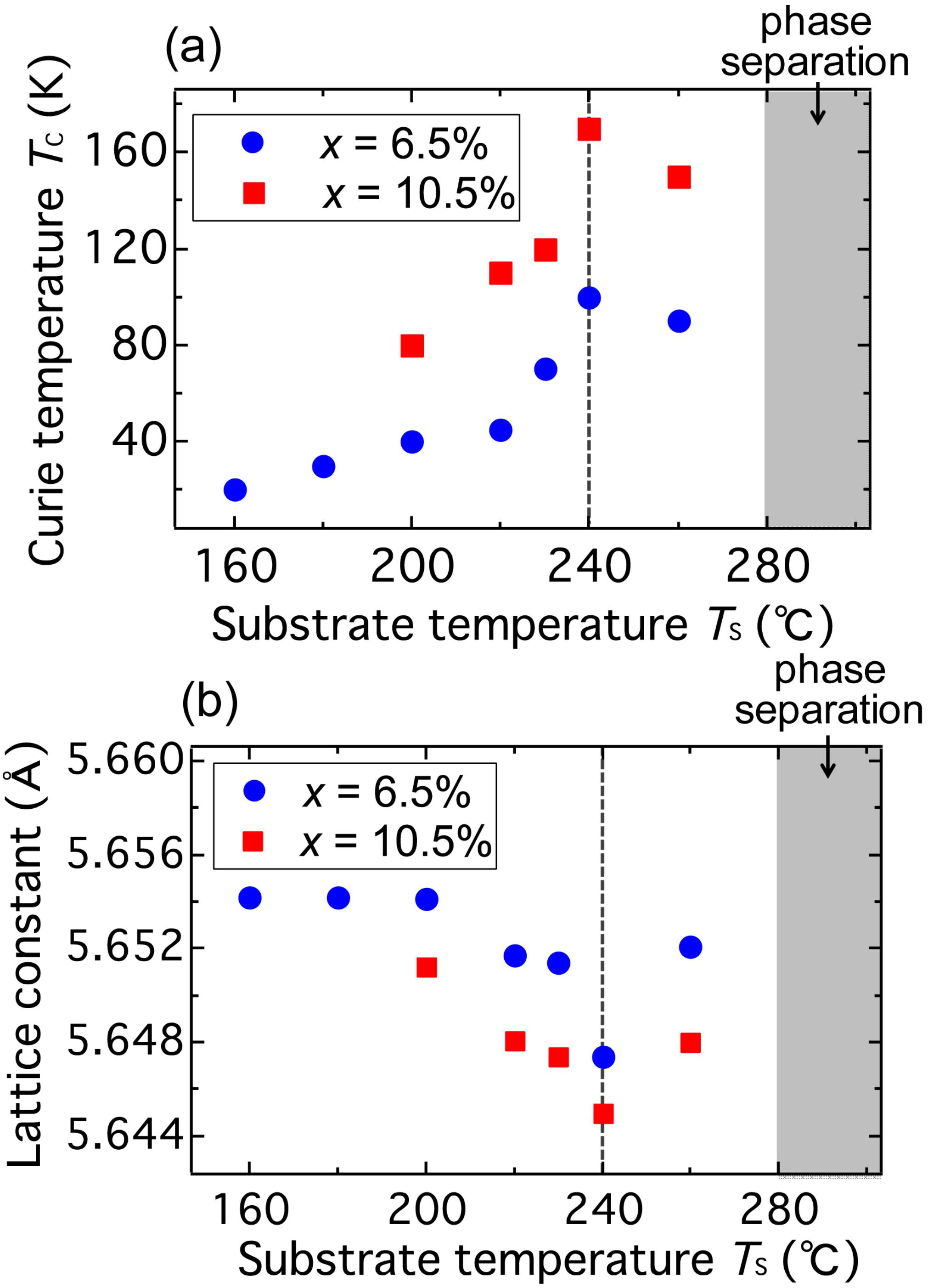

Fig. 11. (a) Curie temperature T_C as a function of T_S of the $Ge_{0.935}Fe_{0.065}$ films (blue circles) and $Ge_{0.895}Fe_{0.105}$ films (red squares), that were estimated by the Arrott plots (MCD^2 - B/MCD) with the photon energy of 2.3 eV, where B is the magnetic field. (b) Lattice constant as a function of T_S of the $Ge_{0.935}Fe_{0.065}$ (x=0.065) films grown at T_S = 160-260ºC (blue circles) and the $Ge_{0.895}Fe_{0.105}$ (x=0.105) films grown at T_S = 200-260ºC (red squares). [Y. K. Wakabayashi *et al.*, Journal of Applied Physics **116**, 173906 (2014).]

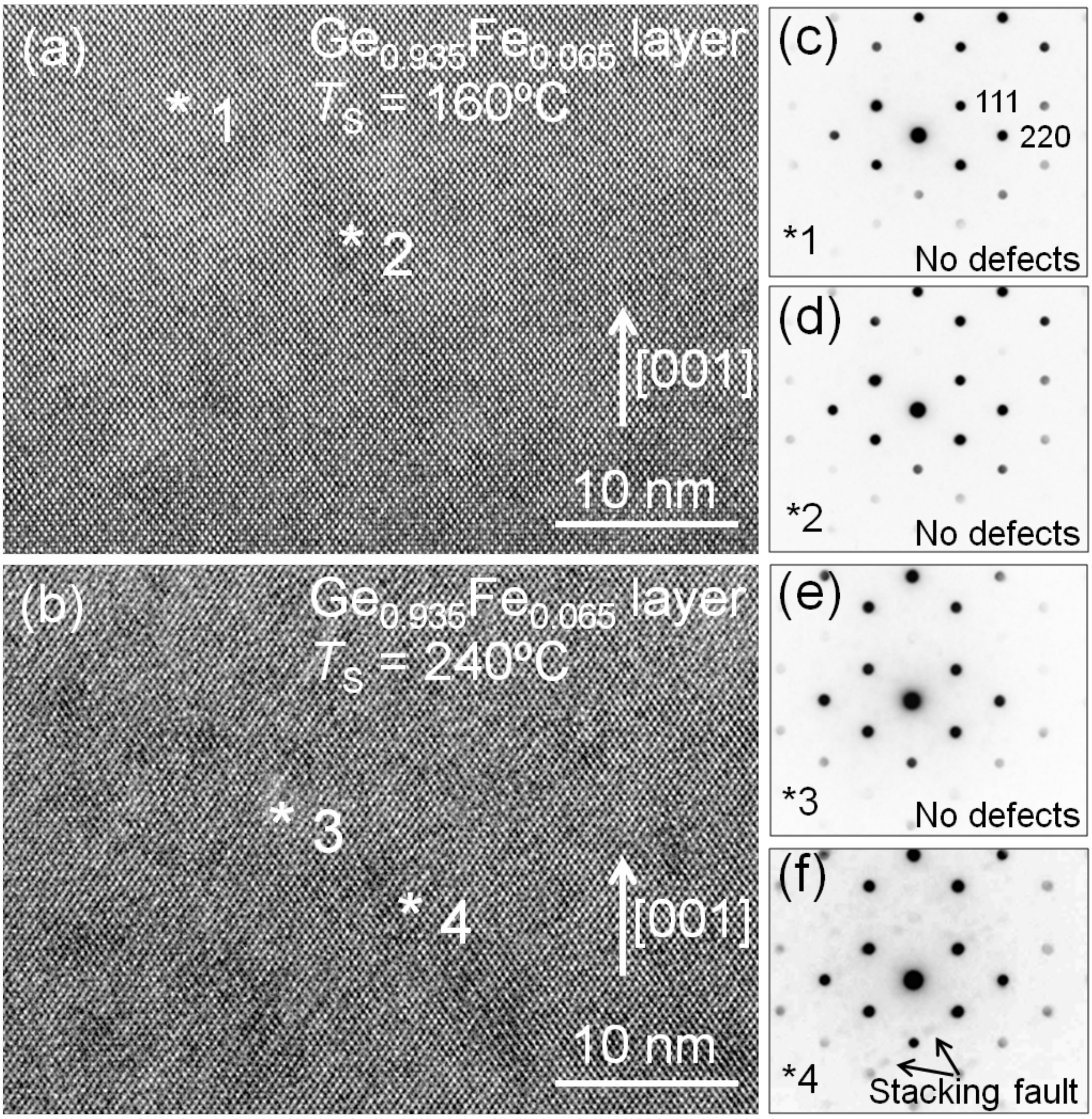

Fig. 12. (a),(b) HRTEM lattice images of the $Ge_{0.935}Fe_{0.065}$ layer grown at (a) T_S = 160ºC and (b) T_S = 240ºC projected along the Ge[110] axis. (c)-(f) TED images taken at (c) the point *1 (bright region), (d) the point *2 (dark region) in the $Ge_{0.935}Fe_{0.065}$ layer grown at T_S = 160ºC, (e) the point *3 (bright region), and (f) the point *4 (dark region) in the $Ge_{0.935}Fe_{0.065}$ layer grown at T_S = 240ºC. [Y. K. Wakabayashi *et al.*, Journal of Applied Physics **116**, 173906 (2014).]

Figure 12 shows the HRTEM lattice images of the $Ge_{0.935}Fe_{0.065}$ films grown at (a) T_S = 160ºC and (b) T_S = 240ºC projected along the Ge[110] axis. The both images indicate that the $Ge_{0.935}Fe_{0.065}$ layers have a diamond-type single-crystal structure. Although there is color (bright and dark) shading which is attributed to the non-uniform distribution of Fe atoms both in (a) and (b), there are no other ferromagnetic intermetallic Fe-Ge precipitates with a different crystal structure. By the spatially resolved EDX measurements, the local Fe concentration at *1 (bright region) and *2 (dark region) in the Ge$_{0.935}$Fe$_{0.065}$ film grown at T_S = 160ºC shown in Fig. 12(a) was estimated to be 4±1% and 7±1%, respectively. The local Fe concentration at *3 (bright region) and *4 (dark region) in the Ge$_{0.935}$Fe$_{0.065}$ film grown at T_S = 240ºC shown in Fig. 12(b) was estimated to be 3±1% and 10±1%, respectively. These results mean that the non-uniformity of Fe atoms in the Ge$_{0.935}$Fe$_{0.065}$ film grown at T_S = 240ºC is larger than that in the Ge$_{0.935}$Fe$_{0.065}$ film grown at T_S = 160ºC. Figure 12(c)-(f) shows the TED images at *1-*4. The TED images at point *1 (bright region), *2 (dark region) in the Ge$_{0.935}$Fe$_{0.065}$ film grown at T_S = 160ºC, and *3(bright region) in the Ge$_{0.935}$Fe$_{0.065}$ film grown at T_S = 240ºC showed the diffraction patterns of the diamond structure without any other crystal phases. The TED image at point *4 (dark region) in the Ge$_{0.935}$Fe$_{0.065}$ film grown at T_S = 240ºC showed the diffraction pattern of the diamond structure with weak extra spots caused by stacking-fault defects along the (111) plane, which indicates that the density of the stacking-fault defects in the Ge$_{0.935}$Fe$_{0.065}$ film grown at T_S = 240ºC is larger than that in the Ge$_{0.935}$Fe$_{0.065}$ film grown at T_S = 160ºC.

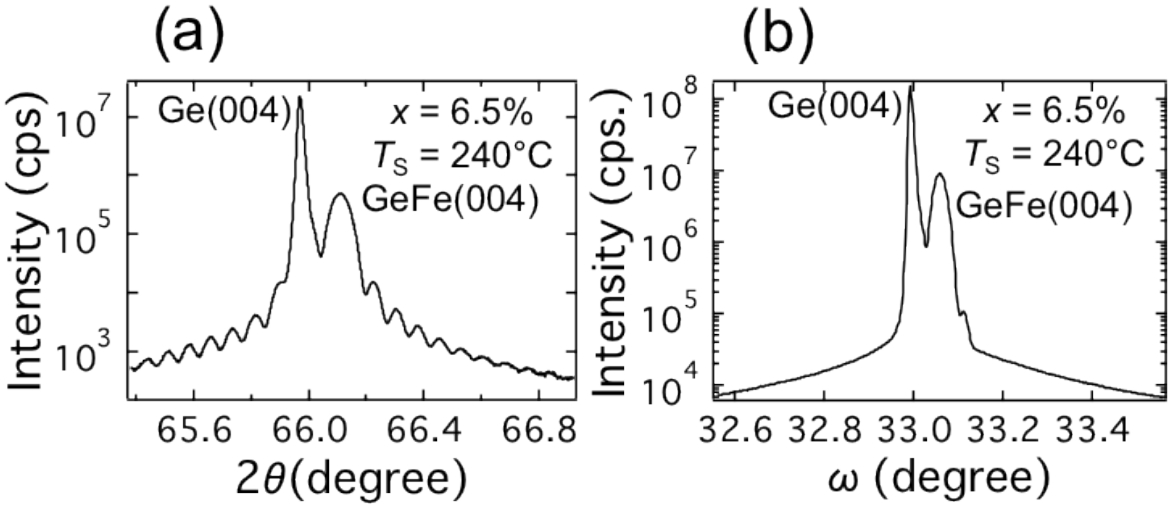

Fig. 13. (a),(b) XRD (a) θ-2θ spectrum and (b) rocking curve of the GeFe(004) reflection of the Ge$_{0.935}$Fe$_{0.065}$ film grown at T_S = 240ºC. [Y. K. Wakabayashi *et al.*, Journal of Applied Physics **116**, 173906 (2014).]

Figure 13 shows (a) the XRD θ-2θ spectrum and (b) the XRD rocking curve of the GeFe(004) reflection of the Ge$_{0.935}$Fe$_{0.065}$ film grown at T_S = 240ºC. In Fig. 13(a), the (004) diffraction peak of the GeFe film is clearly seen on the higher-angle side of the Ge(004) peak with the clear fringes, which indicates that the film is a high-quality single crystal with an abrupt and smooth interface. The excellent crystallinity of the Ge$_{0.935}$Fe$_{0.065}$ film grown at T_S = 240ºC is also confirmed by the XRD rocking curve of the GeFe(004) reflection shown in Fig. 13(b) exhibiting a narrow full width at half maximum of 0.03º, which is comparable to that of the Ge substrate, 0.01°.[36-38] Figure 11(b) shows the T_S dependence of the lattice constant that is estimated from the XRD spectra of the $Ge_{0.935}Fe_{0.065}$ (x=0.065) films grown at T_S = 160-260ºC (blue circles) and the $Ge_{0.895}Fe_{0.105}$ (x=0.105) films grown at T_S = 200-260ºC (red squares). For both of x, the lattice constant is minimum at T_S = 240ºC. Figure 14 shows the lattice constant of the $Ge_{0.935}Fe_{0.065}$ films grown at T_S = 160-260ºC (blue circles) and the $Ge_{0.895}Fe_{0.105}$ films grown at T_S = 200-260ºC (red squares), plotted as a function of T_C. We see a universal relationship between the T_C and the lattice constant, which does not depend on x. The T_C value increases as the lattice constant of the GeFe films decreases.

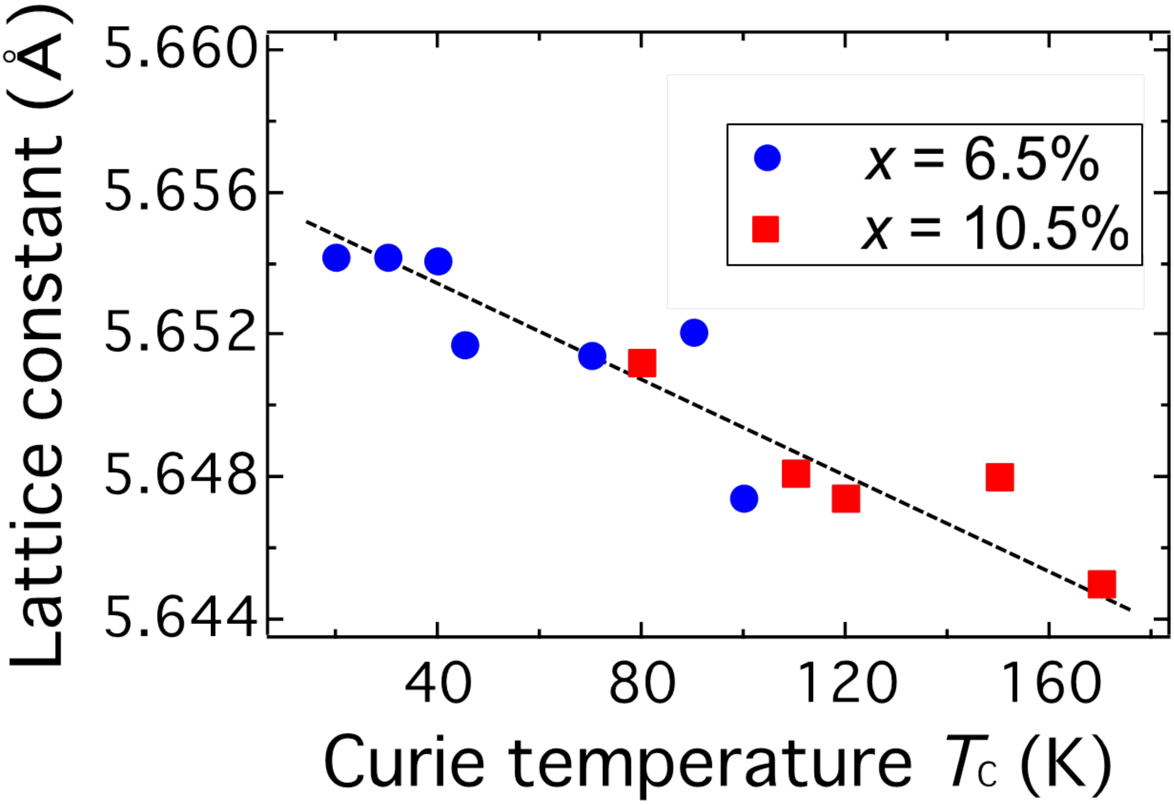

Fig. 14. Lattice constant estimated from the XRD spectra plotted as a function of T_C of the $Ge_{0.935}Fe_{0.065}$ films (blue circles) and the $Ge_{0.895}Fe_{0.105}$ films (red squares). [Y. K. Wakabayashi *et al.*, Journal of Applied Physics **116**, 173906 (2014).]

We employed c-RBS and c-PIXE to determine the position of the Fe atoms in the host Ge lattice. Figure 15 shows our experimental configurations of the PIXE-Fe- Kα and the RBS angular scans in the {100} plane (a) around the <100> axis and (b) around the <110> axis. The red dotted arrows represent the direction of the incident $^4He^{++}$ beam. We measured the scattering yields as a function of the incident angle φ, that is defined as the angle between the crystal-axial (<100> or <110>) direction and the incident direction of an energetic ion beam of ^{4}He^{++}, by varying φ in a few degrees from 0°. Ideally, the scattering yields have a minimum value at φ=0°, where the incident beam is perfectly aligned in the crystal axis and the scattering is most suppressed, while they tend to increase and finally saturate when $|\varphi|$ becomes larger than several degrees.[39 - 42] We define $\chi^{\boldsymbol{d}}(A)$ as the scattering yield originating from the element A normalized by the averaged value of the scattering yields at $|\varphi|$ ranging from 2.5 to 3° when the measurement is carried out around the $\boldsymbol{d}$ crystal-axial direction. Also, $\chi^{\boldsymbol{d}}_{\mathrm{min}}(A)$ is defined as the minimum value of $\chi^{\boldsymbol{d}}(A)$, that is obtained at φ=0°. Figure 16(a) shows the schematic illustration of the possible sites that can be occupied in the diamond-type lattice structure, including the substitutional (or host) sites S (yellow spheres), the bond-center site BC (black sphere), the antibonding sites Q (violet spheres), the hexagonal site H (blue sphere), and the tetrahedral sites T (red spheres).[43,44] Here, we refer to these sites as specific sites. Figure 16(b),(c) illustrates the locations of these specific sites when seen from the <100> and <110> directions, respectively. We note that other sites that are equivalent to these specific sites are neglected in Fig. 16 for simplicity.

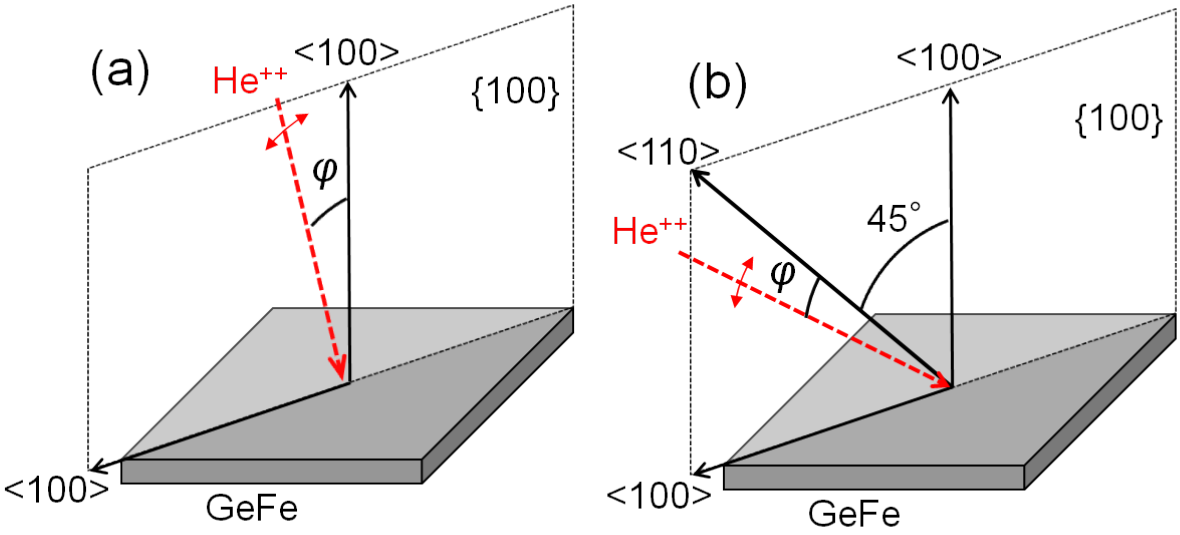

Fig. 15. (a),(b) Experimental configurations of the PIXE-Fe-Kα and RBS angular scans in the {100} plane (a) around the <100> axis and (b) around the <110> axis. The red dotted arrows represent the direction of the incident ^{4}He^{++} beam, and φ represents the angle between the incident beam direction and the axial direction. [Y. K. Wakabayashi *et al.*, Journal of Applied Physics **116**, 173906 (2014).]

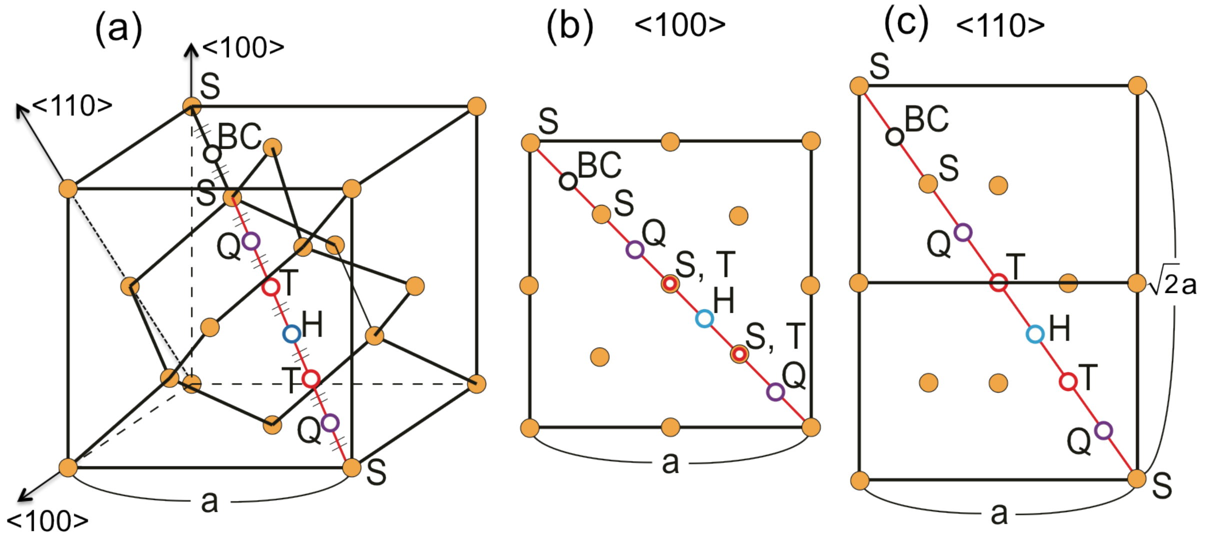

Fig. 16. (a) Schematic illustration of the possible specific sites in the diamond-type lattice structure, including the substitutional sites S (yellow spheres), the bond-center site BC (black sphere), the antibonding sites Q (violet spheres), the hexagonal site H (blue sphere), and the tetrahedral sites T (red spheres). (b),(c) The location of the specific sites when seen from the (b) <100> and (c) <110> directions. [Y. K. Wakabayashi *et al.*, Journal of Applied Physics **116**, 173906 (2014).]

Figure 17(a)-(d) shows the PIXE-Fe-Kα and RBS angular scans in the {100} plane (a),(c) around the <100> axis and (b),(d) around the <110> axis for the $Ge_{0.935}Fe_{0.065}$ films grown at (a),(b) T_S = 160ºC and (c),(d) T_S = 240ºC measured with a 2.275-MeV-$^4He^{++}$ beam. In all the graphs, the normalized yield has a minimum value at $\varphi \approx 0$º, which indicates that a lot of Fe atoms are shadowed by the host atoms and that they are not visible to the beam along the <100> or <110> axial directions. Ideally, $\chi_{\min}^{<100>}$(Ge) and $\chi_{\min}^{<110>}$(Ge) should be nearly zero.[43] In our case, however, $\chi_{\min}^{<100>}$(Ge) (=0.25 and 0.32 in the $Ge_{0.935}Fe_{0.065}$ films grown at T_S = 160ºC and 240ºC, respectively) and $\chi_{\min}^{<110>}$(Ge) (=0.12 and 0.10 in the $Ge_{0.935}Fe_{0.065}$ films grown at T_S = 160ºC and 240ºC, respectively) are larger than zero. We think that these results are attributed to the local fluctuation of the host Ge atom positions (lattice fluctuation) in our GeFe films, which is probably caused by the stacking-fault defects and the non-uniform Fe distribution. However, we obtained nearly the same values of $\chi_{\min}^{<100>}$(Ge) (=0.25 and 0.32) and $\chi_{\min}^{<110>}$(Ge) (=0.12 and 0.10) in the both samples grown at different T_S, which means that this local lattice fluctuation is not sensitive to T_S. Because we discuss the T_S dependence of the Fe location here, the lattice fluctuation is not so important for this purpose as long as the yield does not depend on T_S. Thus, we neglect the influence of this lattice fluctuation in the following discussions.

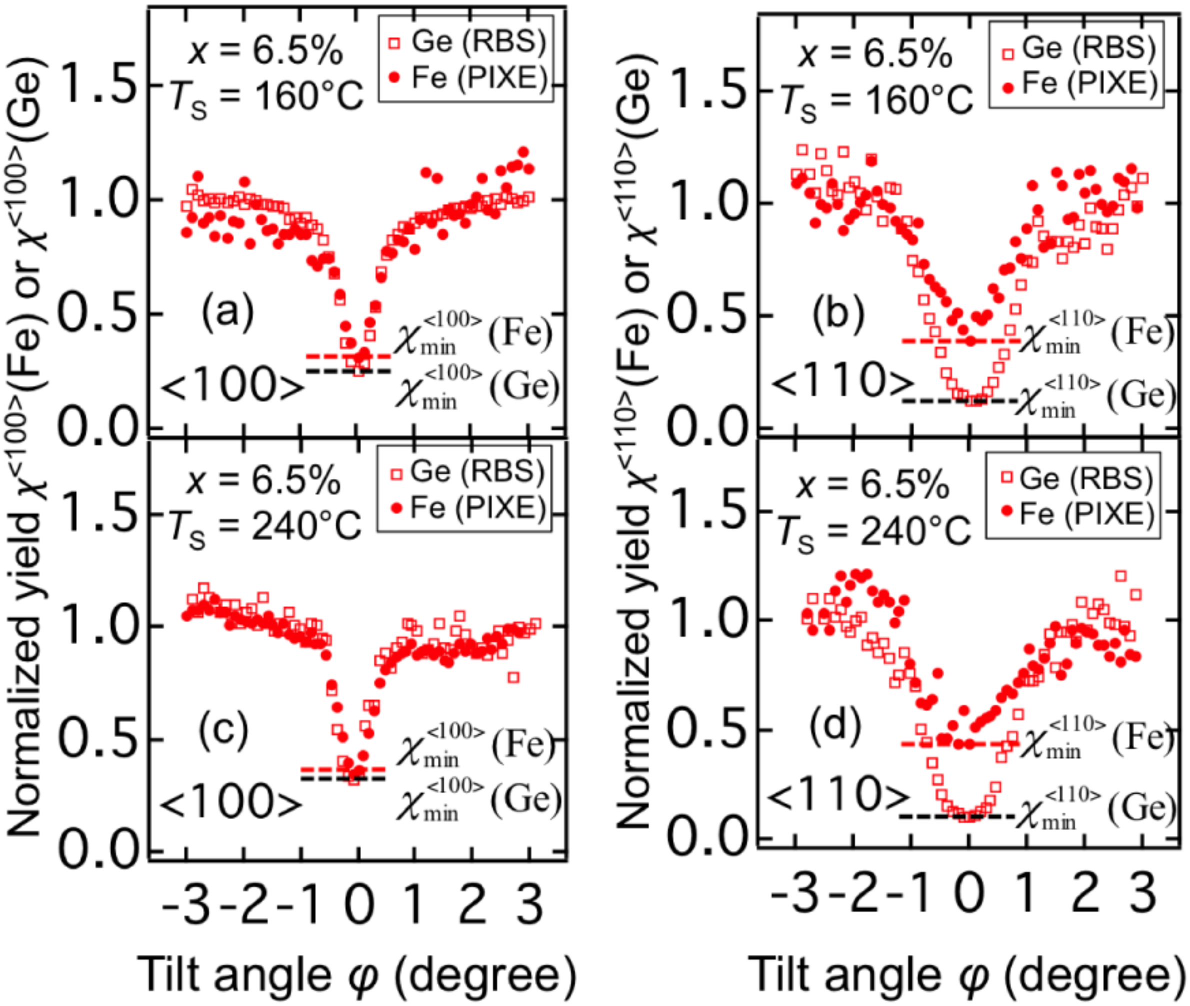

Fig. 17. (a)-(d) PIXE-Fe-Kα (solid red circles) and RBS (blank red squares) angular scans around (a),(c) the <100> axis and (b),(d) the <110> axis for the $Ge_{0.935}Fe_{0.065}$ films grown at (a),(b) T_S = 160ºC and (c),(d) T_S = 240ºC. [Y. K. Wakabayashi *et al.*, Journal of Applied Physics **116**, 173906 (2014).]

The first important point is that $\chi_{\min}^{<100>}$(Fe) is almost the same as $\chi_{\min}^{<100>}$(Ge) in both samples [Figs. 17(a) and 17(c)]. This result indicates that most Fe atoms are located on the S or T sites because the specific sites which are shadowed by the host atoms in the <100> axial direction are only the S and T sites as we can see in Fig. 16(b). We define f_{S+T} as the sum of the densities of the Fe atoms located on the S and T sites divided by the total density of the Fe atoms. We can estimate f_{S+T} by using the following equation with $\chi_{\min}^{<100>}$(Fe) and $\chi_{\min}^{<100>}$(Ge) obtained in the <100> axial direction:[39]

$$f_{S+T} = [1 - \chi_{\min}^{<100>}(\mathrm{Fe})]/[1 - \chi_{\min}^{<100>}(\mathrm{Ge})]. \tag{15}$$

By using eq. (15), f_{S+T} in the $Ge_{0.935}Fe_{0.065}$ films grown at T_S = 160ºC and T_S = 240ºC is estimated to be 93% and 96%, respectively. These results mean that, in the $Ge_{0.935}Fe_{0.065}$ films grown at T_S = 160ºC and T_S = 240ºC, the small fraction of 7% and 4% of the doped Fe atoms is located on the sites other than the S or T sites.

The second important point is that $\chi_{\min}^{<110>}$(Fe) is higher than $\chi_{\min}^{<110>}$(Ge) in the both $Ge_{0.935}Fe_{0.065}$ films grown at T_S = 160ºC [Fig. 17(b)] and T_S = 240ºC [Fig. 17(d)]. As can be seen in Figs. 16(b) and 16(c), the Fe atoms on the T sites in the diamond lattice are shadowed by the host atoms in the <100> direction but are exposed in the <110> direction. The atoms on the T sites are irradiated by the beam in all the φ range shown in Fig. 17(b) and 17(d). It is known that the yields coming from the exposed atoms on the T sites are slightly enhanced in the vicinity of the <110> direction ($\varphi \approx 0^\circ$) due to the flux peaking effect,[45] which has been well understood both theoretically[46] and experimentally.[47] The flux peaking effect is induced by the increase in the flux of the incident energetic ion beam near the T sites in the <110> direction.[48-50] From the numerical calculation, the enhancement factor F for a surface layer, which is defined as the ratio of the intensity of the Fe-Kα-X-rays coming from the atoms on the T sites at φ=0º to that at $|\varphi|$=2º, has been estimated to be in the range of 1.8 - 2.2 in the <110> axis for a diamond cubic lattice.[39,43] The ratio f_T of the density of the Fe atoms on the T sites to the sum of those on the S and T sites can be obtained from the <110> channeling results by the following equation:[49]

$$\chi_{\min}^{<110>}(\mathrm{Fe}) = (1 - f_{S+T}) + f_{S+T}[F f_T + \chi_{\min}^{<110>}(\mathrm{Ge})(1 - f_T)]. \tag{16}$$

By eq. (16), f_T in the $Ge_{0.935}Fe_{0.065}$ films grown at T_S = 160ºC and T_S = 240ºC is estimated to be 13-16% and 15-18%, respectively. In the case of typical III-V-based FMS (Ga,Mn)As, the similar fractions of the Mn atoms on the T sites have been found,[50,51] and it has been known that the density of the substitutional Mn atoms is correlated with T_C, which means that they determine the FM properties of (Ga,Mn)As films.[34,52] In the case of GeFe, however, we do not see a clear difference in the Fe density on the T sites between the two samples, which have the large difference in the T_C values (20 K and 100 K for the films grown at T_S = 160ºC and T_S = 240ºC, respectively). This indicates that the ferromagnetism in GeFe is not directly related to the density of the substitutional Fe atoms.

As described above, the f_T values obtained in the $Ge_{0.935}Fe_{0.065}$ films grown at T_S = 160ºC (T_C = 20 K, M_S = 0.7 μ_B per one Fe atom) and T_S = 240ºC (T_C = 100 K, M_S = 1.0 μ_B per one Fe atom) are almost the same (13-16% and 15-18%, respectively), but the lattice constants (5.654 and 5.647 Å), Fe concentration fluctuations (4-7% and 3-10%), and the stacking-fault densities are different between them. Our results indicate that these characteristics, except for f_T, are correlated with the ferromagnetism. Similar crystallographic changes have been reported in face-centered cubic crystals (CuMnSi and CrMnNi alloys), in which the (004) diffraction peak shifts to the higher angle side with an increase in the density of the stacking-fault defects along the (111) plane.[53-55] Our results mean that the non-uniform distribution of the Fe atoms is a key factor in determining the detailed crystallographic features and magnetic properties.[56] The same tendency has been observed in the annealing-temperature dependence of the GeFe films (see section 3.2).[32] When the non-uniformity of the Fe concentration is enhanced, the locally high-Fe-concentration regions can easily connect each other magnetically, resulting in higher T_C. In III-V and II-VI-based FMSs, such an increase in T_C due to the enhancement of the non-uniformity of the magnetic impurities is predicted theoretically[57] by the random phase approximation in the Heisenberg model.[58,59] Thus, room-temperature ferromagnetism will be achieved by doping a higher concentration of Fe atoms and enhancing the non-uniformity of Fe atoms adequately. The important point is that the GeFe films have a single FMS phase which is confirmed by the MCD and SQUID measurements [see Fig. 9(c)], even though they have the non-uniformity of the Fe concentration. This means that, once ferromagnetism appears, the locally high-Fe-concentration regions and low-Fe-concentration regions are magnetically coupled by the *s*,*p*-*d* exchange interaction, which is confirmed by the enhancement of the E_1 peak in the MCD spectra [see Fig. 9(a)].

In summary of this section, we have studied the T_S dependence of T_C, the lattice constant, the non-uniformity of Fe atoms, and the stacking-fault defects of the $Ge_{1-x}Fe_x$ films with x = 0.065 and 0.105, and observed continuous changes in T_C and in the lattice constant as a function of T_S. The T_C value increases with the decrease in the lattice constant, and the relationship between T_C and the lattice constant does not depend on x. The T_C reaches maximum values of 100 K and 170 K when T_S = 240ºC for x = 0.065 and 0.105, respectively. By using the spatially resolved TED combined with the EDX, we have found that the density of the stacking-fault defects and the non-uniformity of Fe atoms in the $Ge_{0.935}Fe_{0.065}$ film grown at T_S = 240ºC are larger than those in the $Ge_{0.935}Fe_{0.065}$ film grown at T_S = 160ºC. By using c-RBS and c-PIXE characterizations, we have found that the small fraction of 7% and 4% of the doped Fe atoms are located on the sites other than the S or T sites in the $Ge_{0.935}Fe_{0.065}$ samples with T_C of 20 and 100 K, respectively. Among the Fe atoms located on the S and T sites, 13-16% and 15-18% of them exist on the T sites in the $Ge_{0.935}Fe_{0.065}$ films with the different T_C values of 20 and 100 K, respectively. By considering these results, we conclude that the non-uniformity of the Fe concentration and the stacking-fault defects formed in the high Fe concentration region play an important role in determining the FM properties of the GeFe films. The influences of the tetrahedral interstitial magnetic impurities on the ferromagnetic properties are completely different between GeFe and (Ga,Mn)As.

3. 2. Annealing effect

The current problem of GeFe is its low T_C, which is at the highest 170 K as shown in Fig. 11. Recently, GeFe quantum dots with a high T_C of ~400 K without any observable precipitates have been reported.[60] Thus, if we can grow GeFe quantum dots (or nano-particles) inside a Ge film with a flat surface or interfaces with other layers (or substrates), they are very promising. In fact, the ferromagnetic MnAs nano-particles embedded in GaAs have shown intriguing properties induced by Coulomb blockade and spin-dependent tunneling.[61,62] In III-V-based FMS (Ga,Mn)As, post-growth annealing is known to be a powerful technique to improve the T_C by removing the interstitial Mn atoms from the (Ga,Mn)As layer.[63,64] In this section, we investigate the annealing effect on GeFe in order to enhance the ferromagnetism of GeFe and its relevance to the structural and magnetic properties. Through this study, we find that the ferromagnetism of GeFe becomes strong with the enhancement of the non-uniformity of the Fe atoms by the annealing.

The $Ge_{0.895}Fe_{0.105}$ thin film studied here was epitaxially grown on a Ge(001) substrate by LT-MBE. The growth process is described as follows. After the Ge(001) substrate was chemically cleaned and its surface was hydrogen-terminated by buffered HF solution, it was introduced in the MBE growth chamber through an oil-free load-lock system. After degassing the substrate at 400°C for 30 min and successive thermal cleaning at 900°C for 15 min, a 30-nm-thick Ge buffer layer was grown at 200°C, followed by the growth of a 60-nm-thick $Ge_{0.895}Fe_{0.105}$ layer at 240°C. The *in-situ* RHEED was used to observe the crystallinity and morphology of the surface during the growth. The diffraction pattern of the Ge buffer layer surface showed intense and sharp 2 × 2 streaks, and the $Ge_{0.895}Fe_{0.105}$ surface also showed a 2 × 2 pattern with no extra spots, indicating two-dimensional epitaxial growth. Post-growth annealing was carried out in a nitrogen atmosphere for 30 min at 400, 500, and 600°C.

The crystallographic analyses of the $Ge_{0.895}Fe_{0.105}$ films were performed by HRTEM. Figure 18(a),(b) shows the HRTEM lattice images of the $Ge_{0.895}Fe_{0.105}$ film as grown and annealed at 500°C projected along the Ge [110] axis, respectively. The both images indicate that the $Ge_{0.895}Fe_{0.105}$ layers have a diamond-type single-crystal structure with an atomically flat surface. Although the color (dark and bright) contrast in the GeFe layer is attributed to the non-uniform distribution of Fe atoms and stacking-fault defects as discussed in section 3.1, there are no other ferromagnetic intermetallic Fe-Ge precipitates with a different crystal structure.

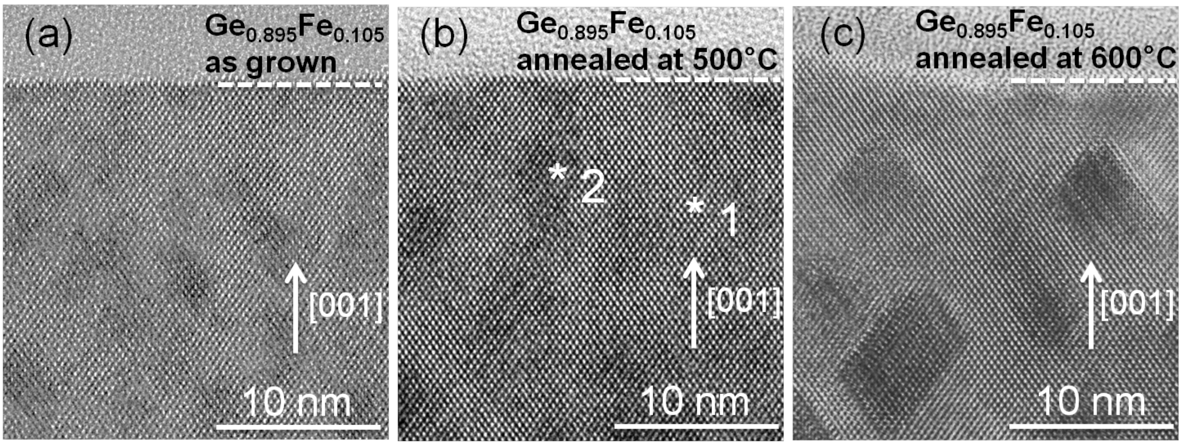

Fig. 18. (a)-(c) HRTEM lattice images projected along the Ge[110] axis of $Ge_{0.895}Fe_{0.105}$ (a) as grown and after annealing at (b) 500°C and (c) 600°C. [Y. K. Wakabayashi *et al.*, Physical Review B **90**, 205209 (2014).]

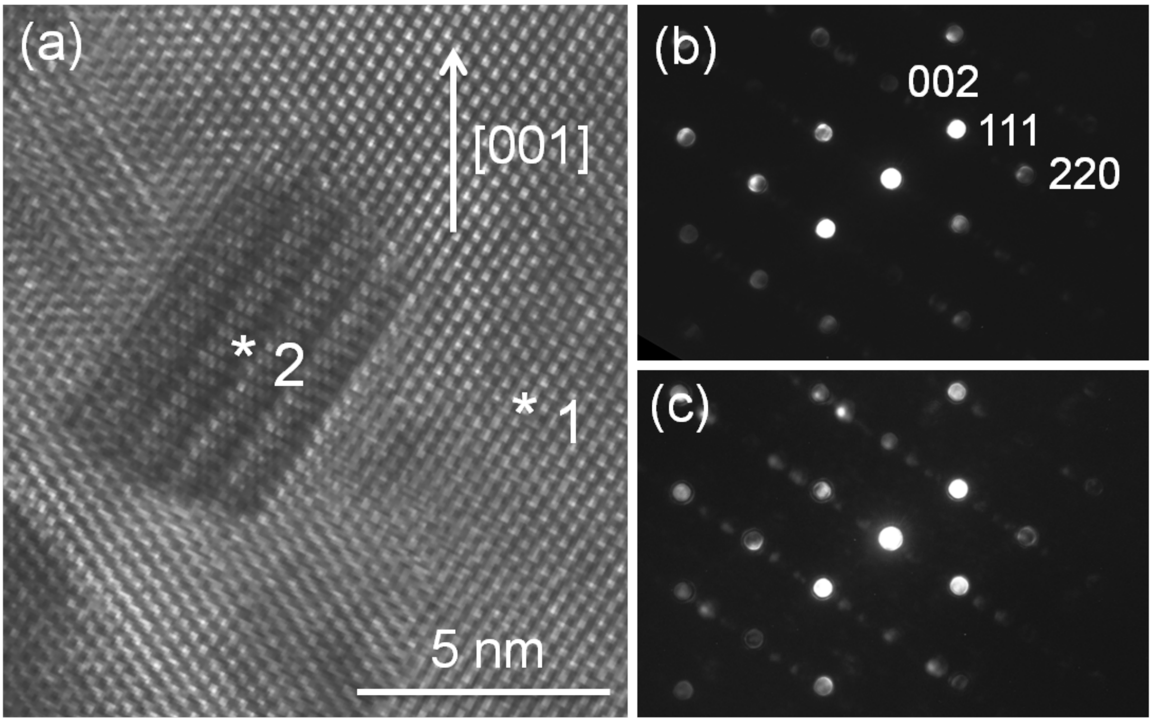

Fig. 19. (a) HRTEM lattice image projected along the Ge[110] axis of a ferromagnetic nano-particle formed in the $Ge_{0.895}Fe_{0.105}$ film after annealing at 600°C. (b),(c) TED images obtained from (b) the diamond-crystal-structure region (*1) and from (c) the nano-particle (*2). [Y. K. Wakabayashi *et al.*, Physical Review B **90**, 205209 (2014).]

Figure 18 (c) shows a HRTEM lattice image of the $Ge_{0.895}Fe_{0.105}$ film annealed at 600°C projected along the Ge [110] axis, where we see many nano-particles formed in the film. Figure 19 (a) shows the magnified view of the HRTEM lattice image of one of the nano-particles in the $Ge_{0.895}Fe_{0.105}$ film annealed at 600°C, indicating that the nano-particles have periodic twins and stacking faults. By the spatially resolved TED combined with the spatially resolved EDX, the local electron-diffraction pattern and Fe concentration were obtained. In the EDX measurements, the error bar of the Fe concentration is ±1%, which mainly originates from the sample drift of ~1 nm during the measurements. The local Fe concentration at *1 (bright region) and *2 (dark region) of the GeFe film annealed at 500°C shown in Fig. 18 (b) was estimated to be 8 and 23%, respectively. When the annealing temperature is 600°C, the local Fe concentration at *1 (homogeneous diamond-crystal-structure region) and *2 (inside the nano-particle) in Fig. 19 (a) was estimated to be 5 and 25%, respectively. These results indicate that the higher the annealing temperature is, the larger the non-uniformity of the Fe concentration becomes. Figure 19 (b) shows the TED image at *1, exhibiting the diffraction pattern of the diamond-type lattice structure with extremely weak extra spots due to stacking-fault defects. Figure 19 (c) shows the TED image at *2, indicating a similar diffraction pattern of the diamond-type lattice structure including clear twins and stacking faults.[65] In either TED images, we do not see any diffractions from precipitates with crystalline Fe-Ge intermetallic compounds of other crystal structures.

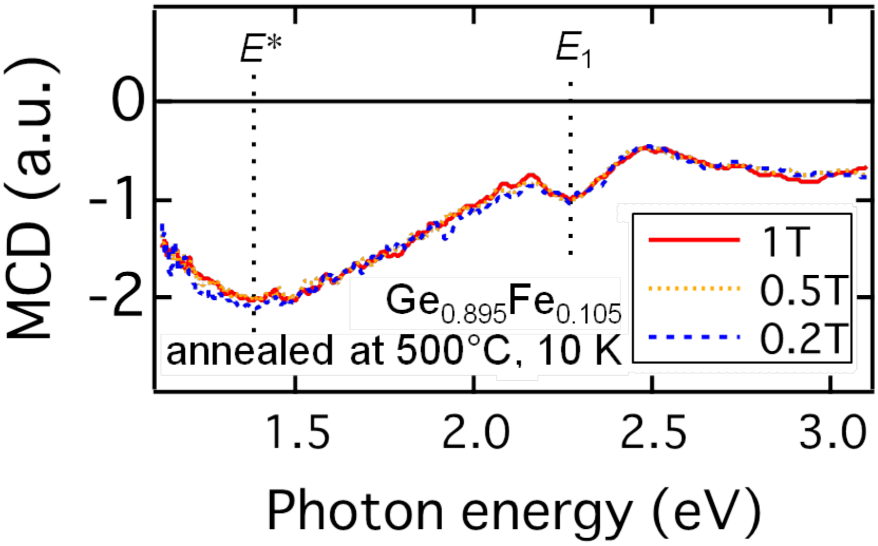

Fig. 20. Normalized MCD spectra of the $Ge_{0.895}Fe_{0.105}$ film annealed at 500°C with magnetic fields of 1 T (red solid curve), 0.5 T (orange dotted curve), and 0.2 T (blue broken curve) applied perpendicular to the film plane at 10 K. [Y. K. Wakabayashi *et al.*, Physical Review B **90**, 205209 (2014).]

Figure 20 shows the normalized MCD spectra of the $Ge_{0.895}Fe_{0.105}$ film annealed at 500°C at different magnetic fields (0.2, 0.5, and 1 T) applied perpendicular to the film at 10 K. They are superimposed on a single spectrum over the whole photon energy range, indicating that the MCD spectrum originates from the nearly single ferromagnetic phase of

GeFe[18] even though it has the non-uniform distribution of Fe atoms. As described later, although the non-uniformity induces weak spin-glass-like behavior in a very low temperature region, it is not strong enough to induce magnetic phase separation. This suggests that the locally high-Fe-concentration region and low-Fe-concentration region are magnetically coupled by the *s*,*p*-*d* exchange interaction, which results in the nearly homogeneous ferromagnetic behavior.

Figure 21 (a) shows the MCD spectra of the Ge substrate, the as-grown $Ge_{0.895}Fe_{0.105}$ film, and the $Ge_{0.895}Fe_{0.105}$ film annealed at 400, 500, and 600°C (from the top to the bottom) with a magnetic field of 1 T applied perpendicular to the film plane at 10 K. All the samples show the E_1 peak at around 2.3 eV corresponding to the L point of bulk Ge as we can see in the MCD spectrum of the Ge substrate and a broad peak (E*) at around 1.4 eV. The E_1 peak enhanced by the *s*,*p*-*d* exchange interaction is a characteristic property of FMSs.[31] As described in section 3.1, for the origin of the E* peak, there are two possibilities; optical transitions from the impurity bands, which have been observed in III-V-based FMS $Ga_{1-x}Mn_xAs$,[66] and *d*-*d* transitions related to the crystal-field splitting of substitutional Fe atoms. The E_1 peak is suppressed by the annealing at 600°C, which is thought to be related to the phase separation shown in Fig. 18 (c). Generally, an MCD spectrum of a phase-separated material is expressed by the sum of these phases. During the annealing at 600°C, the Fe atoms are removed from the region *1 in Fig. 19(a) and it becomes nearly pure Ge, which results in the decreased intensity of the E_1 peak. Figure 21 (b)-(d) shows the magnetic-field (B) dependence of the normalized MCD intensities at the E* (1.5 eV, solid curve) and E_1 (2.3 eV, dotted curve) for (b) the as-grown $Ge_{0.895}Fe_{0.105}$ film and for the $Ge_{0.895}Fe_{0.105}$ films annealed at (c) 500°C and (d) 600°C. Figure 21 (c) also shows the B dependence of the normalized M for the $Ge_{0.895}Fe_{0.105}$ film annealed at 500°C (green curve) measured by SQUID. Here the diamagnetic signal of the Ge substrate was subtracted from the raw M data. In the as-grown GeFe film and the annealed film at 500°C, the shapes of the curves at 1.5 and 2.3 eV are identical with each other, which means that the E* and E_1 peaks originate from the nearly single ferromagnetic phase of GeFe as previously mentioned. Moreover, Fig. 21 (c) shows that the hysteresis loops of MCD have the same shape as that of the M - B curve measured by SQUID at 10 K in the $Ge_{0.895}Fe_{0.105}$ film annealed at 500°C. This indicates that the M data measured by SQUID has the same origin as that induces the spin splitting of the energy band of GeFe. Therefore, we conclude that the origin of the magnetization is only the nearly single ferromagnetic phase of GeFe. In contrast, after the annealing at 600°C, the curves are not identical, which indicates that there are two or more magnetic phases in the film. These results mean that the GeFe layer was phase-separated magnetically and crystallographically by the annealing at 600°C.

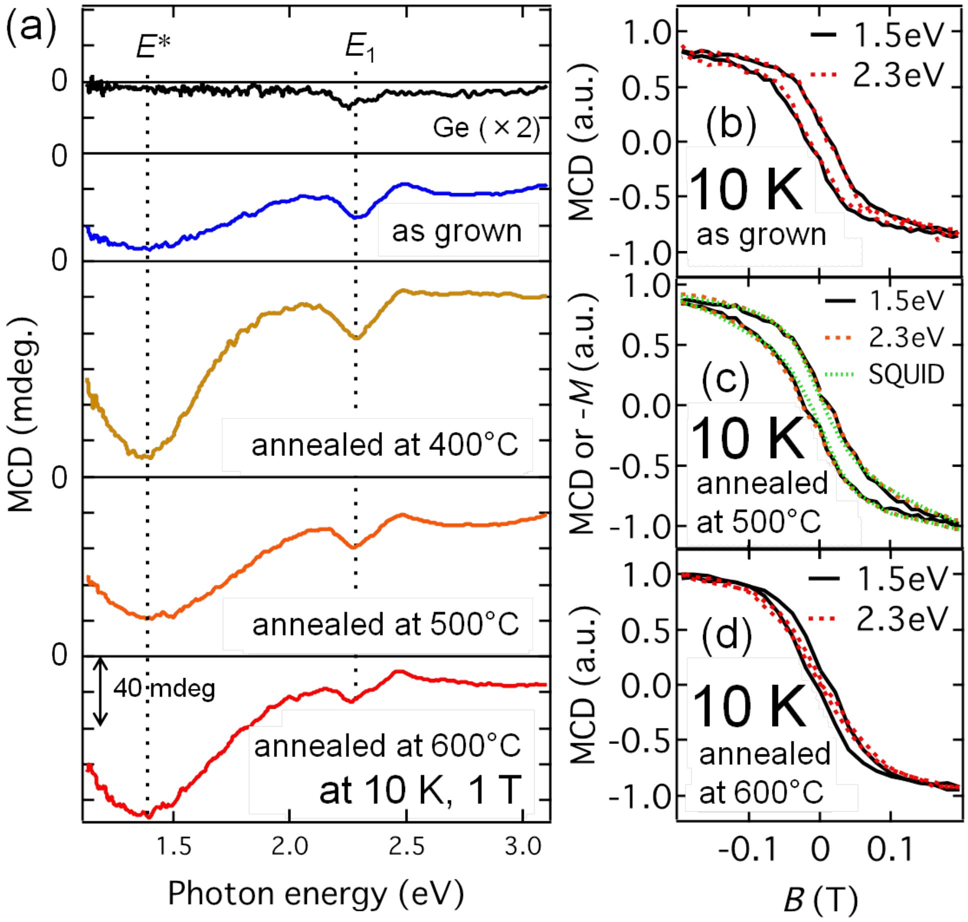

Fig. 21. (a) MCD spectra of the Ge substrate, the as-grown $Ge_{0.895}Fe_{0.105}$ film, and the $Ge_{0.895}Fe_{0.105}$ film annealed at 400, 500, and 600°C (from the top to the bottom) with a magnetic field of 1 T applied perpendicular to the film plane at 10 K. (b)-(d) Magnetic-field dependence of the MCD at 1.5 eV (E^* peak) and 2.3 eV (E_1 peak) for the GeFe films (b) as grown and annealed at (c) 500°C and (d) 600°C. In (c), the green curve expresses the magnetic-field dependence of the normalized -M measured by SQUID for the $Ge_{0.895}Fe_{0.105}$ film annealed at 500°C. [Y. K. Wakabayashi *et al.*, Physical Review B **90**, 205209 (2014).]

Figure 22 (a) shows the magnetic-field dependence of MCD at E_1 (2.3 eV) of the $Ge_{0.895}Fe_{0.105}$ film annealed at 500ºC measured at 10 K (blue curve), 150 K (green curve), 210 K (pink curve), and 240 K (red curve). The inset shows the close-up view near the zero magnetic field. A clear hysteresis curve is observed up to 210 K. We estimated the T_C values of our films by using the Arrott plots (MCD^2 - B/MCD), which were obtained from the MCD-B data. In the plots, we can estimate the square of the spontaneous MCD by extrapolating the data in the high magnetic-field region. This method is well-established and convenient because it is free from the effect of the magnetic anisotropy which affects the low magnetic field properties and sometimes makes the accurate estimation of T_C difficult. Figure 22 (b) shows the Arrott plots of the MCD - B data at 2.3 eV for the $Ge_{0.895}Fe_{0.105}$ film annealed at 500°C, indicating that the T_C is 210 K. The same T_C value is obtained both in the hysteresis loop analysis in Fig. 22 (a) and the Arrott plots in Fig. 22 (b).

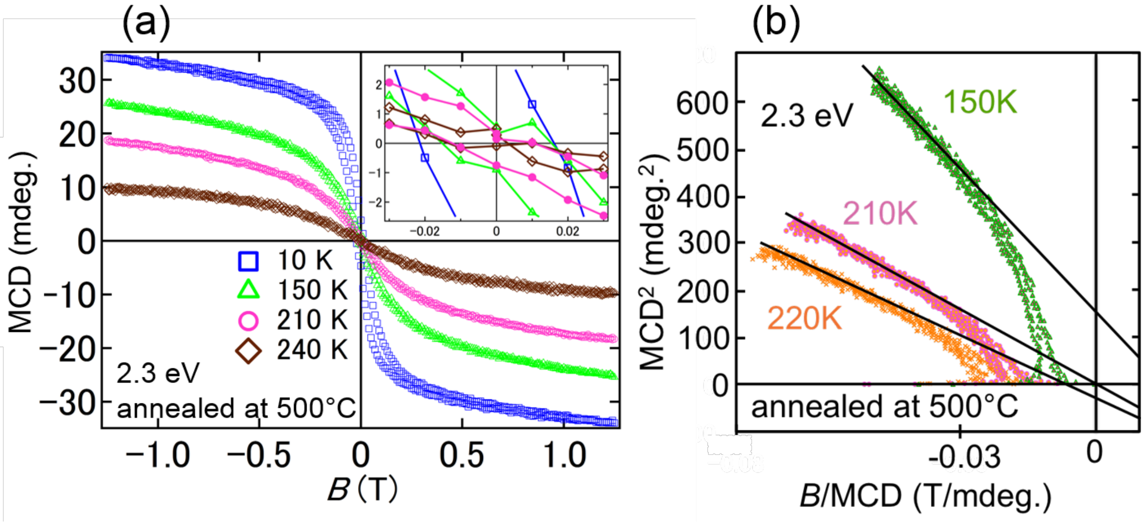

Fig. 22. (a) Magnetic-field dependence of the MCD intensity at E_1 (2.3eV) of the $Ge_{0.895}Fe_{0.105}$ film annealed at 500°C measured at 10 K (blue curve), 150 K (green curve), 210 K (pink curve), and 240 K (brown curve). The inset shows the close-up view near zero magnetic field. (b) Arrott plots of the MCD-*B* data at 2.3 eV measured at various temperatures for the $Ge_{0.895}Fe_{0.105}$ film annealed at 500°C. [Y. K. Wakabayashi *et al*., Physical Review B **90**, 205209 (2014).]

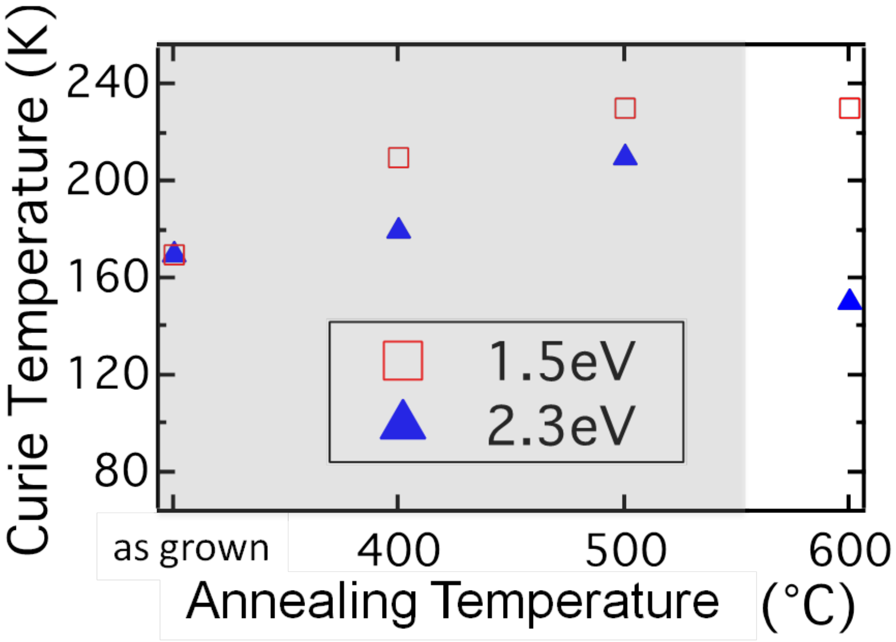

Fig. 23. (a) Curie temperature as a function of the annealing temperature of the $Ge_{0.895}Fe_{0.105}$ films estimated by the Arrott plot (MCD^2 – *B*/MCD) at the photon energies of 1.5 eV (square) and 2.3 eV (triangle). [Y. K. Wakabayashi *et al*., Physical Review B **90**, 205209 (2014).]

Figure 23 shows the T_C of the $Ge_{0.895}Fe_{0.105}$ films estimated at the photon energy of 1.5 eV (square) and 2.3 eV (triangle). In the as-grown film, the T_C values at both of the photon energies are the same. When it is annealed at 400 or 500°C, even though the film is magnetically homogeneous as discussed above, we see a slight difference in the T_C values between at 1.5 and 2.3 eV most likely due to the non-uniformity of the Fe concentration, which is enhanced by the annealing. When the annealing temperature is 600°C, the T_C values at 1.5 and 2.3 eV are completely different due to the phase separation.

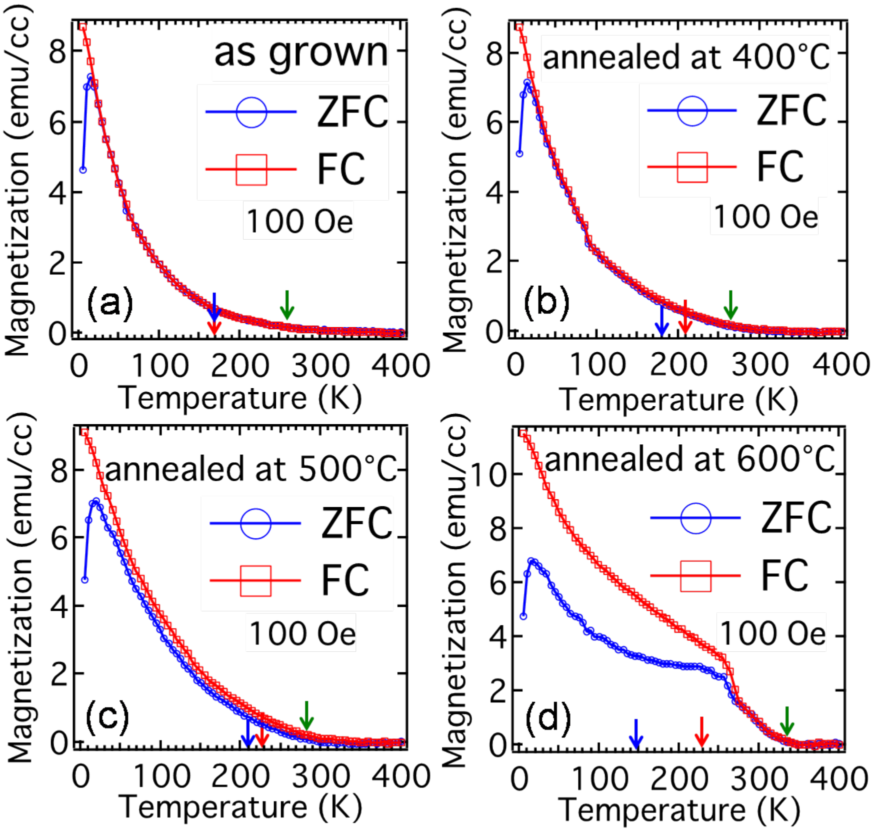

Fig. 24. (a)-(d) Magnetization versus temperature (M-T) curves of the $Ge_{0.895}Fe_{0.105}$ samples (a) as grown and annealed at (b) 400, (c) 500, and (d) 600°C. The measurements were performed in the two processes of field cooling (FC, red curve) and zero field cooling (ZFC, blue curve) with a magnetic field of 100 Oe applied perpendicular to the film plane. The red and blue arrows are the T_C values estimated by the Arrott plots of the MCD-B data obtained at 1.5 and 2.3 eV, respectively. The green arrows express θ_a estimated by the Curie-Weiss plots. [Y. K. Wakabayashi *et al.*, Physical Review B **90**, 205209 (2014).]

The magnetization versus temperature (M - T) curves of the films were measured by SQUID. Figure 24 (a)-(d) shows the M-T curves of the $Ge_{0.895}Fe_{0.105}$ samples as grown and annealed at 400, 500, and 600°C, respectively. In the zero-field-cooling (ZFC) process shown by the blue curves, M was measured with a magnetic field of 100 Oe applied perpendicular to the film plane with increasing temperature after the sample was cooled down to 5 K from room temperature without a magnetic field. In the field-cooling (FC) process shown by the red curves, M was measured with decreasing temperature from room temperature to 5 K under a magnetic field of 100 Oe applied perpendicular to the film plane. The red and blue arrows are the T_C values estimated by the Arrott plots obtained at 1.5 eV and 2.3 eV, respectively. The small leap of M at around 80 K in Fig. 24 (b) is the artifact caused by the switching of the measurement range of SQUID. Figure 25(a)-(d) shows the Curie-Weiss plots ($1/M$-T curves) obtained in the FC process for the $Ge_{0.895}Fe_{0.105}$ films (a) as grown and annealed at (b) 400, (c) 500, and (d) 600°C. The high-temperature part is described by the Curie-Weiss law. The green arrows in Fig. 24 are the asymptotic Curie temperature θ_a deduced from these Curie-Weiss plots. The θ_a values are higher than the T_C values, which indicates the existence of the ferromagnetic domains above T_C in the GeFe films as mentioned below. The θ_a value is increased from 260 K (as grown) to 285 K (annealed at 500°C) by the annealing while the film keeps the single magnetic phase. This result means that the enhancement of the non-uniformity of the Fe concentration increases the ferromagnetic interaction in the locally high-Fe-concentration region.

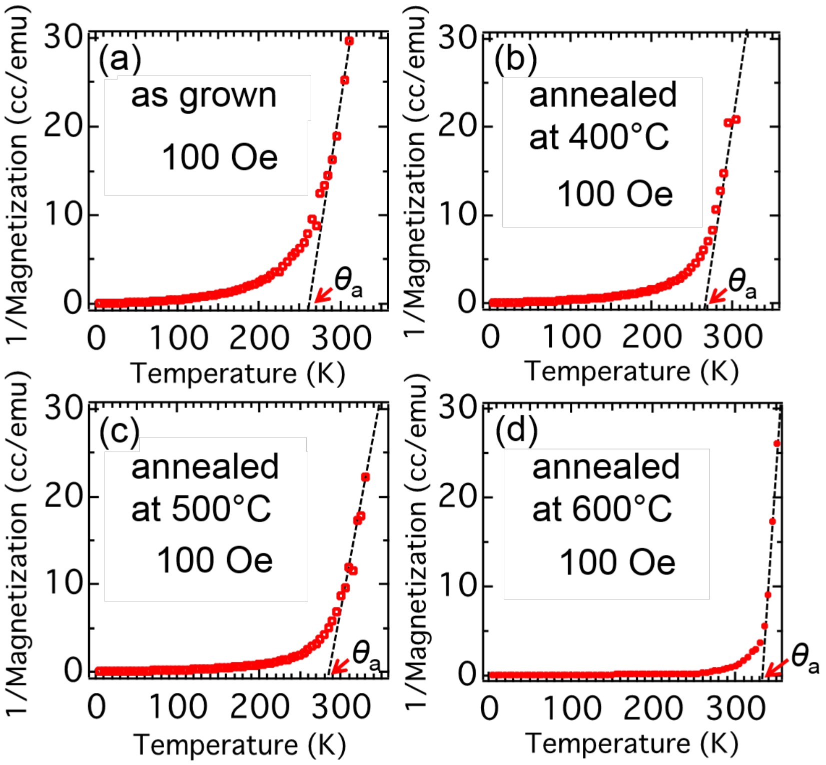

Fig. 25. (a)-(d) Inverse of M versus temperature ($1/M$-T) curves of the $Ge_{0.895}Fe_{0.105}$ samples (a) as grown and annealed at (b) 400, (c) 500, and (d) 600°C. The measurements were performed in the FC process. [Y. K. Wakabayashi *et al.*, Physical Review B **90**, 205209 (2014).]

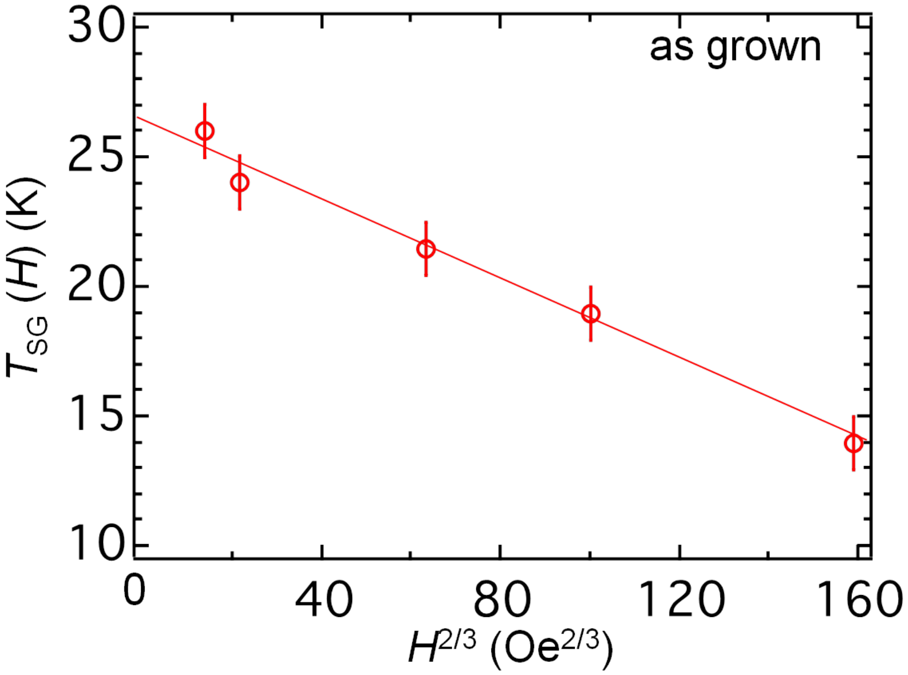

Fig. 26. Magnetic-field H dependence of the spin-glass transition temperature $T_{SG}(H)$ of the as-grown $Ge_{0.895}Fe_{0.105}$ film with the AT line. [Y. K. Wakabayashi *et al.*, Physical Review B **90**, 205209 (2014).]

The M - T curves in Fig. 25 are characterized by the irreversibility between the ZFC and FC processes. In all the samples, a cusp is seen at around 15 K in the ZFC curves, being a characteristic feature of a magnetic random system like a spin glass. The similar phenomena were observed in III-V-based FMS GaMnAs,[67] II-VI-based FMS ZnCrTe,[35] and AuFe alloys.[68] In GaMnAs, this magnetic randomness comes from the difference of magnetic anisotropy between the low and high hole concentration regions,[67] while it comes from existence of the antiferromagnetic interaction due to the RKKY interaction in AuFe alloys. In GeFe, it does not originate from the ferromagnetic intermetallic precipitates but from the non-uniform distribution of Fe atoms which is observed by the EDX measurements. The position of the cusps is insensitive to the annealing temperature, indicating that the annealing does not much influence this weak spin-glass-like behavior. Here, the spin-glass transition temperature $T_{SG}(H)$, which is related to a typical scale of the anisotropy-energy barriers in the system, is defined as the temperature at which the difference between the M values in ZFC and FC processes appears when a magnetic field of H (Oe) is applied perpendicular to the film plane. When a material system is in a spin-glass-like phase, it is well known that $T_{SG}(H)$ follows the de Almeida-Thouless (AT) line[69] given by

$$T_{SG}(H) = T_{SG}(0)(1 - \alpha H^{\frac{2}{3}}), \tag{17}$$

where α is a constant. Figure 26 shows the H dependence of the $T_{SG}(H)$ of the as-grown

$Ge_{0.895}Fe_{0.105}$ film with the AT line. In Fig. 26, we see that $T_{SG}(H)$ linearly decreases as $H^{2/3}$ increases, meaning that the weak spin-glass-like behavior appears in the very low temperature region at $T < T_{SG}(H)$.[70] The extrapolation of the AT line back to $H = 0$ gives the spin glass transition temperature $T_{SG}(0)$ at zero magnetic field, which is estimated to be ~26 K in this case. Alternative-current susceptibility measurements may help more detailed understanding of it; however it is difficult to measure it due to its small magnetic moment.

The notable point is that, when annealed at 600°C, the sample shows another cusp at 260 K in the ZFC process shown in Fig. 24 (d), which indicates the occurrence of phase separation and superparamagnetism. Moreover, the magnetic moment persists up to room temperature, indicating that the nano-particles, which have the high Fe concentration with the periodic twins and stacking faults, have a high T_C value up to room temperature. These results obtained by SQUID show that the magnetic phase separation occurs at 600°C, being consistent with the crystallographic and MCD analyses mentioned above.

In the case of the GeMn granular films, an α-phase, which is very difficult to be distinguished from the host lattice only by the [110]-projection TEM image, has been observed in the GeMn nano-columns.[71,72] In the case of our single-phase GeFe films, we can exclude the possibility of the existence of such nano-columns because the surface of the GeFe films is very smooth with a small root-mean-square roughness r_{RMS} of 0.33 nm, which is comparable to that of the pure Ge film grown by LT-MBE,[73] and we do not see any clear structures suggesting the existence of the nano-columns on the surface. However, there might be a possibility that the α-phase is embedded in the diamond crystal structure without any clear visible interface. We have carried out the c-RBS and c-PIXE measurements (See section 3. 1), by which the Fe atoms in the α-phase (if any) can be distinguished from the substitutional Fe atoms. In the $Ge_{0.935}Fe_{0.065}$ films grown at 160 and 240°C, we have found that ~85% of the doped Fe atoms exist at the substitutional sites and ~15% of the doped Fe atoms exist at the interstitial sites. We have also clarified that T_C of GeFe is not correlated with the density of the Fe interstitials. Thus, even if the embedded α-phase exists in our films, it does not seem to be related to the ferromagnetism.

In the above sections, we have found that single-phase GeFe has the three critical temperatures; T_C, θ_a, and $T_{SG}(0)$. From these three critical temperatures, we can infer the magnetic state in GeFe. Figure 27(a)-(d) shows the schematic diagrams of the magnetic states in the GeFe films after the sample was cooled down to 5 K from room temperature without a

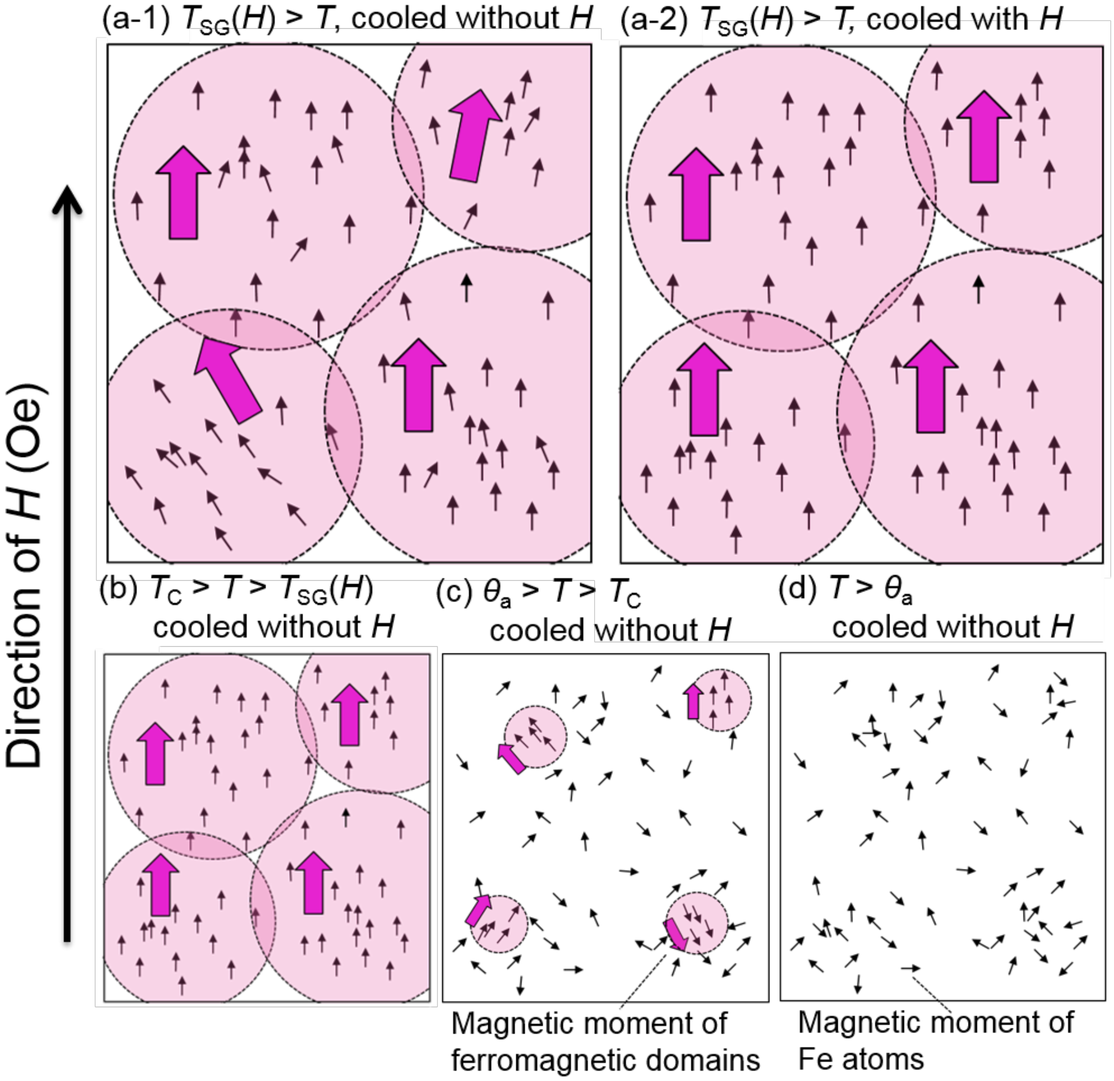

Figure 27. Schematic diagrams of the magnetic states in the GeFe films after the sample was cooled down to 5 K from room temperature without a magnetic field and then temperature (T) is gradually increased with a magnetic field H (Oe) applied perpendicular to the film plane; (a-1) $T_{SG}(H) > T$, (b) $T_C > T > T_{SG}(H)$, (c) $\theta_a > T > T_C$, (d) $T > \theta_a$, corresponding to the ZFC measurements, and (a-2) the one after the sample was cooled down to T from room temperature with a magnetic field when $T_{SG}(H) > T$, corresponding to the FC measurements.

magnetic field and then temperature (T) is gradually increased with a magnetic field H (Oe) applied perpendicular to the film plane; (a-1) $T_{SG}(H) > T$, (b) $T_C > T > T_{SG}(H)$, (c) $\theta_a > T > T_C$, (d) $T > \theta_a$, corresponding to the ZFC measurements. Fig. 27 (a-2) shows the one after the sample was cooled down to T from room temperature with a magnetic field when $T_{SG}(H) > T$, corresponding to the FC measurements. Each small black arrow and big arrow represent the magnetic moment of each Fe atom and local ferromagnetic region, respectively. We note that, when $T > T_{SG}(H)$, the magnetic states in the ZFC and FC measurements are the same for the

GeFe as grown and annealed at 400 and 500°C. In the high temperature region above θ_a, every Fe atom shows the paramagnetic behavior [Fig. 27 (d)]. When $\theta_a > T > T_C$, the local ferromagnetic regions, that are formed by the short-range interaction, appear in the locally high-Fe-concentration regions, resulting in the deviation from the Curie-Weiss law [Fig. 27 (c)]. With decreasing T further, these local ferromagnetic regions become larger, and the ferromagnetic transition of the whole system occurs at T_C [Fig. 27 (b)]. Finally, the weak spin-glass-like behavior appears below $T_{SG}(H)$ [Fig. 27 (a-1) and (a-2)]. We note that the hysteresis loops obtained in our single-phase films are not affected by this weak spin-glass-like behavior since this behavior is broken due to the initial magnetization process before the measurements. In section 3. 3, more detailed microscopic magnetization process in GeFe are observed by using XMCD.

The magnetic interaction in single-phase GeFe is complex because there is the magnetic randomness which comes from the non-uniform distribution of Fe atoms, which results in the weak spin-glass-like behavior at the very low temperature. However, the ferromagnetic interaction is obviously dominant because the T_C and θ_a values are much higher than T_{SG} and because more than half of M remains in the ZFC process even at 4 K. The origin of the ferromagnetic interaction is the *s*,*p*-*d* exchange interaction, which is confirmed by the enhancement of the E_1 peak in the MCD spectra [Fig. 21(a)]. The annealing enhances this FM interaction, resulting in the increase in T_C and θ_a. Our results show that the increase in T_C is correlated with the enhancement of the non-uniformity of Fe atoms. In FMSs, such an increase in T_C with the enhancement of the non-uniformity of magnetic impurities is predicted theoretically.[57,74] Thus, to achieve room-temperature ferromagnetism, higher Fe concentration and adequate enhancement of the non-uniformity of Fe atoms are needed.

In Fig. 22 (a), the MCD-B curve at 240 K, which is above T_C (= 210 K), has a large curvature, suggesting the existence of the superparamagnetism. This does not originate from the FM intermetallic precipitates but from the local FM regions due to the non-uniform distribution of Fe atoms. This result also supports the model that the FM interactions between the Fe atoms in the locally high-Fe-concentration regions are still remaining above T_C, as mentioned above.

The T_C values of the already-known equilibrium Fe-Ge compound phases are much higher than room temperature,[75-77] which suggests that the FM nano-particles obtained by the annealing at 600°C in this study are an unknown magnetic phase, which has a diamond crystal structure with periodic twins and stacking faults. The high T_C of the nano-particles may originate from the high Fe concentration, quantum confinement, or band structure modulation associated with the formation of twins.[78] The twin boundaries are viewed to be a regional wurtzite structure so these nano-particles, which include periodic twin boundaries, may change their band structure and physical properties.

In summary of this section, the annealing of the GeFe thin film in a nitrogen atmosphere was shown to be quite effective to enhance the ferromagnetism of GeFe. When the annealing temperature is lower than 600°C, T_C is increased up to 210 K while the film keeps the nearly single FMS phase. When it is annealed at 600°C, the FM nano-particles with a high T_C up to room temperature, which have a diamond crystal structure with twins and stacking-faults, are formed in the GeFe film. We have clarified that the inhomogeneity of the Fe concentration plays an essential role in determining the ferromagnetism. The ferromagnetism is much stronger than the weak spin-glass-like behavior, which is caused by the non-uniform distribution of the Fe atoms, and it dominates the system. Both types of films have good compatibility with group IV (Ge and Si) semiconductor materials and devices, and thus they are very promising for realizing Si-based spin devices.

3. 3. XMCD measurements

Despite the attractive features of GeFe, detailed microscopic understanding of the ferromagnetism in GeFe, which is vitally important for room-temperature applications, is lacking. In this section, we investigate the local electronic and magnetic properties of GeFe using XAS and XMCD,[79] which are powerful techniques for element-specific detection of local electronic states and magnetic moments.[80-84] We find that nanoscale local FM regions remain in the GeFe films even at room temperature, i.e., well above T_C; it follows that GeFe potentially has strong ferromagnetism, which persists even at room temperature. Furthermore, we observe the intriguing feature that FM regions, which are formed above T_C via the FM exchange interaction in high-Fe concentration regions of the films, develop and expand as the temperature decreases, and that all of them coalesce at temperatures below T_C. Such a nanoscale expansion of the FM regions is a key feature in understanding materials that exhibit single-phase ferromagnetism despite the inhomogeneous distribution of magnetic atoms in the film.[29,32,85,86]

We carried out XMCD measurements on two samples (labeled A and B) consisting of a 120-nm-thick $Ge_{0.935}Fe_{0.065}$ layer grown on a Ge(001) substrate by low-temperature molecular beam epitaxy (LT-MBE) [Fig. 28(a),(b)]. The $Ge_{0.935}Fe_{0.065}$ layer of sample A was grown at 160°C, whereas that of sample B was grown at 240°C. These samples are the same as those studied in section 3.1 and 3.4. From the Arrott plots of the H dependence of the MCD measured with visible light with a photon energy of 2.3 eV (corresponding to the L-point energy gap of bulk Ge), we found $T_C = 20$ K and 100 K for samples A and B, respectively. Detailed crystallographic analyses, including *in situ* RHEED, HRTEM, spatially resolved TED combined with EDX, and XRD, showed that the GeFe films have a diamond-type single-crystal structure without any ferromagnetic precipitates and with nanoscale spatial Fe concentration fluctuations of 4% – 7% (sample A) and 3% – 10% (sample B) (see section 3.1). We found that T_C is higher when the fluctuations in the Fe concentration are larger. In addition, c-RBS and c-PIXE measurements showed that ~85% (~15%) of the doped Fe atoms exist at the substitutional (tetrahedral interstitial) sites in both samples A and B, and that the interstitial Fe concentration is not related to T_C. This also indicates that there are *no* FM precipitates with different crystal structures in our films.

We performed XAS and XMCD measurements at the soft X-ray beamline BL23SU of SPring-8 with a twin-helical undulator of in-vacuum type.[87] The monochromator resolution was $E/\Delta E > 10000$. The XAS and XMCD spectra were obtained by reversing photon helicity at each energy point and were recorded in the total-electron-yield (TEY) mode. The XMCD spectra were taken both for positive and negative applied magnetic fields and were averaged in order to eliminate experimental artifacts. Backgrounds of the XAS spectra at the Fe $L_{2,3}$-edge were assumed to be hyperbolic tangent functions. To remove the oxidized surface layer, the samples were briefly etched in dilute HF prior to loading into the XAS (XMCD) vacuum chamber.

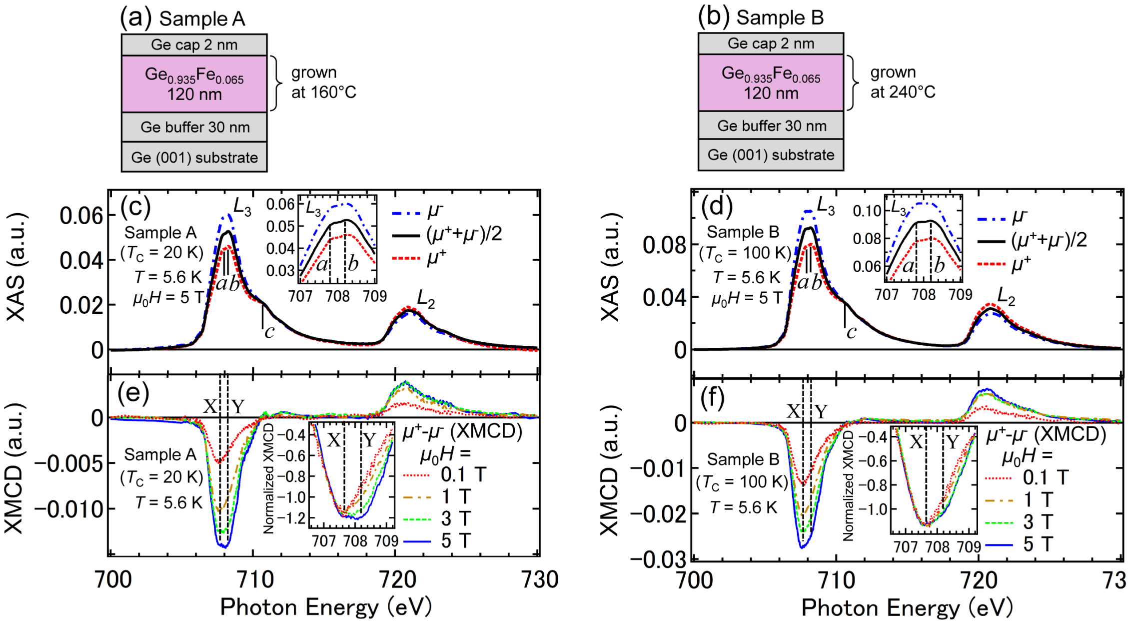

Figure 28. (a),(b) Schematic sample structures of (a) sample A and (b) sample B. (c),(d) XAS spectra of μ^-, μ^+ and $(\mu^+ + \mu^-)/2$ at the L_2 (~721 eV) and L_3 (~708 eV) absorption edges of Fe for (c) sample A and (d) sample B measured at 5.6 K with $\mu_0 H = 5$ T applied perpendicular to the film surface. The insets show a magnified plot of the spectra at the Fe L_3 edge. (e),(f) XMCD ($= \mu^+ - \mu^-$) spectra at the L_2 and L_3 absorption edges of Fe for (e) sample A and (f) sample B measured at 5.6 K with various H applied perpendicular to the film surface. The insets show a magnified plot of the spectra at the Fe L_3 edge, in which the XMCD data are normalized to 707.3 eV. [Y. K. Wakabayashi *et al.*, Scientific Reports **6**, 23295 (2016).]

We measured the Fe $L_{2,3}$-edge XAS spectra [μ^+, μ^- and $(\mu^+ + \mu^-)/2$] of samples A [Fig. 28(c)] and B [Fig. 28(d)] at 5.6 K with $\mu_0 H = 5$ T applied perpendicular to the film surface. Here, μ^+ and μ^- refer to the absorption coefficients for photon helicity parallel and antiparallel to the Fe 3*d* majority spin direction, respectively. In both films, three peaks *a*, *b* and *c* are observed at the Fe L_3 edge in the XAS spectra [see also the insets in Fig. 28(c),(d)]. We found that the small peak *c* was suppressed by etching the surface with dilute HF, indicating that this peak, which can be assigned to the Fe^{3+} state, originates from a small quantity of surface Fe oxide,[88] which remains even after surface cleaning. Meanwhile, peaks *a* and *b* are assigned to the Fe atoms in GeFe. Peaks *a* and *b* can be assigned to the Fe^{2+} state.[89,90]

We measured the Fe $L_{2,3}$-edge XMCD ($= \mu^+ - \mu^-$) spectra of samples A [Fig. 28(e)] and B [Fig. 28(f)] at 5.6 K with various *H* applied perpendicular to the film surface. Here, we discuss the XMCD intensities at 707.66 eV (X) and 708.2 eV (Y), which correspond to the photon energies of peaks *a* and *b* in the XAS spectra, respectively. When normalized to 707.3 eV, the XMCD spectra with various *H* differ, and the intensity at X grows faster than that at Y as *H* increases, as shown in the insets of Fig. 28(e),(f). As shown in Fig. 28(c),(d), the shapes of the XAS spectra at the Fe L_3 edge are similar between samples A and B, which have almost the same interstitial Fe concentrations (i.e., 15% of the total Fe content); therefore, we can assign the XMCD intensity at X to the substitutional Fe atoms and the paramagnetic component of the XMCD intensity at Y to the interstitial Fe atoms. We do not observe fine structures due to multiplet splitting at the Fe L_3 edge in both samples, which would be observed if the 3*d* electrons were localized and were not strongly hybridized with other orbitals.[91] These observations indicate that the Fe 3*d* electrons are strongly hybridized with the Ge 4*p* states.[92]

We determine the orbital magnetic moment, m_{orb}, and the spin magnetic moment, m_{spin}, the orbital magnetic moment relative to the spin magnetic moment, $m_{\text{orb}}/m_{\text{spin}}$, and the total magnetic moment, $M = m_{\text{spin}} + m_{\text{orb}}$, of the *substitutional* Fe atoms in accordance with the well-established procedure using the XMCD sum rules.[24,34,93-95] Figure 29(a) shows the XAS spectra (solid curves) and the XAS signals integrated from 690 eV (dashed curves) of sample A. Figure 30(b) shows the XMCD spectra (solid curves) and the XMCD signals integrated from 690 eV (dashed curves) of sample A. Here, the measurements were carried out with a magnetic field $\mu_0 H = 5$ T applied perpendicular to the film surface at various temperatures. Figure 29(c),(d) shows the same data measured for sample B. For the XMCD sum-rules analyses, we define *r*, *p* and *q* as the following equations at each temperature.

$$r = \int_{E_3+E_2} \frac{(\mu^+ + \mu^-)}{2} dE, \tag{18}$$

$$p = \int_{E_3} (\mu^+ - \mu^-) dE, \tag{19}$$

$$q = \int_{E_3+E_2} (\mu^+ - \mu^-) dE, \tag{20}$$

where E_3 (690-718 eV) and E_2 (718-760 eV) represent the integration energy ranges for the L_3 and L_2 absorption edges, respectively. Here, E represents the incident photon energy. We can obtain m_{spin} and m_{orb} of substitutional Fe atoms using the XMCD sum rules, which are expressed as follows:

$$m_{\mathrm{orb}} = -\frac{2q}{3r}(10 - n_{3d}), \tag{21}$$

$$m_{\mathrm{spin}} + 7m_{\mathrm{T}} = -\frac{3p-2q}{r}(10 - n_{3d}), \tag{22}$$

where n_{3d} and m_{T} are the number of 3*d* electrons on the Fe atom and the expectation value of the intra-atomic magnetic dipole operator, respectively. We neglect m_{T} because it is negligibly small for Fe atoms at the T_{d} symmetry site.[34] By dividing equation (21) by equation (22), $m_{\mathrm{orb}}/m_{\mathrm{spin}}$ is expressed by

$$m_{\mathrm{orb}}/m_{\mathrm{spin}} \approx \frac{2q}{3(3p-2q)}. \tag{23}$$

Thus, we can obtain $m_{\mathrm{orb}}/m_{\mathrm{spin}}$ directly from the XMCD spectra without any assumptions.

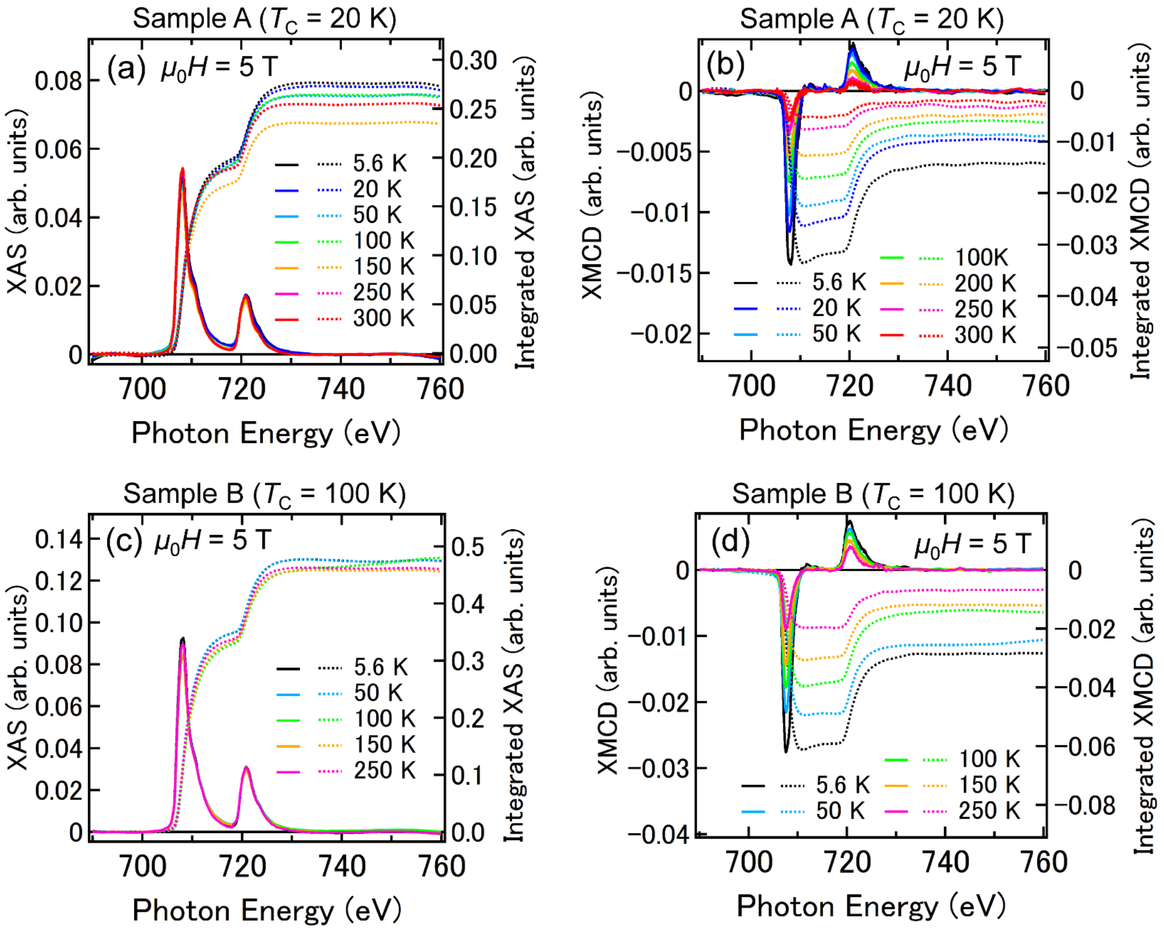

Figure 29. (a),(c) XAS [= ($\mu^+ + \mu^-$)/2] spectra (solid curves) and the XAS signals integrated from 690 eV (dashed curves) of (a) sample A and (c) sample B. (b),(d) XMCD (= $\mu^+ - \mu^-$) spectra (solid curves) and the XMCD signals integrated from 690 eV (dashed curves) of (b) sample A and (d) sample B. These measurements were carried out with a magnetic field $\mu_0 H$ = 5 T applied perpendicular to the film surface at 5.6 K (black curves), 20 K (blue curves), 50 K (light blue curves), 100 K (green curves), 150 K (orange curves), 250 K (pink curves), and 300 K (red curves). [Y. K. Wakabayashi *et al.*, Scientific Reports **6**, 23295 (2016).]

By the above calculations with equations (19), (20) and (23) using the temperature dependence of XMCD spectra shown in Fig. 29, we obtained the temperature dependence of $m_{\mathrm{orb}}/m_{\mathrm{spin}}$ of substitutional Fe atoms as shown in Fig. 30(a),(b). For sample A, $m_{\mathrm{orb}}/m_{\mathrm{spin}} = 0.12 \pm 0.02$, and for sample B, $m_{\mathrm{orb}}/m_{\mathrm{spin}} = 0.11 \pm 0.03$, both of which are positive and larger than that of bulk Fe (where $m_{\mathrm{orb}}/m_{\mathrm{spin}} \sim 0.043$[91]); the orbital angular momentum in GeFe is not quenched. The observation that the spin and orbital angular momentum are parallel suggests that the Fe 3*d* shell is more than half filled. This implies that the Fe atoms are in the 2+ state rather than in the 3+ state, in which the Fe 3*d* shell is half-filled and the orbital angular momentum vanishes. This result is consistent with the peak positions of the XAS spectra [see Fig. 28(c),(d)]. The large m_{orb} is a characteristic property of GeFe, and excludes the possibility of the existence of ferromagnetic Fe metal precipitates in our films.

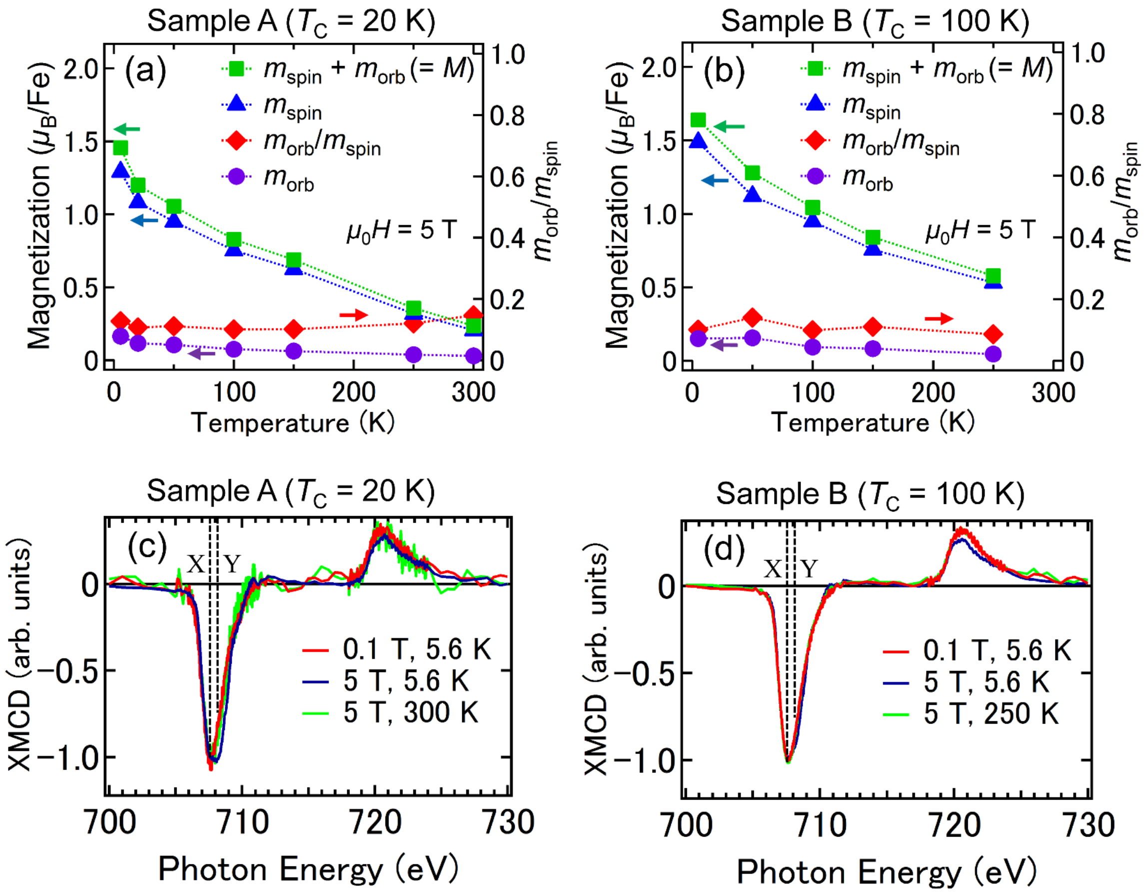

Figure 30. (a),(b) Temperature dependence of $m_{spin} + m_{orb}$, m_{spin}, m_{orb}, and m_{orb}/m_{spin} for (a) sample A and (b) sample B with an applied magnetic field of $\mu_0H = 5$ T. (c),(d) XMCD spectra of (c) samples A and (d) sample B normalized to 707.3 eV measured at 5.6 and 300 K with magnetic fields of 0.1 and 5 T applied perpendicular to the film surface. [Y. K. Wakabayashi *et al.*, Scientific Reports **6**, 23295 (2016).]

We describe the derivation of m_{spin} and m_{orb} using equations (21) and (22). Figure 30(c),(d) shows the XMCD spectra of samples (c) A and (d) B normalized to 707.3 eV measured at 5.6 and 300 K with magnetic fields of 0.1 and 5 T applied perpendicular to the film surface. In both films, all the line shapes of the XMCD spectra are almost the same, which means that the paramagnetic component observed at Y in Fig. 28(e),(f) is negligibly small in comparison with the entire XMCD spectra and almost all XMCD intensities are composed of the absorptions by the substitutional Fe atoms observed at X in Fig. 28(e),(f). This result means that the integrated values of the XMCD spectra p [equation (19)] and q [equation (20)] can be attributed only to the substitutional Fe atoms. Meanwhile, because the XAS signals have both contributions of the substitutional and interstitial Fe atoms, we reduced the integrated XAS intensity r [equation (18)] to 85% of its raw value (85% is the approximate ratio of the density of the substitutional Fe atoms to that of the total Fe atoms in both samples A and B) when using the XMCD sum rules. We note that this assumption, that each substitutional Fe atom and each interstitial Fe atom contribute equally to the integrated XAS intensity [r value (equation (18))], does not affect our main conclusions in this section. We took n_{3d} to be 6 and the correction factor for m_{spin} to be 0.88[95] for Fe^{2+} in equations (21) and (22). By the above calculations using the temperature dependence of XAS and XMCD spectra shown in Fig. 29, we obtained the temperature dependence of m_{spin}, m_{orb} and m_{spin} + m_{orb} (=M) of substitutional Fe atoms shown in Fig. 30(a),(b). The M values obtained by the XMCD measurements are 1.00 μ_B/Fe for sample A and 1.43 μ_B/Fe for sample B when a magnetic field $\mu_0 H$ = 1 T is applied perpendicular to the film surface at 5.6 K. The magnetizations measured by SQUID under the same condition at 5 K are 0.7 μ_B/Fe for sample A and 1.3 μ_B/Fe for sample B. These values are close to those obtained by XMCD. The slight differences may originate from the unavoidable inaccuracy of the subtracting procedure of the large diamagnetic response of the substrate in the SQUID measurements. We see that both m_{spin} and m_{orb} (and therefore the total magnetic moment $M = m_{\mathrm{spin}} + m_{\mathrm{orb}}$) are larger in sample B (T_C = 100 K) than in sample A (T_C = 20 K) over the entire temperature region when $\mu_0 H$ = 5 T.

Figure 31(c) shows the magnetization versus temperature (M - T) curves of sample B measured by SQUID. In the ZFC process shown by the blue curve, M was measured with H = 100 Oe applied perpendicular to the film surface with increasing temperature after the sample was cooled down to 4 K from room temperature without a magnetic field. In the field-cooling FC process shown by the red curve, M was measured with decreasing temperature from room temperature to 4 K under H = 100 Oe applied perpendicular to the film surface. The inset shows a magnified plot near 0 K. At very low temperature, we see a slight difference between the M values in ZFC and FC processes, which means that there is a weak spin-glass phase in the film only at very low temperatures.[32] The spin-glass transition temperature T_{SG}(100 Oe), which is defined as the temperature at which the difference between the M values in ZFC and FC processes appears when H is 100 Oe, is 10 K in sample B. As described in section 3.2, this value is lower than that of the $\mathrm{Ge}_{0.895}\mathrm{Fe}_{0.105}$ film grown at 240°C (i.e. T_{SG}(100 Oe) $\approx$ 24 K), which has a spin-glass transition temperature T_{SG}(0 Oe) of ~26 K. This result means that the T_{SG}(0 Oe) of sample B is lower than 26 K. The T_C value of sample B (100 K) is much higher than T_{SG}(0 Oe) (< 26 K), and more than 80% of M remains in the ZFC process even at 4 K [Fig. 31(c)]. Therefore, the ferromagnetism is much stronger than the spin-glass phase and is dominant in the entire temperature region below T_C. In the case of the superparamagnetic particles with slow relaxation, the magnetic hysteresis is only observed below the blocking temperature. Furthermore, the MCD hysteresis curve did not depend on the sweeping speed of the magnetic field unlike superparamagnetic materials with spin blocking [see Fig. 31 (a),(b)].[96,97] Thus, we can conclude that the GeFe films are ferromagnetic below T_C.

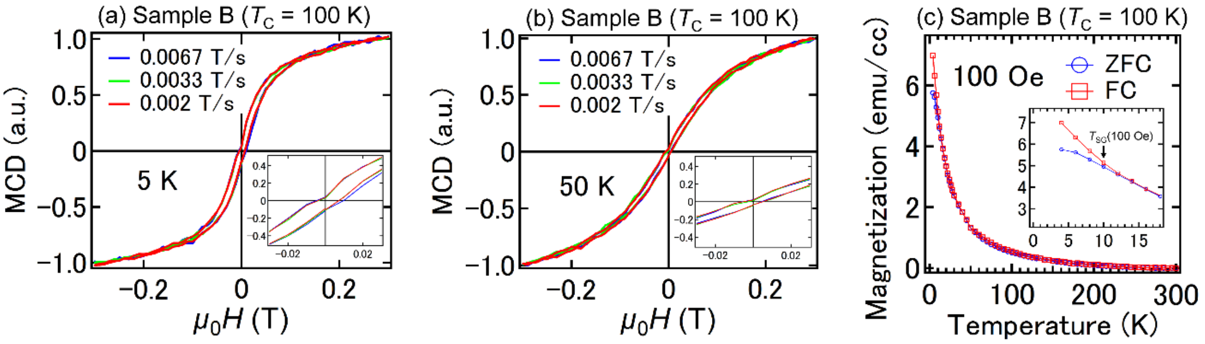

Figure 31. (a),(b) The *H* dependence of the MCD intensity for sample B at (a) 5 K and (b) 50 K with a photon energy of 2.3 eV measured at different sweeping speeds of *H* applied perpendicular to the film surface. (c) Magnetization versus temperature (*M*-*T*) curves of sample B. The measurements were performed in the two processes of field cooling (FC, red curve) and zero field cooling (ZFC, blue curve) with *H* = 100 Oe applied perpendicular to the film surface. [Y. K. Wakabayashi *et al.*, Scientific Reports **6**, 23295 (2016).]

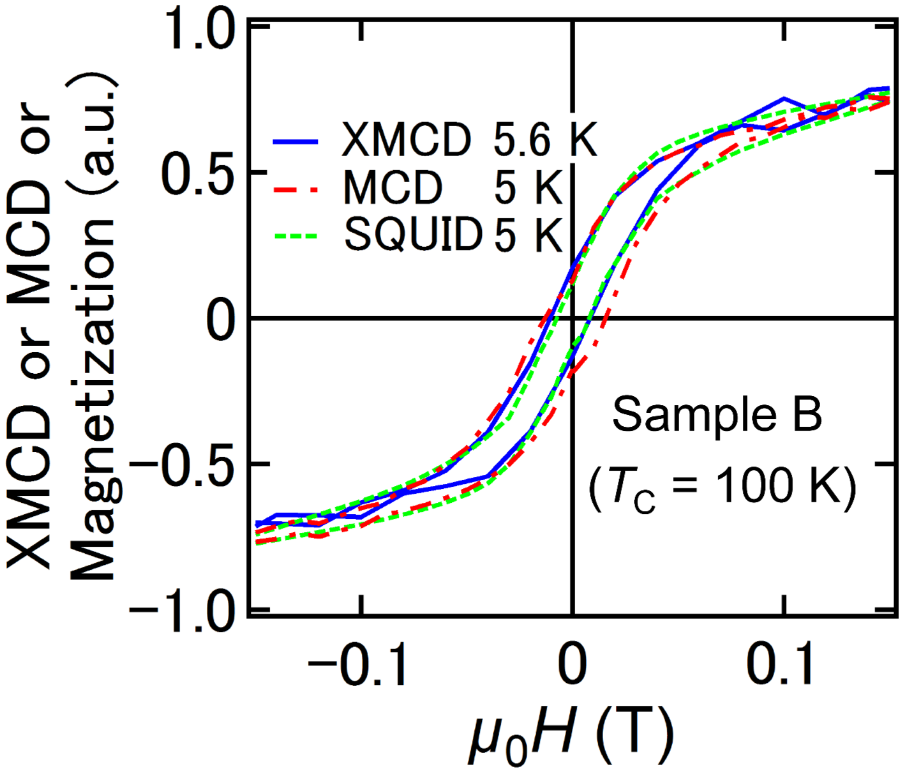

Figure 32. The *H* dependence of the XMCD intensity at X shown in Fig. 29 (707.66 eV) at 5.6 K, the MCD intensity at 5 K with a photon energy of 2.3 eV corresponding to the *L*-point energy gap of bulk Ge, and the magnetization measured using a SQUID at 5 K for sample B. [Y. K. Wakabayashi *et al.*, Scientific Reports **6**, 23295 (2016).]

Figure 32 shows the H dependence of the XMCD intensity at energy X and a temperature of 5.6 K, the MCD intensity measured with visible light of 2.3 eV at 5 K, and the magnetization measured using a SQUID at 5 K for sample B. The shapes of these curves show excellent agreement with each other; it follows that the spin splitting of the valence band composed of the Ge 4p orbitals is induced by the Fe 3d magnetic moment, which originates from the substitutional Fe atoms, through the p-d hybridization.

Figure 33(a),(b) shows the effective magnetic-field (H_{eff}) dependence of the XMCD intensity measured at X for samples (a) A and (b) B at various temperatures. Here, M is also plotted (filled red symbols), and $\mu_0 H_{\mathrm{eff}}$ is obtained by subtracting the product of M and the density of the substitutional Fe atoms from $\mu_0 H$ to eliminate the influence of the demagnetization field. The insets show clear hysteresis below T_{C} in both samples. The XMCD – H_{eff} curves show large curvature above T_{C} in both samples [see the main panels of Fig. 33(a),(b)], indicating that part of the film is superparamagnetic (SPM) above T_{C}. It indicates that local ferromagnetic regions form in nanoscale high-Fe concentration regions at temperatures above T_{C}, and thus M can be described by

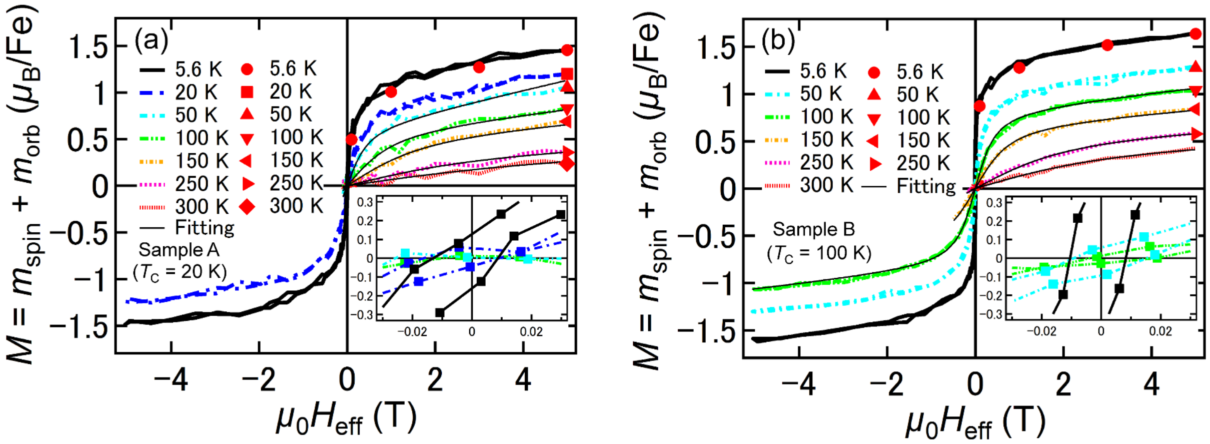

Figure 33. (a),(b) The dependence of the XMCD intensity measured at X on the effective magnetic field H_{eff} for (a) sample A and (b) sample B at various temperatures. The total magnetization ($M = m_{\mathrm{spin}} + m_{\mathrm{orb}}$) obtained using the XMCD sum rules is also plotted (filled red symbols). We scaled the vertical axis of the XMCD intensity so that it represents M at each temperature. In all measurements, H was applied perpendicular to the film surface. [Y. K. Wakabayashi *et al.*, Scientific Reports **6**, 23295 (2016).]

$$M = 4.4\mu_{\mathrm{B}} f_{\mathrm{SPM}} L\left(\frac{m_{\mathrm{SPM}}\mu_0 H_{\mathrm{eff}}}{k_{\mathrm{B}} T}\right) + (1\text{-}f_{\mathrm{SPM}})\frac{C}{T}\mu_0 H_{\mathrm{eff}}, \qquad (24)$$

where f_{SPM} and m_{SPM} are fitting parameters expressing the fraction of SPM substitutional Fe atoms and the magnetic moment per local ferromagnetic region, respectively. Also, C is the Curie constant per substitutional Fe atom, and L is the Langevin function. Here, $4.4\mu_{\mathrm{B}}$ is the *ideal* saturated value of M; i.e., $M = m_{\mathrm{spin}} + (m_{\mathrm{orb}}/m_{\mathrm{spin}}) \times m_{\mathrm{spin}}$, where $m_{\mathrm{spin}} = 4\ \mu_{\mathrm{B}}$ (for Fe^{2+}) and $m_{\mathrm{orb}}/m_{\mathrm{spin}} \approx 0.1$ [Fig. 30(a),(b)] when all the substitutional Fe atoms are magnetically active. Here, the Curie constant per substitutional Fe atom is obtained using the following equations:

$$C = \frac{\mu_{\mathrm{B}}^2}{3k_{\mathrm{B}}} n_{\mathrm{B}}^2, \tag{25}$$

$$n_{\mathrm{B}} = \left[\frac{3}{2} + \frac{S(S+1) - L(L+1)}{2J(J+1)}\right]\sqrt{J(J+1)}, \tag{26}$$

where μ_{B}, k_{B}, n_{B}, S, L and J represent the Bohr magneton, the Boltzmann constant, the effective Bohr magneton number, the spin angular momentum, the orbital angular momentum and the total angular momentum, respectively. Here, $S = 2$ (for Fe^{2+}), and $L = 0.4$ [$L = 2S \times m_{\mathrm{orb}}/m_{\mathrm{spin}}$, where $m_{\mathrm{orb}}/m_{\mathrm{spin}} \approx 0.1$ as shown in Fig. 30(a),(b)], and $J = 2.4$ ($= L + S$ because the spin and orbital angular momenta of a substitutional Fe atom are parallel) in equation (26). Thus, n_{B} is estimated to be 5.24. The first and second terms in equation (24) correspond to the SPM and paramagnetic components, respectively. In Fig. 33(a),(b), the thin black solid curves correspond to the best fit obtained with equation (24). For sample B, the $M - H_{\mathrm{eff}}$ curves at temperatures in the range 100 – 300 K are well reproduced by equation (24), which indicates that the FM – SPM transition occurs at $T_{\mathrm{C}} = 100$ K. With sample A, the $M - H_{\mathrm{eff}}$ curves at temperatures above T_{C} (i.e., $T \geq 20$ K) are well reproduced by equation (24), except for $T = 20$ K, which is probably due to the onset of ferromagnetism. These good fits up to room temperature indicate that FM interactions within the nanoscale high-Fe concentration regions remain at room temperature in both samples.

Here, we estimate the ratios of the substitutional FM, paramagnetic, and magnetically inactive Fe atoms to the total number of substitutional Fe atoms at 5.6 K in samples A and B. In this discussion, we only consider substitutional Fe atoms. The obtained results are summarized in Table 1. At 5.6 K, in principle, the H_{eff} dependence of M ($= m_{\mathrm{spin}} + m_{\mathrm{orb}}$) of one substitutional *paramagnetic* Fe atom is expressed by the Langevin function. Thus, theoretically, the H_{eff} dependence of M of one substitutional paramagnetic Fe atom at 5.6 K is obtained by substituting $4.4\mu_{\mathrm{B}}$, 1 and 5.6 K in m_{SPM}, f_{SPM} and T of equation (24), respectively (Fig. 34). Here, the experimental M-H_{eff} curves at 5.6 K shown in Fig. 33(a),(b) can be approximately expressed by the sum of the square hysteresis curve originating from substitutional ferromagnetic Fe atoms and the Langevin function originating from substitutional paramagnetic Fe atoms. From the high-field magnetic susceptibility $\partial M/\partial(\mu_0 H_{\mathrm{eff}})$ (μ_{B}/T per Fe) of the M-H_{eff} curve, we can estimate the fraction of the substitutional paramagnetic Fe atoms. We approximated $\partial M/\partial(\mu_0 H_{\mathrm{eff}})$ by the slope of the M-H_{eff} line from 4 T to 5 T. In this way, from Fig. 34, the theoretical $\partial M/\partial(\mu_0 H_{\mathrm{eff}})$ value is estimated to be 0.33 μ_B/T per one substitutional paramagnetic Fe (slope of the black dashed line in Fig. 34). As shown in Fig. 33(a),(b), the experimental $\partial M/\partial(\mu_0 H_{\mathrm{eff}})$ values at 5.6 K in samples A and B are 0.08 μ_B/T and 0.06 μ_B/T, respectively; it follows that the ratios of the substitutional paramagnetic Fe atoms to the total number of substitutional Fe atoms are ~24% (= 0.08/0.33) in sample A and ~18% (= 0.06/0.33) in sample B. Next, we estimate the fraction of substitutional ferromagnetic Fe atoms. The extrapolated M value from the high magnetic field region to $H_{\mathrm{eff}} = 0$ in Fig. 33(a),(b) is 1.1 μ_B per Fe atom in sample A, and 1.3 μ_B per Fe atom in sample B at 5.6 K. Because the M-H_{eff} curve of the substitutional paramagnetic Fe atoms is expressed by the Langevin function at this temperature as mentioned above, these extrapolated M values include a contribution of the substitutional paramagnetic Fe atoms, which is estimated by a linear extrapolation of M to $H_{\mathrm{eff}} = 0$ in the M-H_{eff} curve of the substitutional paramagnetic Fe atoms. In Fig. 34, for one substitutional paramagnetic Fe atom, it is 1.1 μ_B per Fe. Thus, the contribution of the substitutional paramagnetic Fe atoms to the extrapolated M value is experimentally ~0.26 μ_B (= 1.1 μ_B × 0.24) per Fe for sample A and ~0.20 μ_B (= 1.1 μ_B × 0.18) per Fe for sample B. These results suggest that only ~19% [= (1.1-0.26)/4.4] and ~25% [= (1.3-0.20)/4.4] of the substitutional Fe atoms are ferromagnetic in samples A and B, respectively. This result means that 57% (=100-24-19 for sample A and 100-18-25 for sample B) of the substitutional Fe atoms do not contribute to the total magnetization. We think that some fraction of these substitutional magnetically inactive Fe atoms couple antiferromagnetically. This is also supported by the weak spin-glass behaviour observed in GeFe at very low temperatures.[32]

Table 1. Ratios of the substitutional ferromagnetic, paramagnetic, and magnetically inactive Fe atoms to the total number of substitutional Fe atoms at 5.6 K in samples A and B. [Y. K. Wakabayashi *et al.*, Scientific Reports **6**, 23295 (2016).]

Sample	Ferromagnetic	Paramagnetic	Inactive
A	19%	24%	57%
B	25%	18%	57%

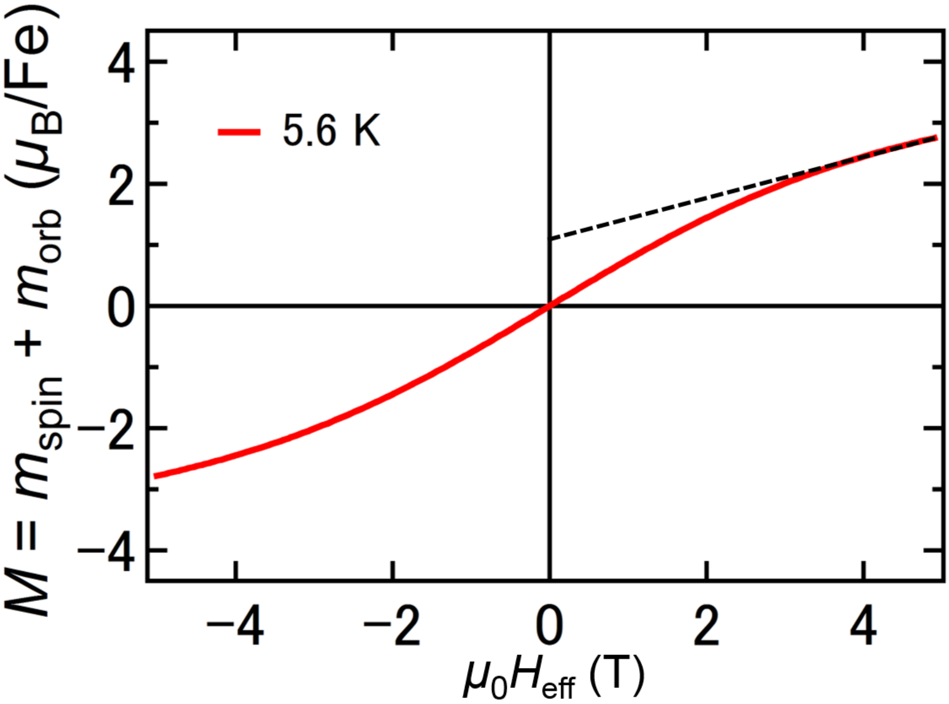

Figure 34. Effective magnetic-field dependence of the total magnetization M (= m_{spin}+m_{orb}) per one substitutional paramagnetic Fe at 5.6 K obtained using equation (7). [Y. K. Wakabayashi *et al.*, Scientific Reports **6**, 23295 (2016).]

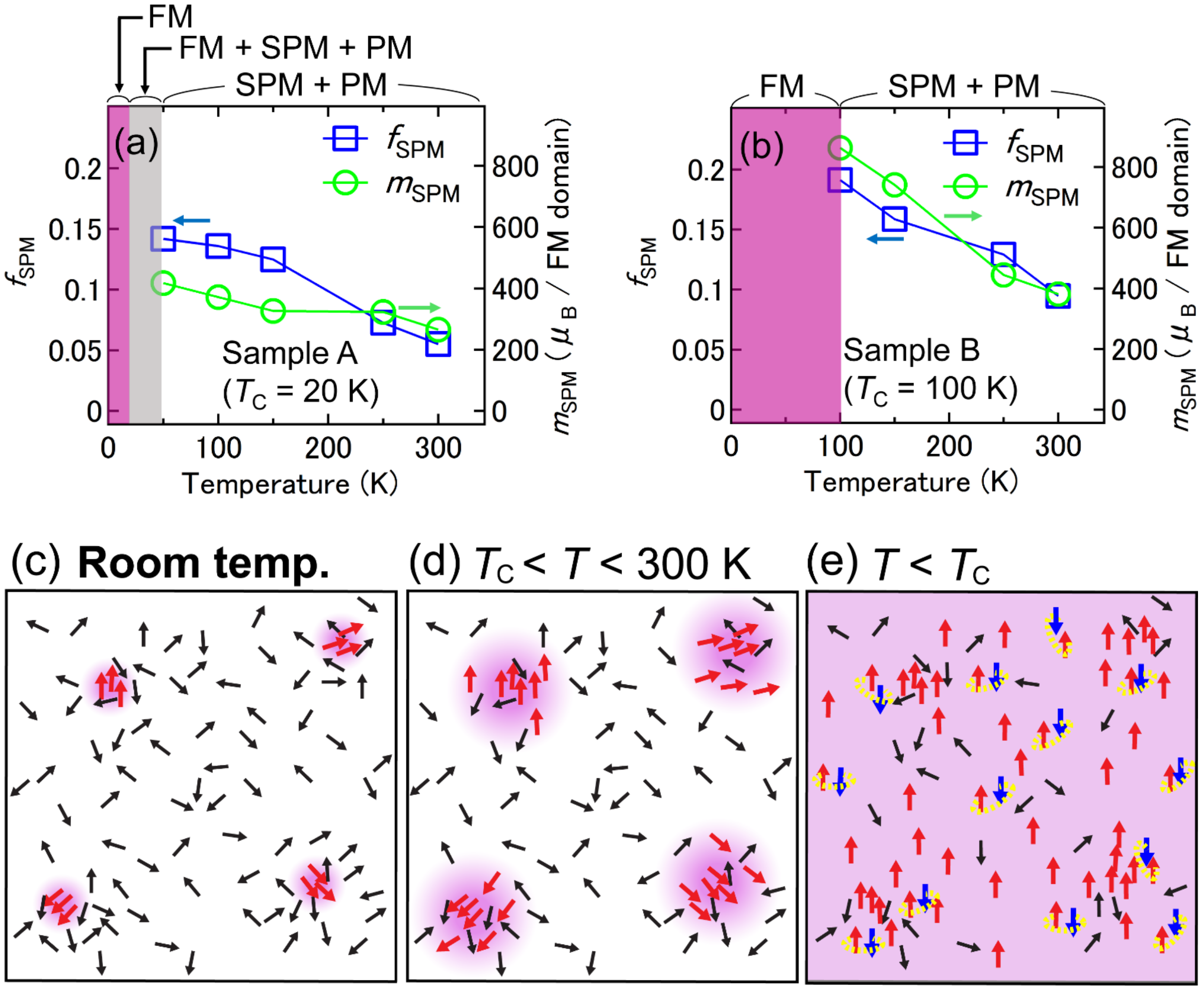

Figure 35. (a),(b) The temperature dependence of the best-fit parameters f_{SPM} and m_{SPM} obtained for (a) sample A and (b) sample B. The red, grey, and white areas indicate ferromagnetic (FM), FM + SPM + paramagnetic (PM), and SPM + PM regions, respectively. (c)–(e) Schematic diagrams showing the most likely picture of the magnetic states in the $\mathrm{Ge}_{0.935}\mathrm{Fe}_{0.065}$ films with zero magnetic field at (c) room temperature (i.e., $T = 300$ K), (d) $T_C < T < 300$ K, and (e) $T < T_C$. The small black, red and blue arrows correspond to the magnetic moments of the paramagnetic, ferromagnetic, and antiferromagnetically coupled substitutional Fe atoms, respectively. The red areas indicate ferromagnetic regions. Antiferromagnetically coupled Fe atoms are thought to exist all over the film at temperatures below T_C. [Y. K. Wakabayashi *et al.*, Scientific Reports **6**, 23295 (2016).]

We see a similar trend in the temperature dependence of the fitting parameters f_{SPM} and m_{SPM} in both films; i.e., f_{SPM} and m_{SPM} both increase with decreasing temperature [Figs. 35(a) and 35(b)]. This result implies that the ferromagnetic regions, which form only in the nanoscale high-Fe concentration regions at room temperature [Fig. 35(c)], expand toward lower Fe concentration regions with decreasing temperature [Fig. 35(d)], and finally the entire film becomes ferromagnetic at T_C [Fig. 35(e)]. This appears to be a characteristic feature of materials that exhibit single-phase ferromagnetism, despite the inhomogeneous distribution of magnetic atoms in the film. As shown in Fig. 35(a),(b), f_{SPM} and m_{SPM} are larger in sample B than in sample A, which can be attributed to the difference in spatial fluctuations of the Fe concentration, which are 4% – 7% in sample A and 3% – 10% in sample B. The larger the non-uniformity of the Fe distribution is, the larger each local ferromagnetic region, f_{SPM}, and m_{SPM} become, and the local ferromagnetic regions can be more easily connected magnetically, resulting in a higher T_{C}.

In summary of this section, we have investigated the local electronic structure and magnetic properties of the doped Fe atoms in the $\mathrm{Ge_{0.935}Fe_{0.065}}$ films, which have a diamond-type single-crystal structure without any ferromagnetic precipitates and with nanoscale spatial Fe concentration fluctuations, using XAS and XMCD.[98] The Fe atoms appear in the 2^+ state, with the 3*d* electrons strongly hybridized with the 4*p* electrons in Ge; this results in a delocalized 3*d* nature and long-range ferromagnetic ordering, leading to the excellent agreement between the *H* dependence of magnetization, MCD, and XMCD. Using the XMCD sum rules, we obtained the $M-H_{\mathrm{eff}}$ curves, which can be explained by the coexistence of SPM and paramagnetic properties at temperatures above T_{C}. The fitting results clearly show that the local ferromagnetic regions, which exist at room temperature, expand with decreasing temperature, leading to a ferromagnetic transition of the entire system at T_{C}. The non-uniformity of the Fe concentration seems to play a crucial role for the formation of the ferromagnetic regions, and our results indicate that strong ferromagnetism is inherent to GeFe, and persists at room temperature. Such a nanoscale expansion of the ferromagnetic regions is a key feature in understanding materials that exhibit single-phase ferromagnetism (i.e., where the film is free from any ferromagnetic precipitates) despite the *inhomogeneous* distribution of magnetic atoms in the film.

3. 4. ARPES measurements

There has been two models to explain the origin of the ferromagnetism in the FMSs; the valence band model[99,100] and the impurity-band model.[101,102] In the valence-band model, itinerant holes occupying states around the valence-band maximum (VBM) mediate ferromagnetism through Zener's *p*-*d* exchange interaction. In the impurity-band model, impurity levels are located within the band gap of the host semiconductor and ferromagnetism becomes stable through a double-exchange-like mechanism within the impurity band. The large difference of these two models is the position of the E_{F}. Therefore, it is important to investigate the the position of the E_{F} to examine which model is reasonable for GeFe.

In this section, using soft x-ray ARPES, we have clarified the origin of the ferromagnetism in GeFe by observing its electronic structure, namely, the position of the E_{F}

and the band dispersion.

We carried out the ARPES measurement on the sample consisting of a 120-nm-thick $Ge_{0.935}Fe_{0.065}$ layer grown on a Ge(001) substrate by LT-MBE. The $Ge_{0.935}Fe_{0.065}$ layer was grown at 240°C. The sample is the same as that studied in section 3.1 and 3.3. The T_C of the sample is 100 K. The soft x-ray ARPES experiment was performed at beam line BL23SU of SPring-8. The sample temperature was set to 20 K and x rays of 700-950 eV were used. The energy resolution was about 170 meV. The sample was placed so that the [-110] direction became parallel to the analyzer slit and perpendicular to the beam. By rotating the sample around the [-110] axis and changing the photon energy, we can change θ and ω in eqs. (7)-(10) (see section 2.2), and cover the entire Brillouin zone.

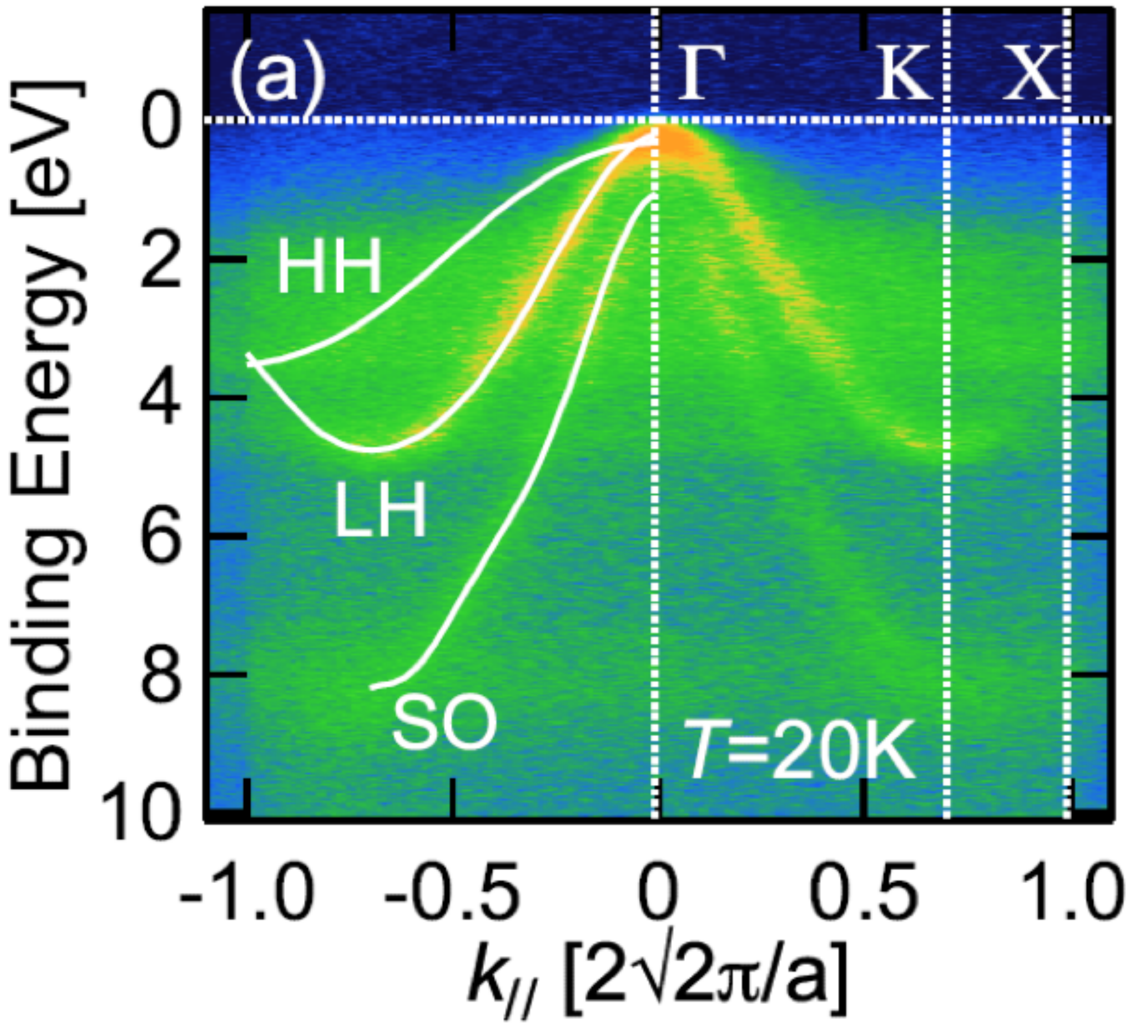

Figure 36. ARPES spectra along the Γ-K-X line in the Brillouin zone of the fcc lattice taken with the photon energy of 875 eV at 20 K. The peak positions of the second derivatives of the energy distribution curves (EDCs) are fitted to polynomial functions and shown by white solid curves. [S. Sakamoto, Y. K. Wakabayashi *et al.*, Physical Review B, in press.]

Figure 36 shows ARPES spectra along the Γ-K-X line in the Brillouin zone of the fcc lattice taken with the photon energy of 875 eV. The peak positions of the second derivatives of the energy distribution curves (EDCs) are fitted by polynomial functions, which are shown by white solid curves. Here, clear band-dispersion characteristics of Ge, such as the heavy-hole (HH) band, the light-hole (LH) band, and the split-off (SO) band, can be seen, indicating that the doped Fe atoms do not affect the electronic structure of the Ge host significantly. We note that this is also the case for (Ga,Mn)As. The energy of the VBM is located at 0.35 eV below E_F, indicating that the E_F of GeFe is located in the middle of the band gap of Ge (0.7 eV). This suggest that the impurity band model is applicable for GeFe.

A another characteristic feature of the impurity-band conduction picture is that the Fe 3*d* states have finite contribution to the density of states at the E_F. To examine the above feature, we carried out resonant photoemission spectroscopy (RPES), which allows us to detect the Fe specific electronic structure using the incident X-ray with the photon energy of the Fe 2*p*-3*d* absorption energy (714 eV).

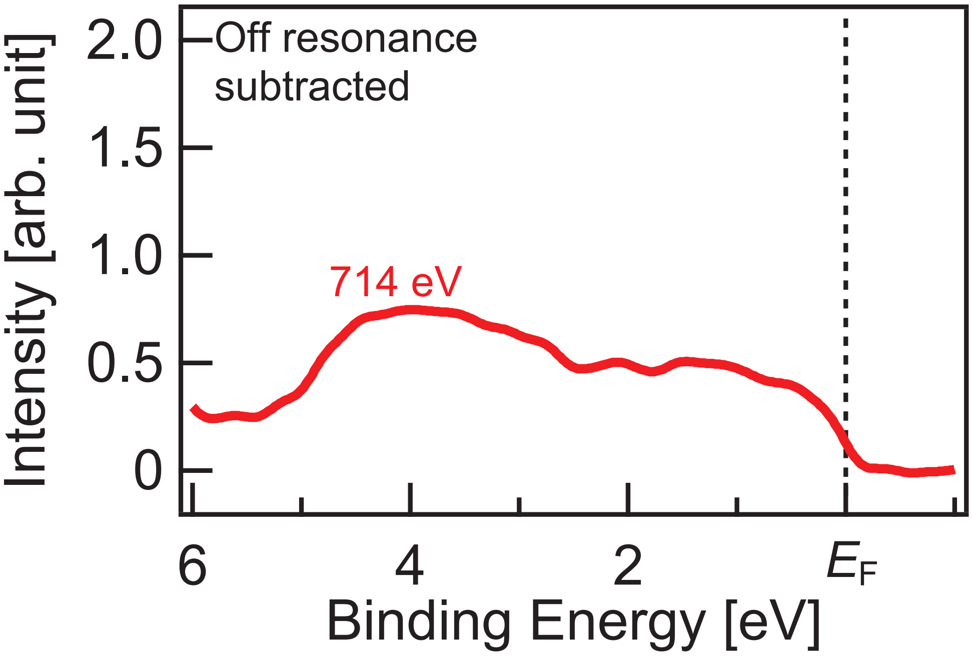

Fig. 37. Resonance photoemission spectrum of $Ge_{0.9335}Fe_{0.065}$. Spectrum was taken in the angle-integrated mode near the Fe L_3 absorption edge (714 eV). The off-resonance spectrum has been subtracted. [S. Sakamoto, Y. K. Wakabayashi *et al.*, Physical Review B, in press.]

Figure 37 shows RPES spectra taken in the angle-integrated mode near the Fe L_3 absorption edge (714 eV). Here, the off-resonance spectrum taken at a lower photon energy of 704 eV has been subtracted and the binding energy is defined relative to E_F. Due to the strong Auger peak, it was difficult to extract the PDOS from the spectra taken with the photon energy of the absorption peak at 708 eV. Therefore, using higher energy photons of 714 eV, we have deduced the Fe 3*d* partial density of states (PDOS) as shown in Fig. 37. The Fermi edge-like step can be seen at E_F, indicating that the Fe 3*d* states have a finite contribution to the states at E_F. We note that the Fermi edge-like feature at E_F is much clearer in GeFe than in (Ga,Mn)As, indicating that contributions of 3*d* electrons to the states at E_F are more pronounced in GeFe than in (Ga,Mn)As. This difference of the contributions of 3*d* electrons to the states at E_F between GeFe and (Ga,Mn)As should be the origin of the difference of the transport mechanism below T_C; hopping transport in GeFe and metallic transport in (Ga,Mn)As.

In summary of this section, we performed soft X-ray ARPES measurements for GeFe. ARPES and RPES spectra show that the E_F is located at 0.35 eV above the VBM and that the Fe 3*d* states exist at the E_F, indicating that the impurity band model seems to be applicable for GeFe and the ferromagnetic interaction is mediated by double-exchange interaction mediated by the Fe 3*d* impurity levels.[103]

Chapter 4: Fe/MgO/$Ge_{0.935}Fe_{0.065}$ Magnetic Tunnel Junctions

4. 1. Growth of Fe/MgO/$Ge_{1-x}Fe_x$ magnetic tunnel junctions

For the realization of Si- and Ge-based spintronic devices using GeFe, it is necessary to confirm the presence of the spin polarized carriers at the E_F in GeFe. Recently, first principles calculations suggested that the E_F is located in two overlapping highly spin-polarized bands formed in the bandgap of GeFe; spin-down $d(e)$ band and spin-up p-$d(t_2)$ band.[103] Thus, it is important to clarify how these bands contribute to spin injection and detection. Thus far, there has been no report of successful detection of spin-dependent tunneling in MTJs using group-IV FMSs. In this chapter, we show TMR[28,104-106] in epitaxially grown MTJs composed of Fe/MgO/$Ge_{0.935}Fe_{0.065}$. This is the first observation of TMR in MTJs with a group-IV FMS. We found that spin-polarized carriers in the p-$d(t_2)$ band of GeFe are mainly responsible for the tunneling transport.

We fabricated MTJs composed of Fe (14 nm) / MgO (d nm) / $Ge_{0.935}Fe_{0.065}$ (50 nm) / Ge:B (B: 4×10^{19} cm^{-3}, 70 nm) grown on a p^+-Ge (001) substrate by LT-MBE [Fig. 38(a)]. The growth process is described as follows. After the Ge substrate was chemically cleaned by ultra pure water, ammonia water, and acetone, followed by cleaning and etching with ultra pure water and buffered HF in a cyclical manner for 1 hour, it was introduced in the ultrahigh vacuum MBE growth chamber through an oil-free load-lock system. After degassing the substrate at 300°C for 30 minutes and successive thermal cleaning at 740°C for 15 minutes, we grew the Ge:B buffer layer at 300°C, which was followed by the growth of the 50-nm-thick $Ge_{0.935}Fe_{0.065}$ layer at 240°C. The MgO barrier layer was grown by electron beam deposition in our MBE growth chamber at 80°C with a growth rate of 0.02 Å/s. The thickness d of the MgO barrier was changed from 3 nm to 9 nm in the same wafer by moving the main shutter in front of the sample surface during the deposition of MgO. Then, we grew the top Fe layer at 50°C. To obtain a flat surface of the top Fe layer, the sample was annealed at 250°C for 30 minutes after the growth. We used *in situ* RHEED to monitor the crystallinity and surface morphology during the growth [Figs. 38(c)-38(j)]. The diffraction patterns indicate that the MgO and Fe layers are epitaxially grown on $Ge_{0.935}Fe_{0.065}$ with the epitaxial relationship of Fe[100](001)// MgO[110](001)// $Ge_{0.935}Fe_{0.065}$[100](001) shown in Fig. 38(b), which is the same as that of Fe/MgO/Ge.[107,108] The diffraction patterns of the top Fe layer change from spotty [Figs. 38(e) and 38(f)] to streaky [Figs. 38(c) and 38(d)] by the annealing, reflecting the improvement of the surface flatness. The root mean square of the surface roughness of the top Fe layer measured by atomic force microscopy (AFM) was about 0.24

nm, which means that an atomically flat surface was obtained (see Fig. 39). The T_C value of the $Ge_{0.935}Fe_{0.065}$ layer was 100 K. Figure 40(a),(b) shows the cross-sectional HRTEM images of the sample. One can see that almost the entire region of the trilayer has an epitaxially-grown single-crystal structure with smooth and flat interfaces. There are some amorphous-like crystal domains, which are indicated by the yellow arrows in Figs. 40(a) and 40(b), between the regions that have slightly different tilts of the crystal orientation indicated by the white dashed lines in Fig. 40(b).

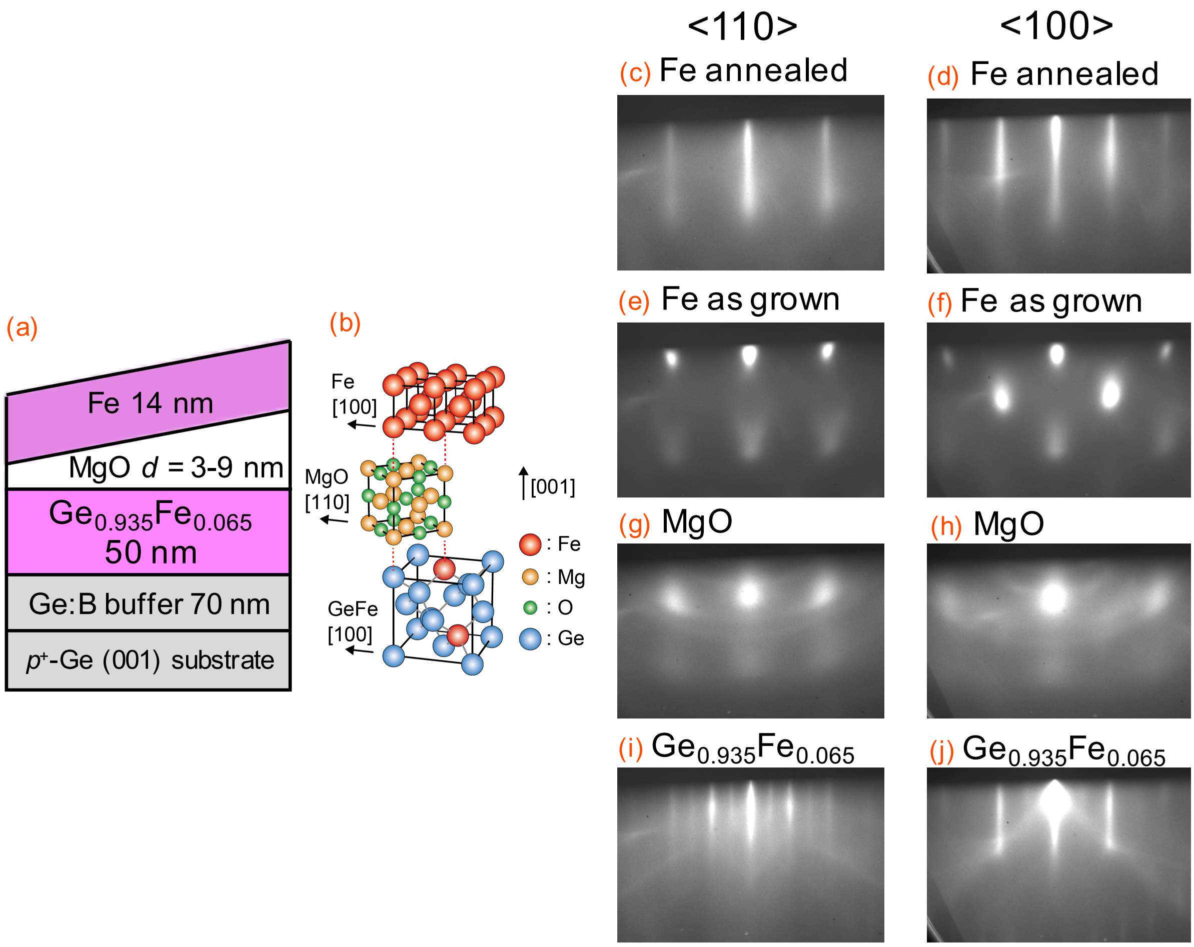

Fig. 38. (a),(b) Schematic illustrations of (a) the Fe/MgO/GeFe trilayer sample fabricated in our study and (b) its epitaxial relationship. In (b), the black and gray lines represent the unit cells and covalent bonds, respectively. (c)-(j) RHEED patterns of (c),(d) the annealed Fe layer, (e),(f) as-grown Fe layer, (g),(h) MgO layer, and (i),(j) $Ge_{0.935}Fe_{0.065}$ layer with the electron-beam azimuth along (c),(e),(g),(i) the <110> direction and (d),(f),(h),(j) the <100> direction of the Ge(001) substrate. [Y. K. Wakabayashi *et al.*, Applied Physics Express **9**, 123001 (2016).]

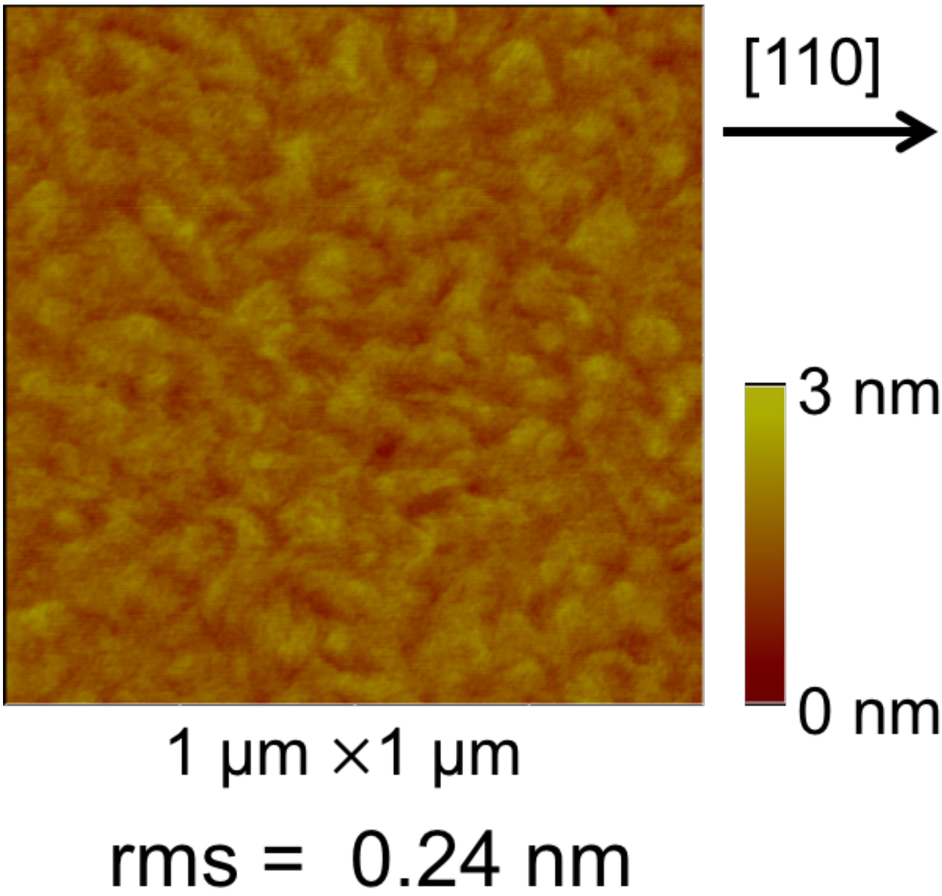

Fig. 39. AFM image of the Fe/MgO/GeFe sample.

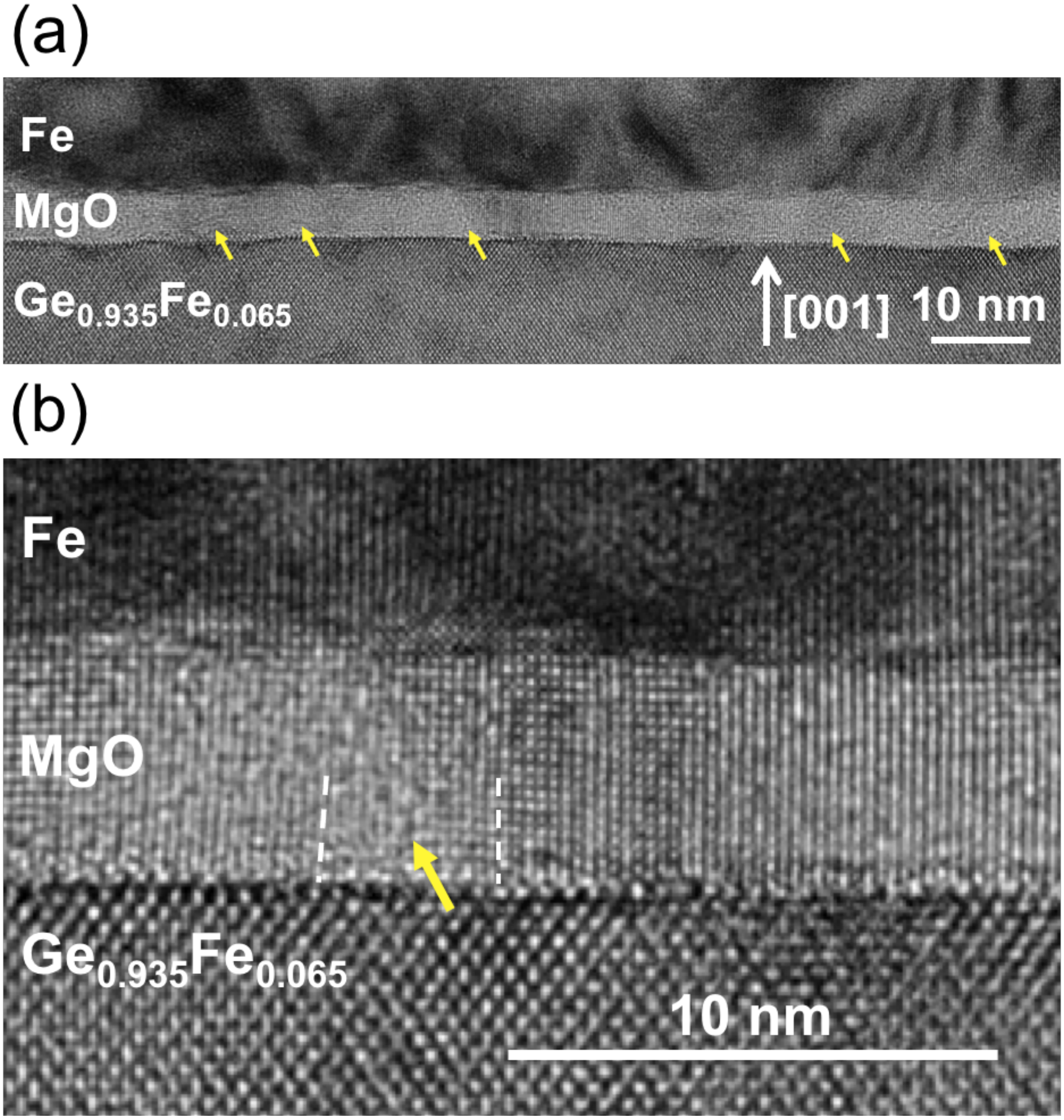

Fig. 40. (a) HRTEM lattice image of the Fe/MgO/GeFe sample projected along the Ge<110> axis. (b) Magnified image of (a). In the MgO layer, there are some amorphous-like crystal domains indicated by the yellow arrows between the regions that have slightly different tilts of the crystal orientation indicated by the white dashed lines. [Y. K. Wakabayashi *et al*., Applied Physics Express **9**, 123001 (2016).]

4. 2. TMR in Fe/MgO/Ge$_{1-x}$Fe$_x$ magnetic tunnel junctions

For tunneling transport measurements, square mesas with a size of 700 × 700 μm were fabricated on the sample using photolithography and Ar-ion etching. As shown in Fig. 41(a), the resistance-area product RA is symmetric about V=0 for all the MTJs with d from 3 to 9 nm at 3.5 K, where V is the bias voltage applied to the top electrode with respect to the substrate. This suggests that the Schottky barrier is not formed at the MgO/GeFe interface. This result can be understood by considering the E_F position; it was reported that E_F is pinned at about 0.12 eV above the VBM at the MgO/*p*-Ge interface,[109] and ARPES measurements for GeFe showed that E_F is located at 0.35 eV above the VBM in impurity bands (Fig. 36), which are indicated by the pink area in the inset of Fig. 41(a).[103] The *RA* increases exponentially as *d* increases [Fig. 41(b)]. This is a typical feature of tunnel junctions. In the Wentzel-Kramer-Brillouin (WKB) approximation, the slope of the ln *RA* – *d* characteristics is given by $2\sqrt{2m^*V_b}/\hbar$. From our results, m^*V_b [kg·eV] is estimated to be $0.035m_0$ for Fe/MgO/GeFe. Here, m_0 is the free-electron mass, m^* is the effective mass of holes, and V_b is the barrier height. This value is significantly lower than the reported values for the MgO barrier in the literature ($1.1m_0$ and $3.6m_0$ for the epitaxial MgO(001) barrier in Fe/MgO/Fe and FeCo/MgO/Fe structures, respectively).[110,111] In Fe/MgO/Fe MTJs, it is known that the barrier height is decreased by oxygen-vacancy defects in the MgO barrier.[28] The low barrier height of our junctions is probably due to the presence of the amorphous-like crystal domains in the MgO layer, which are seen in the HRTEM lattice images [see Figs. 40(a) and 40(b)], in addition to the oxygen-vacancy defects. These domains may have a role of leak paths and decrease the tunnel resistance, lowering the barrier height.

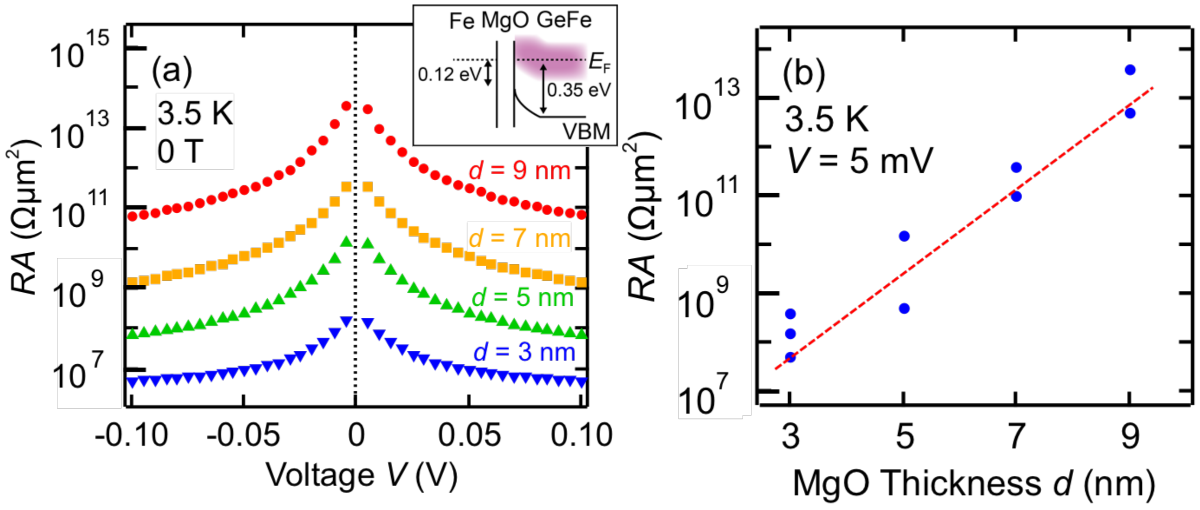

Fig. 41. (a) *RA* versus the bias voltage *V* measured at 3.5 K for the Fe/MgO/GeFe MTJs with the MgO thickness *d* ranging from 3 to 9 nm. Inset of (a) shows the band line-up of Fe/MgO/$Ge_{0.935}Fe_{0.065}$. The solid and dotted lines correspond to the VBM and the Fermi level E_F. The pink area represents the impurity bands. (b) *RA* as a function of *d* measured with *V* = 5 mV at 3.5 K. [Y. K. Wakabayashi *et al.*, Applied Physics Express **9**, 123001 (2016).]

Figure 42(a) shows the magnetic-field dependence of *RA* measured with *V* = 40 mV at 3.5 K when *d* is 3 nm. The magnetic field *H* was applied along the [110] axis in the plane of the Ge substrate. We note that the *RA* - *H* data showed no noticeable dependence on the in-plane direction of *H*, reflecting the weak magnetic anisotropy of GeFe. The red and blue curves (major loop curves) were obtained by sweeping *H* from positive to negative and negative to positive, respectively. The jumps of *RA* at $\mu_0 H$ = ~±2 mT in the major loop correspond to the magnetization reversal of the top Fe layer.[28] The *RA* values measured with the opposite magnetic-field sweep directions gradually become closer with increasing $|\mu_0 H|$, reflecting the gradual saturation of the magnetization in the $Ge_{0.935}Fe_{0.065}$ layer. As can be seen in the minor loop [green curve in the inset of Fig. 42(a)], the anti-parallel magnetization configuration is stable at $\mu_0 H$ = 0 T. This is a typical feature of TMR. We note that the measurements of *RA* - *H* performed on a reference Al/$Ge_{0.935}Fe_{0.065}$/Ge:B sample, which does not have an MgO barrier layer, did not show clear magnetoresistance, indicating that the observed magnetoresistance in Fe/MgO/GeFe originates from the tunneling transport through the MgO barrier.

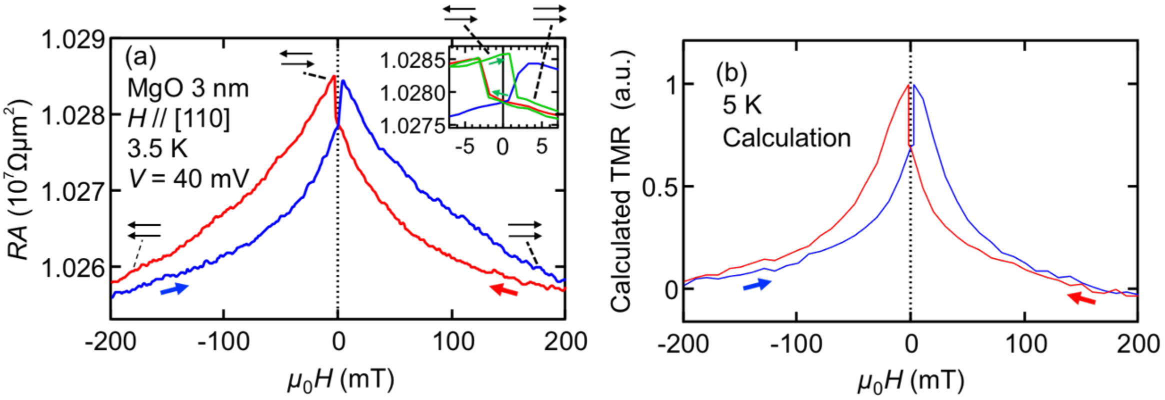

Fig. 42. (a) Magnetic-field ($\mu_0 H$) dependence of *RA* of the MTJ with d = 3 nm measured with a bias voltage V of 40 mV at 3.5 K. The magnetic field *H* was applied along the [110] axis in the plane of the Ge substrate. The red and blue curves (major loop curves) were obtained by sweeping *H* from positive to negative and negative to positive, respectively. The black arrows indicate the magnetization configurations of the top Fe layer and the bottom $Ge_{0.935}Fe_{0.065}$ layer. The inset shows the magnified plot of the TMR curves. The green curve is the minor loop. (b) Calculated TMR curves at 5 K as a function of $\mu_0 H$ obtained by multiplying the [110] direction component of the magnetizations between the top Fe and the bottom $Ge_{0.935}Fe_{0.065}$ layers. [Y. K. Wakabayashi *et al.*, Applied Physics Express **9**, 123001 (2016).]

We can calculate the TMR curves using the magnetization curves of Fe and GeFe. From Julliere's model, the TMR ratio defined as [*RA*($\mu_0 H$) - *RA*(200 mT)]/*RA*(200 mT) is given by

$$\text{TMR ratio} = \frac{P_{\mathrm{Fe}} P_{\mathrm{GeFe}}[1\text{-}\cos(\theta_{\mathrm{Fe}} - \theta_{\mathrm{GeFe}})]}{1 + P_{\mathrm{Fe}} P_{\mathrm{GeFe}} \cos(\theta_{\mathrm{Fe}} - \theta_{\mathrm{GeFe}})}. \tag{27}$$

Here, *RA*($\mu_0 H$) represents the *RA* value obtained under $\mu_0 H$ (mT). P_{Fe} (P_{GeFe},) and θ_{Fe} (θ_{GeFe}) are the spin polarization P and the direction of the magnetization relative to the [110] axis (//H) in the Fe (GeFe) layer, respectively. When $P_{\mathrm{Fe}}P_{\mathrm{GeFe}} \ll 1$, the denominator in Eq. (27) becomes 1. Because the magnetization of the Fe layer is sharply reversed (*i.e.*, $\theta_{\mathrm{Fe}} = 0°$ or 180°), $\cos(\theta_{\mathrm{Fe}} - \theta_{\mathrm{GeFe}})$ is expressed by $M^{\mathrm{Fe}}M^{\mathrm{GeFe}}/M_{\mathrm{s}}^{\mathrm{Fe}}M_{\mathrm{s}}^{\mathrm{GeFe}}$,[112] where M^{Fe} (M^{GeFe}) is the H direction component of the magnetization of Fe (GeFe) and $M_{\mathrm{s}}^{\mathrm{Fe}}$ ($M_{\mathrm{s}}^{\mathrm{GeFe}}$) is the saturation magnetization of Fe (GeFe). Thus, the TMR ratio of our MTJs should be approximately proportional to $1 - M^{\mathrm{Fe}}M^{\mathrm{GeFe}}/M_{\mathrm{s}}^{\mathrm{Fe}}M_{\mathrm{s}}^{\mathrm{GeFe}}$. Figure 42(b) shows the calculated TMR ratio obtained by $M^{\mathrm{Fe}}M^{\mathrm{GeFe}}$. Here, the magnetization curve of the $\mathrm{Ge}_{0.935}\mathrm{Fe}_{0.065}$ layer was estimated by MCD at 5 K with a photon energy of 2.3 eV corresponding to the L-point energy gap of bulk Ge measured for a $\mathrm{Ge}_{0.935}\mathrm{Fe}_{0.065}$ film, which was grown with the same condition as that for our MTJ sample. We assumed that the magnetization curve of the top Fe has a rectangular shape with the coercive fields of ±2 mT. We can see that the calculated TMR curves qualitatively reproduce the experimental TMR curves [Fig. 42(b)]. The slight difference between the experimental TMR curves and the calculated TMR curves may originate from the presence of small tunneling anisotropic magnetoresistance of GeFe, or from the difference between the magnetization near the MgO/GeFe interface and that of the entire GeFe film.

Figure 43(a) shows the TMR ratio as a function of $\mu_0 H$ at various temperatures measured with $V = 40$ mV when $d = 3$ nm. The TMR ratio (at $\mu_0 H = 2$ mT) decreases [Fig. 43(b)] and the hysteresis becomes smaller [Fig.43(a)] with increasing temperature, reflecting a decrease in the magnetization of the $\mathrm{Ge}_{0.935}\mathrm{Fe}_{0.065}$ layer. These results also support our conclusion that the measured magnetoresistance is due to the TMR effect.

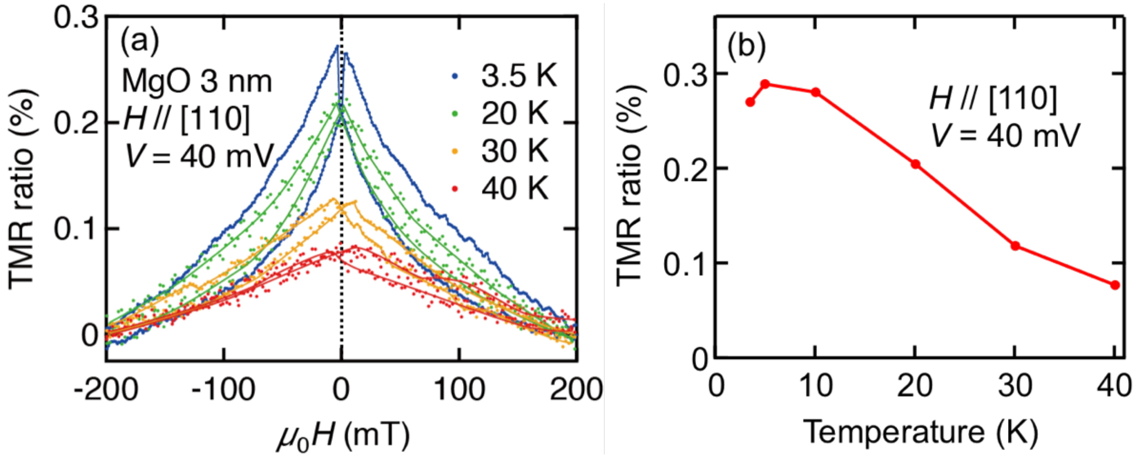

Fig. 43. (a) TMR ratio, which is defined as [$RA(\mu_0 H)$ - RA(200 mT)]/RA(200 mT), as a function of $\mu_0 H$ at various temperatures. (b) TMR ratio at $\mu_0 H = 2$ mT as a function of temperature when d is 3 nm and the bias voltage V is 40 mV. [Y. K. Wakabayashi *et al.*, Applied Physics Express **9**, 123001 (2016).]

First-principles supercell calculations performed on GeFe suggested that the Fermi level is located in two overlapping impurity bands that have opposite spin directions formed in the band gap; one is a narrow spin-down $d(e)$ band, in which P is almost 100%, and the other is a spin-up p-$d(t_2)$ band, in which P is about 70%.[103] In the recent ARPES measurements for $Ge_{0.935}Fe_{0.065}$, it was confirmed that the Fe 3d impurity states actually have finite contribution to the density of states at E_F (see section 3.3). Because the observed sign of the TMR ratio was positive in Fe/MgO/GeFe and P of Fe is positive, our result means that the spin-up p-$d(t_2)$ band is responsible for the tunneling properties.[103] From the TMR ratio about 0.27% observed at 3.5 K [Fig. 43(a)], the P value of the $Ge_{0.935}Fe_{0.065}$ layer is estimated to be 0.17% by Julliere's model,[113] when we use the effective P value of the top Fe layer estimated from TMR observed for Fe/MgO/Fe (P = 75%).[28] This P value obtained for GeFe is much smaller than that predicted by the first-principles supercell calculations (70%).[103] This is probably due to the leak current, which does not contribute to TMR, through the amorphous crystal domains. Thus, the TMR ratio is expected to be enhanced in the Fe/MgO/GeFe MTJs by improving the crystallinity of the MgO tunnel barrier and decreasing the leak current through the amorphous crystal domains in MgO.

In summary of this chapter, we have grown MTJs composed of epitaxial Fe/MgO/$Ge_{0.935}Fe_{0.065}$ and demonstrated the first successful observation of TMR in the MTJs containing a group-IV ferromagnetic semiconductor.[114] This result confirms the presence of spin-polarized carriers at E_F in GeFe. The observed sign of the TMR was positive, which revealed that the largely spin-polarized carriers in the p-$d(t_2)$ band are dominant for the tunneling. The TMR ratio will be increased in the Fe/MgO/GeFe MTJs by improving the crystallinity of the MgO tunnel barrier and decreasing the leak current through the amorphous crystal domains in MgO. Our results show that GeFe is promising for spin injectors and detectors of future Si- and Ge-based spintronic devices.

Chapter 5: Crystal Structure, Magnetic Properties, and Spin-Dependent Transport of the $Ge_{1-x}Mn_x$ Granular Films

5. 1. Approach to clarify the origin of the spin-dependent transport in GeMn granular films

$Ge_{1-x}Mn_x$ granular thin films have attracted much interest for spintronic applications owing to their large positive MR, which can be as high as ~280% (under 5 T at 40 K), and to their compatibility with existing semiconductor technology.[13-21] In GeMn, the sharp enhancement of the MR at very low temperatures and its peculiar spike-shaped magnetic field dependence cannot be explained by GMR[115] or magnetic field-dependent avalanche breakdown,[116,117] which is widely invoked to explain the origin of the MR of granular films. Previous studies of GeMn have suggested that the large MR is related to nanoscale spinodal decomposition of GeMn into FM metallic Mn-rich nanoparticles and a PM Mn-poor matrix [Fig. 45].[14,15,19,20] However, the microscopic origin of the MR has not yet been clarified over the past decade since the first report of GeMn, although understanding the microscopic origin of the MR is vitally important for the development of spin-dependent functionality in granular films. Generally, the origin of the MR in granular systems is discussed in the context of the *macroscopic* properties of the transport and magnetization of the films. For more profound understanding of the MR, however, it is obvious that we need *microscopic* information. Because the large MR of GeMn is thought to be induced by spin-dependent scattering near the interfaces between the nanoparticles and the matrix, separate detection of the magnetic properties of the FM nanoparticles and the PM matrix near the interfaces is necessary. However, this is difficult with conventional magnetization measurements using SQUID.

The XMCD measurements are extremely sensitive to the local magnetic state of each atom in magnetic films.[79-83] One can distinguish between the different local magnetic states based on the difference in the energy spectrum in addition to the difference in the magnetic-field dependence of the XMCD signal from each atom. Thus, by carefully analyzing the magnetic-field dependence of the XMCD signals using various incident-photon energies, it would be possible to distinguish the magnetic signals originating from the FM nanoparticles from those originating from the PM matrix. Another advantage of XMCD, especially in our study, is its probing depth. In the TEY mode used for the present XMCD measurements, we detect signals originating from atoms located within 2–3 nm of the film surface.[118] As shown in Fig. 45, the nanoparticles are located approximately 3–5 nm from the film surface of GeMn. Thus, one can selectively study the magnetic properties near the top interfaces of those nanoparticles. Because the scattering of charge carriers occurs near those interfaces, XMCD measurements are suitable for the investigation of first order magnetic scattering in GeMn. In addition, because XMCD is free from the diamagnetic signal from the substrate, one can perform very accurate measurements. Despite these attractive features, there have been no reports of selective detection of the magnetizations of the nanoparticles and matrix in magnetic granular films using XMCD.

In this chapter, we demonstrate a unique method to separately investigate the magnetic properties of the nanoparticles and the matrix in GeMn granular thin films and clarify the origin of the large MR, its peculiar magnetic field dependence, and its large enhancement at low temperatures. We make full use of the aforementioned advantages of XMCD and carefully analyze the XMCD data. We find that the MR ratio is proportional to the product of the magnetizations originating from the FM nanoparticles and the PM matrix. This indicates that the spin-polarized holes, which penetrate from the nanoparticles into the matrix, undergo first order magnetic scattering by the PM Mn atoms in the matrix, thereby causing the large MR.

5. 2. Crystal structure and magnetic properties

The investigated $Ge_{1-x}Mn_x$ thin films have total Mn concentrations x of 0.09 and 0.14. They were grown on Ge(111) substrates by LT-MBE. Figure 44(a),(b) shows the schematic cross-sectional structures of (a) the samples used for the measurements of the XMCD, SQUID, and HRTEM, and (b) those used for the magneto-transport measurements, respectively. The growth process is described as follows. After the *p* (or *n*)-type Ge(111) substrates were chemically cleaned by ultra-pure water and acetone, followed by etching with ultra-pure water and buffered HF in a cyclical manner for 1 hour, they were introduced in our ultrahigh vacuum ($\leq \sim 7.0\times10^{-9}$ Pa) MBE growth chamber through an oil-free load-lock system. After degassing the substrate at 400°C for 30 minutes and successive thermal cleaning at 740°C for 15 minutes, we grew a 10-nm-thick Ge buffer layer at 180°C, which was followed by the growth of a 13-nm-thick $Ge_{1-x}Mn_x$ layer at 130°C. After that, in the case of the samples used for the XMCD, SQUID, and HRTEM measurements, we grew a 1.5-nm-thick Ge capping layer at 130°C to avoid the surface oxidation of the GeMn layer. During the growth, the *in situ* RHEED of the $Ge_{0.91}Mn_{0.09}$ and $Ge_{0.86}Mn_{0.14}$ layers showed 2×2 and 1×1 streaks, respectively. This result indicates that the $Ge_{1-x}Mn_x$ layers are epitaxially grown on the Ge substrates. To avoid parallel conduction through the substrate, the samples for the magneto-transport measurements were grown on *n*-type substrates. This is because GeMn is *p*-type, and the *p*-*n* junction of *p*-GeMn/ *n*-Ge prevents carrier diffusion from the GeMn layer to the substrate.[119] For other samples, after the growth of the $Ge_{1-x}Mn_x$ layer, we grew a 1.5-nm-thick Ge capping layer to prevent surface oxidation of the $Ge_{1-x}Mn_x$ layer.

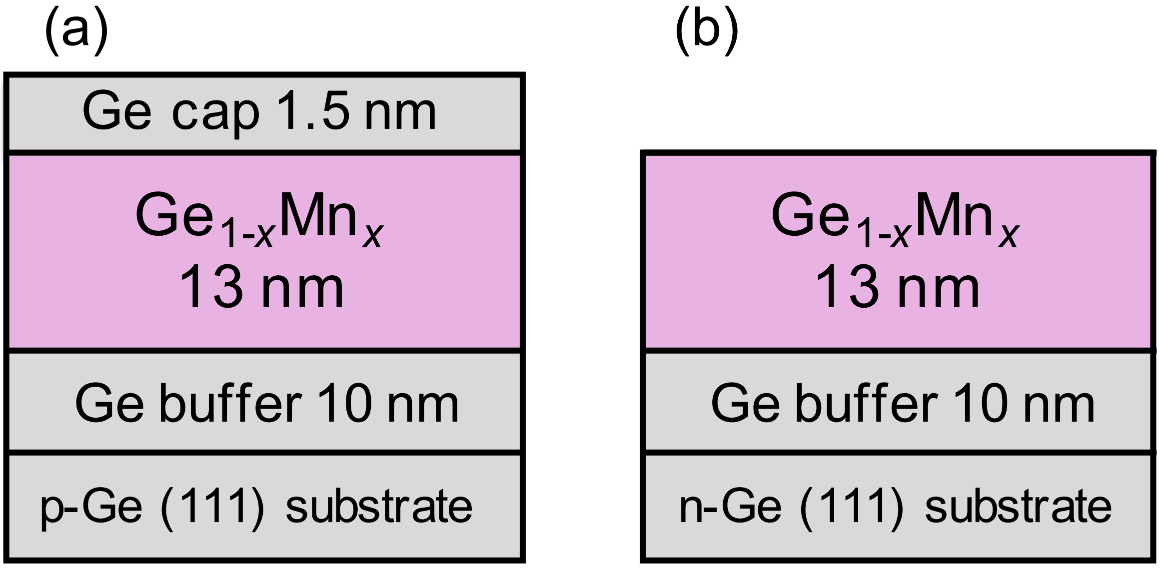

Fig. 44. (a),(b) Schematic cross-sectional structures of the samples used (a) for the XMCD, SQUID and HRTEM measurements, and (b) for the magneto-transport measurements. [Y. K. Wakabayashi *et al.*, Physical Review B **95**, 014417 (2017).]

The crystallographic analyses on the $Ge_{0.86}Mn_{0.14}$ film were performed by HRTEM combined with the spatially resolved TED and EDX. In the EDX measurements, the spot diameter of the incident electron beam was set at ~0.2 nm. From the HRTEM lattice image of the $Ge_{0.86}Mn_{0.14}$ (Fig. 45), it is found that the $Ge_{0.86}Mn_{0.14}$ layer basically has a diamond-type crystal structure. There are sphere-like nanoparticles embedded in the matrix (see the dashed circles in Fig. 45). The nanoparticles are located 3–5 nm from the film surface. By the spatially resolved EDX measurements, the local Mn concentrations at *1 (matrix) and *2 (nanoparticle) are roughly estimated to be ~6% and ~60%, respectively. Because we obtained similar XMCD results both for the $Ge_{0.91}Mn_{0.09}$ and $Ge_{0.86}Mn_{0.14}$ samples as shown later (Fig. 56), we can estimate that the ratio of the local Mn concentration of the Mn-rich nano-particles to that of the Mn-poor-matrix is roughly similar between the two samples. Then, the local Mn concentrations in the nanoparticles and the matrix in the $Ge_{0.91}Mn_{0.09}$ film are estimated to be ~40% and ~4%, respectively. Figures 46(a) and 46(b) show the TED images at *1 and *2, respectively. The main diffraction patterns at both points indicate the diamond-type crystal structure. Additionally, a weak halo pattern is seen at *2, indicating the presence of amorphous structures. Such a weak halo pattern is also seen in the plane-view TED patterns as shown in Ref. 20. The XRD diffraction patterns of our $Ge_{0.86}Mn_{0.14}$ film indicate the presence of Mn_5Ge_3 precipitates,[20] which are the most stable compound in the Mn-Ge phase diagram.[15,120] These results indicate that the Mn-rich nanoparticles have a heavily-Mn doped amorphous GeMn phase including Mn_5Ge_3 precipitates, and that the surrounding Mn-poor matrix has a diamond-type crystal structure. Most of the 1.5-nm-thick Ge capping layer is naturally oxidized in the atmosphere. To remove this layer, the samples were briefly etched in dilute HF solution prior to loading them into the XMCD vacuum chamber. Before performing the measurements, we carefully checked and confirmed the *absence* of a two-peak structure at 537 and 540 eV in the XAS spectrum, which originates from the Mn oxide on the sample surface.[121]

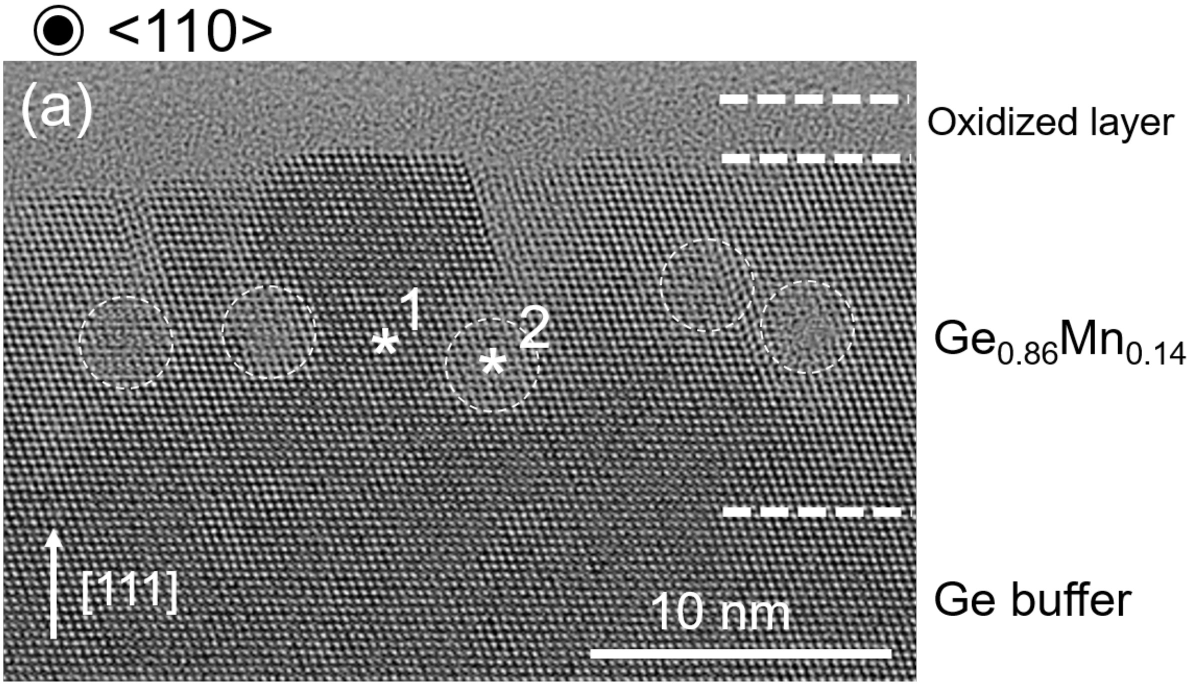

Fig. 45. Transmission electron microscope lattice image of the $Ge_{0.86}Mn_{0.14}$ layer projected along the Ge<110> axis. The nanoparticles are indicated by white dashed circles. By the spatially resolved energy dispersive X-ray spectroscopy, the local Mn concentrations at *1 (matrix) and *2 (nanoparticle) are estimated to be ~6% and ~60%, respectively. [Y. K. Wakabayashi *et al.*, Physical Review B **95**, 014417 (2017).]

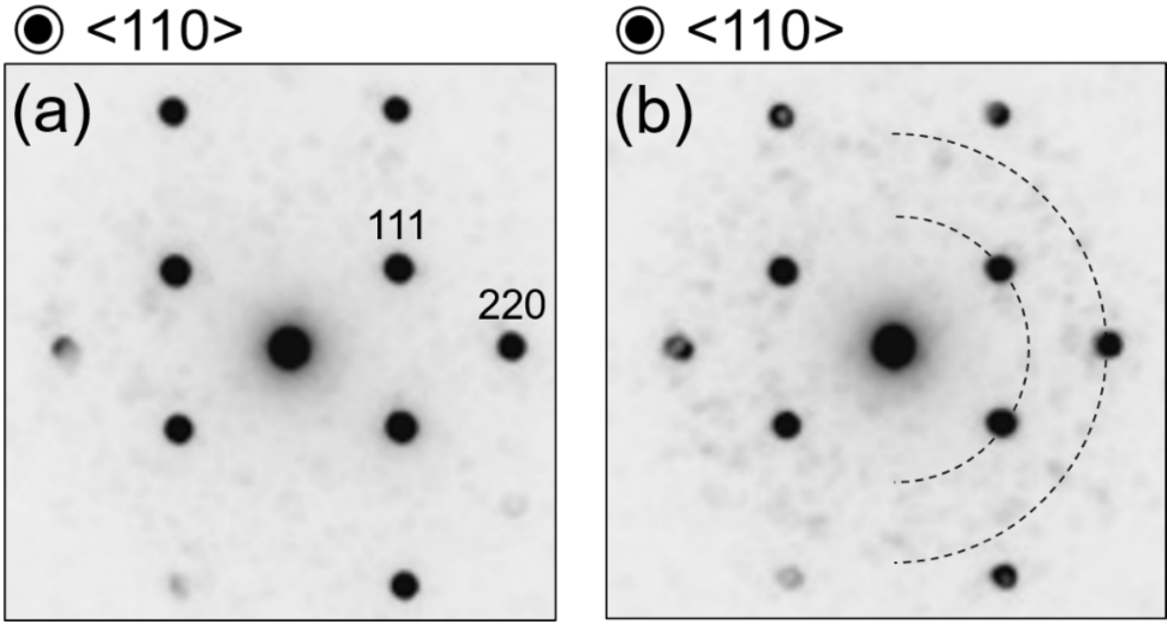

Fig. 46. (a),(b) TED images at (a) *1 (matrix) and (b) *2 (nanoparticle) projected along the Ge<110> axis. The weak halo pattern is indicated by the dashed curves in (b). [Y. K. Wakabayashi *et al.*, Physical Review B **95**, 014417 (2017).]

5. 3. XMCD measurements

For the XAS and XMCD measurements, we used the twin-helical undulator beamline BL23SU of SPring-8, which enabled us to perform efficient measurements of XMCD with various incident photon energies and magnetic fields at various temperatures.[87] Figure 47(a),(b) shows (a) the Mn $L_{2,3}$-edge XAS $[(\mu^{+} + \mu^{-})/2]$ spectrum and (b) the XMCD ($= \mu^{+} - \mu^{-}$) spectra for the $\mathrm{Ge_{0.86}Mn_{0.14}}$ film at 6 K with various magnetic fields applied perpendicular to the film surface. The direction of the incident X-ray is also perpendicular to the film surface. Here, μ^{+} and μ^{-} refer to the absorption coefficients for the photon helicity parallel and antiparallel to the Mn 3*d* majority spin direction, respectively. In both the XAS and XMCD spectra, one can see five peaks at the Mn L_3-edge (whose energies are referred to as *a*-*e*) [see also the insets in Figs. 47(a) and 47(b)] and two peaks at the Mn L_2-edge (whose energies are referred to as *f* and *g*). When the XMCD spectra are normalized at *c*, the spectral line shape is changed with varying *H*, and the peak at *c* becomes more dominant as *H* increases, as shown in the inset of Fig. 47(b). Whereas the XMCD intensities at *a* and *b* tend to saturate for $\mu_0 H = 7$ T, the one at *c* does not. This indicates that the peaks at *a* and *b* have a certain amount of an FM component, whereas the peak at *c* mainly originates from the PM Mn atoms. The same features were also observed in the $\mathrm{Ge_{0.91}Mn_{0.09}}$ film (see Fig. 48). These results indicate that the XMCD signals have both PM and FM components.

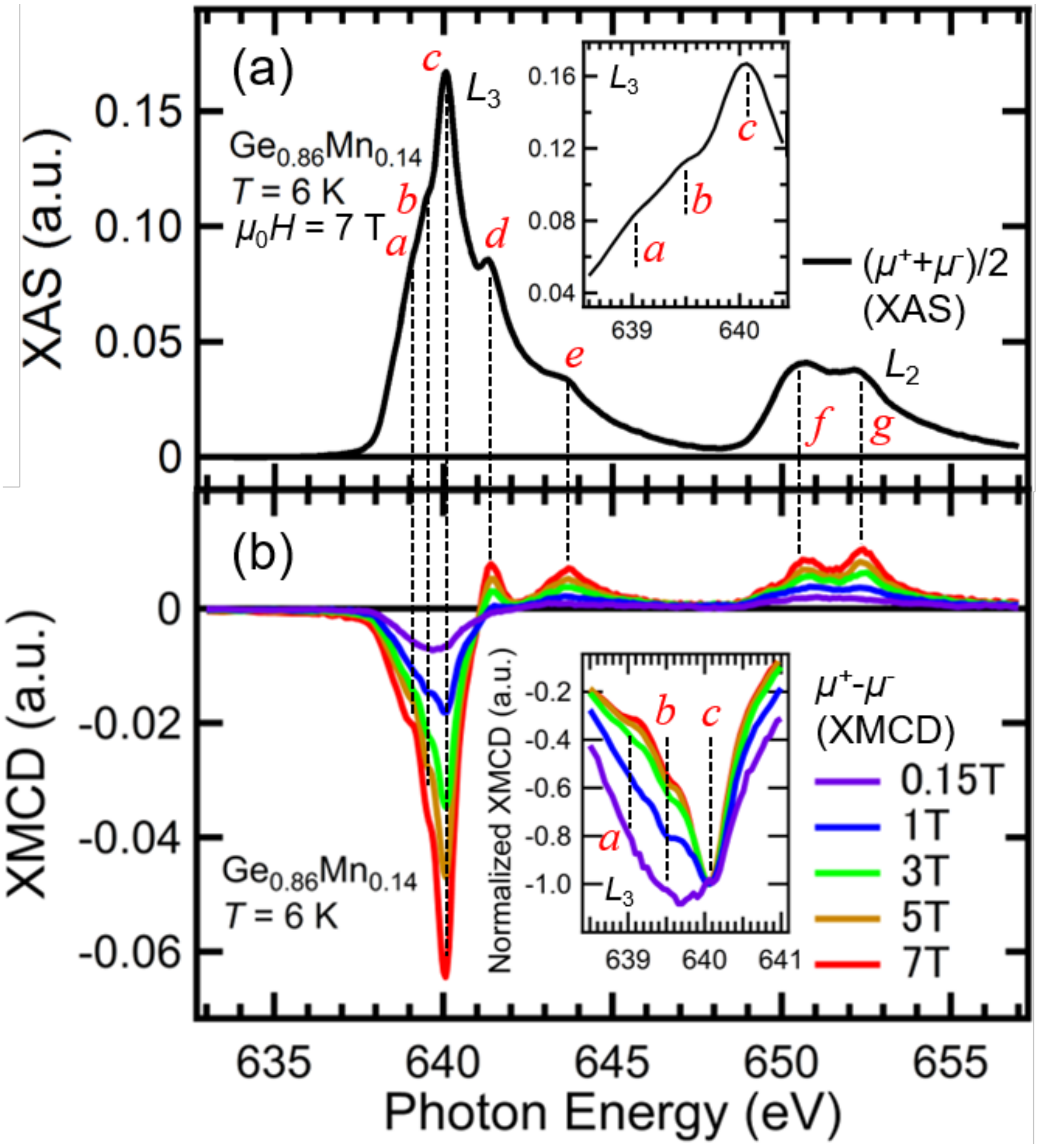

Fig. 47. (a) Mn $L_{2,3}$-edge XAS [$(\mu^+ + \mu^-)/2$] spectrum for the $Ge_{0.86}Mn_{0.14}$ film at 6 K with a magnetic field $\mu_0 H$ = 7 T applied perpendicular to the film surface. The inset shows a magnified plot of the spectrum at the Mn L_3 edge. (b) Mn $L_{2,3}$-edge XMCD ($= \mu^+ - \mu^-$) spectra for the $Ge_{0.86}Mn_{0.14}$ film at 6 K with various magnetic fields H applied perpendicular to the film surface. The inset shows a magnified plot of the spectra at the Mn L_3 edge. Here, the XMCD data have been normalized at *c*. [Y. K. Wakabayashi *et al.*, Physical Review B **95**, 014417 (2017).]

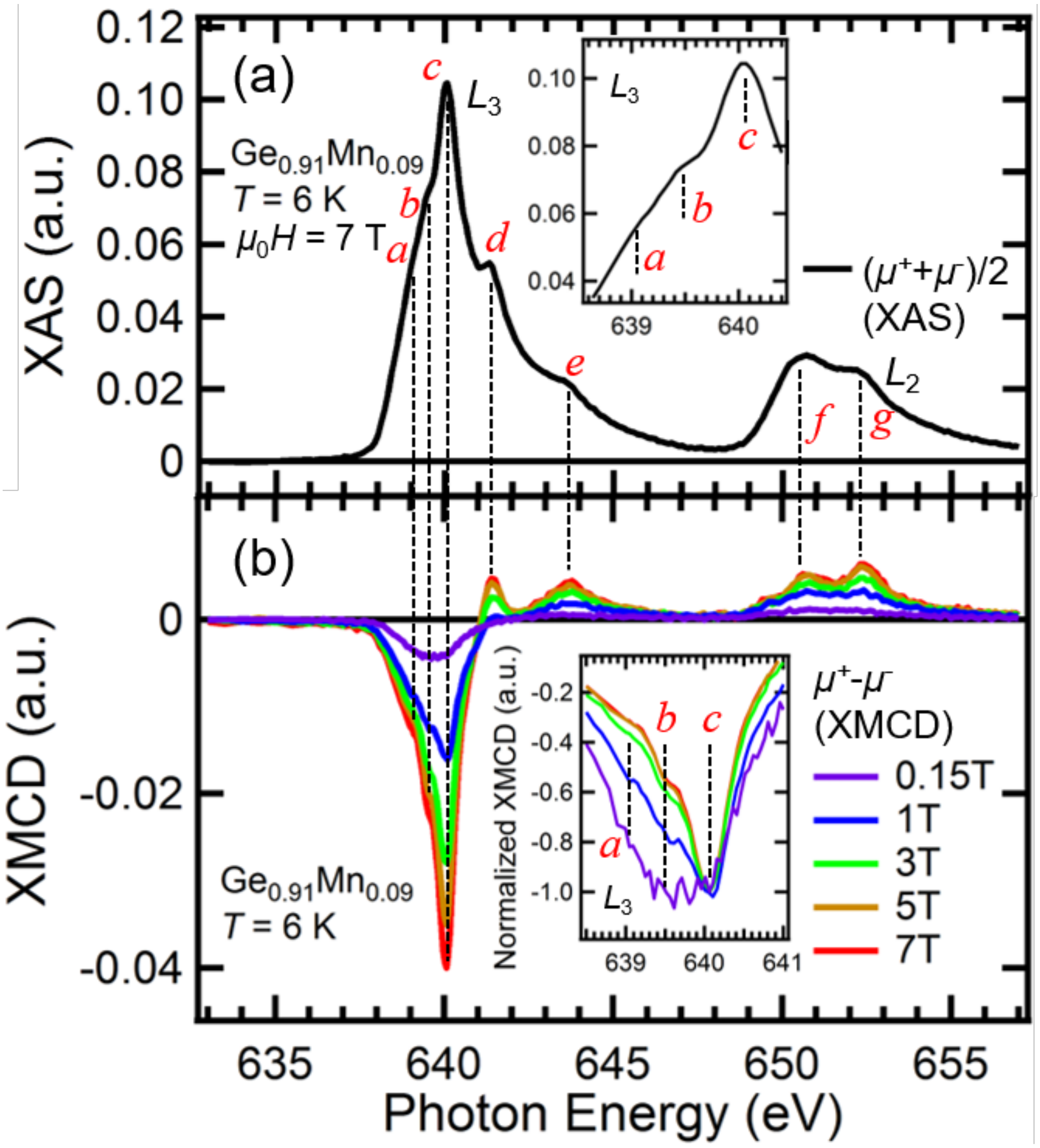

Fig. 48. (a) Mn $L_{2,3}$-edge XAS [$(\mu^+ + \mu^-)/2$] spectrum for the $Ge_{0.91}Mn_{0.09}$ film at 6 K with $\mu_0H = 7$ T applied perpendicular to the film surface. The inset shows a magnified plot of the spectrum at the Mn L_3 edge. (b) Mn $L_{2,3}$-edge XMCD ($= \mu^+ - \mu^-$) spectra for the $Ge_{0.91}Mn_{0.09}$ film at 6 K with various H applied perpendicular to the film surface. The inset shows a magnified plot of the spectra at the Mn L_3 edge, where the XMCD data are normalized to 640.06 eV. The black dashed lines indicate the peak positions. [Y. K. Wakabayashi *et al.*, Physical Review B **95**, 014417 (2017).]

By analyzing the XMCD - H curves measured at various energies and temperatures T for both samples with $x = 0.09$ and 0.14, we decomposed the XMCD signals into an FM(-like) component, which saturates at high magnetic fields (> 6 T), and a PM component, which is linear in the range of $\mu_0 H$ from –1 to 1 T and follows the Brillouin function.

Figure 49(a),(b) shows the H dependence of the XMCD intensity measured at 6 K for the $Ge_{0.86}Mn_{0.14}$ film at (a) a and (b) c, respectively. These curve shapes are largely different. These curves are composed of an FM-like component $I_{FM}(H)$, which saturates at high magnetic fields (> 6 T), and a PM component $I_{PM}(H)$, which is linear in the range of $\mu_0 H$ from –1 T to 1 T and follows the Brillouin function. That is,

$$I_{XMCD}(H, a) = \alpha(a)\, I_{FM}(H) + \beta(a)\, I_{PM}(H) \tag{28}$$

$$I_{XMCD}(H, c) = \alpha(c)\, I_{FM}(H) + \beta(c)\, I_{PM}(H), \tag{29}$$

where $I_{XMCD}(H, E)$ is the XMCD intensity at an energy E under H, and $\alpha(E)$ and $\beta(E)$ are E dependent constants. Here, $I_{FM}(H)$ and $I_{PM}(H)$ are normalized to 1 at 7 T.

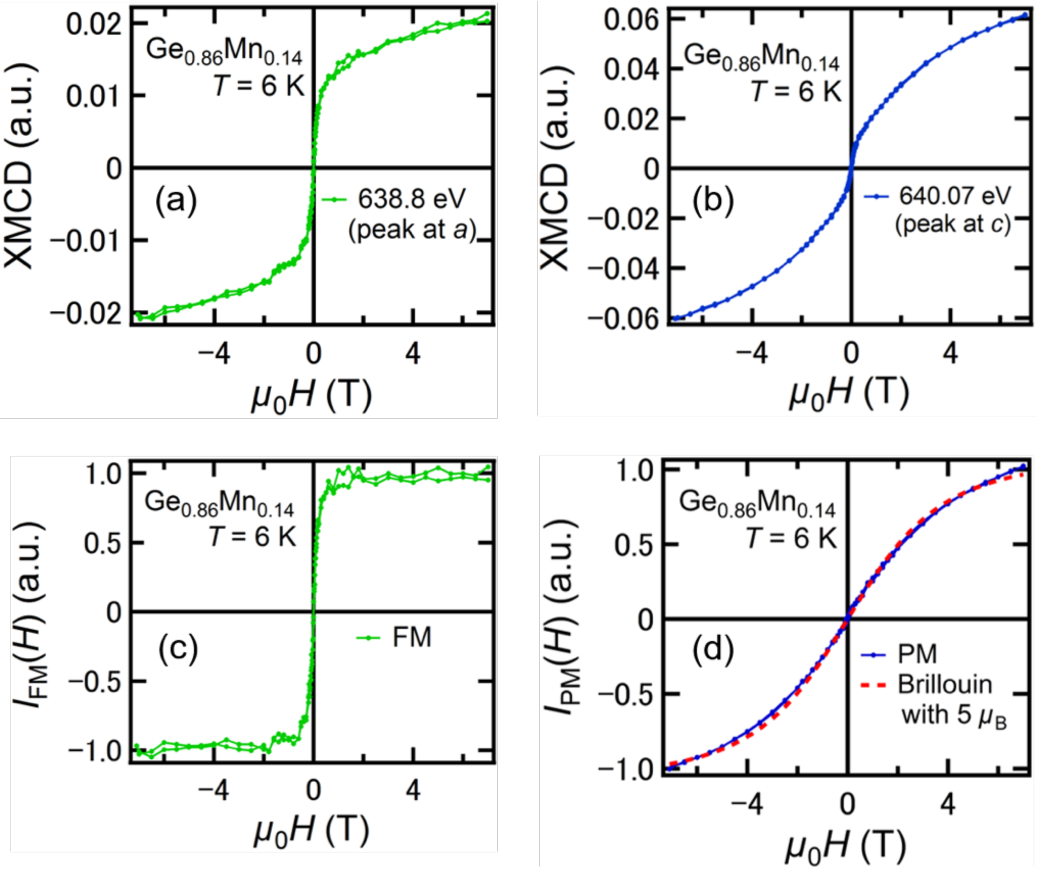

Fig. 49. (a),(b) H dependence of the XMCD intensity measured at 6 K for the $Ge_{0.86}Mn_{0.14}$ film at (a) 638.8 eV (peak at a) and (b) 640.07 eV (peak at c). (c),(d) Derived (c) FM and (d) PM components of the XMCD-H curves for the $Ge_{0.86}Mn_{0.14}$ film. The red dashed curve is the Brillouin function with the magnetic moment of 5 μ_B at 6 K. [Y. K. Wakabayashi *et al*., Physical Review B **95**, 014417 (2017).]

Here, we determine $I_{\mathrm{FM}}(H)$ and $I_{\mathrm{PM}}(H)$ from the XMCD-H curves at a and c. By subtracting Eq.(28)×$\beta(a)/\beta(c)$ from Eq.(29), we obtain

$$I_{\mathrm{XMCD}}(H,a) - \gamma I_{\mathrm{XMCD}}(H,c) = \lambda I_{\mathrm{FM}}(H). \tag{30}$$

Here,

$$\gamma = \frac{\beta(a)}{\beta(c)}, \quad \lambda = \alpha(a) - \alpha(c)\frac{\beta(a)}{\beta(c)}.$$

λ is just a constant for normalization of $I_{\mathrm{FM}}(H)$. We determined γ so that $I_{\mathrm{XMCD}}(H,a) - \gamma I_{\mathrm{XMCD}}(H,a)$, i.e. $I_{\mathrm{FM}}(H)$, saturates when $\mu_0 H > 6$ T. Then, we can derive $I_{\mathrm{FM}}(H)$ [Fig. 49(c)].

Similarly, for the determination of $I_{\mathrm{PM}}(H)$, we obtain

$$I_{\mathrm{XMCD}}(H,c) - \eta I_{\mathrm{XMCD}}(H,a) = \xi I_{\mathrm{PM}}(H) \tag{31}$$

from Eqs. (28) and (29). Here,

$$\eta = \frac{\alpha(c)}{\alpha(a)}, \quad \xi = \beta(c) - \beta(a)\frac{\alpha(c)}{\alpha(a)}.$$

We determined ξ so that $I_{\mathrm{XMCD}}(H,a) - \eta I_{\mathrm{XMCD}}(H,a)$, i.e. $I_{\mathrm{PM}}(H)$, becomes linear in the range of $\mu_0 H$ from -1 T to 1 T. This is because the magnetization curve of paramagnetic spins is generally linear in this magnetic field range (from –1 to 1 T) as long as the moment of the spin is lower than $10\mu_{\mathrm{B}}$. Then, we can derive $I_{\mathrm{PM}}(H)$ [Fig. 49(d)].

The FM component is attributed to the FM Mn atoms in the Mn-rich nanoparticles. The derived PM component of the XMCD-H curve follows the Brillouin function with the magnetic moment of 5 μ_{B} (total angular momentum J=5/2), as shown in Fig. 49(d). Thus, the PM component of the XMCD signal originates from the PM Mn^{2+} ions with $n_{3\mathrm{d}}$ = 5 (5 μ_{B}), where $n_{3\mathrm{d}}$ is the number of 3d electrons per Mn^{2+}.

Figure 50(a)-(g) shows the XMCD-H curves (red solid curves) measured at 6 K for the $\mathrm{Ge}_{0.86}\mathrm{Mn}_{0.14}$ film at various energies. These XMCD-H curves show various shapes depending on E. As shown in Figs. 50(a)-(g), the experimental XMCD-H curves at various energies are well fitted by the linear combination of $I_{\mathrm{FM}}(H)$ and $I_{\mathrm{PM}}(H)$, which were derived above (black dashed curves). Using the same procedure, the XMCD-H curves at various energies also for the $\mathrm{Ge}_{0.91}\mathrm{Mn}_{0.09}$ film are well fitted by the linear combination of $I_{\mathrm{FM}}(H)$ and $I_{\mathrm{PM}}(H)$ derived using the XMCD-H curves at a and c for the $\mathrm{Ge}_{0.91}\mathrm{Mn}_{0.09}$ film (see Figs. 51 and 52). These results indicate that the XMCD spectra are entirely composed only of the FM-like and PM components derived above.

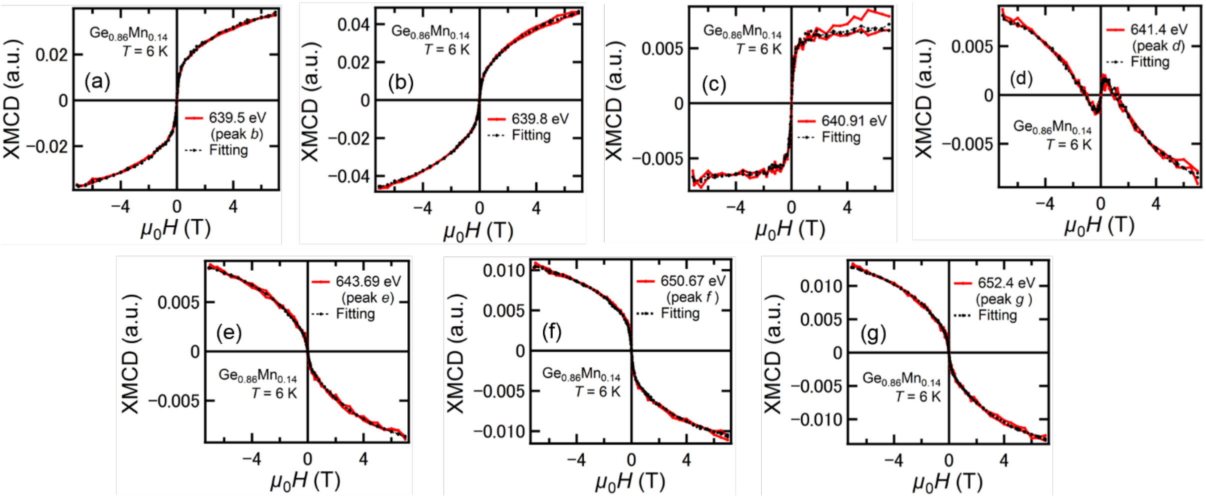

Fig. 50. Experimental XMCD-*H* curves (red solid curves) at various energies at 6 K and the fitting curves (black dashed curves) expressed by the linear combination of $I_{\mathrm{FM}}(H)$ and $I_{\mathrm{PM}}(H)$ for the $Ge_{0.86}Mn_{0.14}$ film. [Y. K. Wakabayashi *et al.*, Physical Review B **95**, 014417 (2017).]

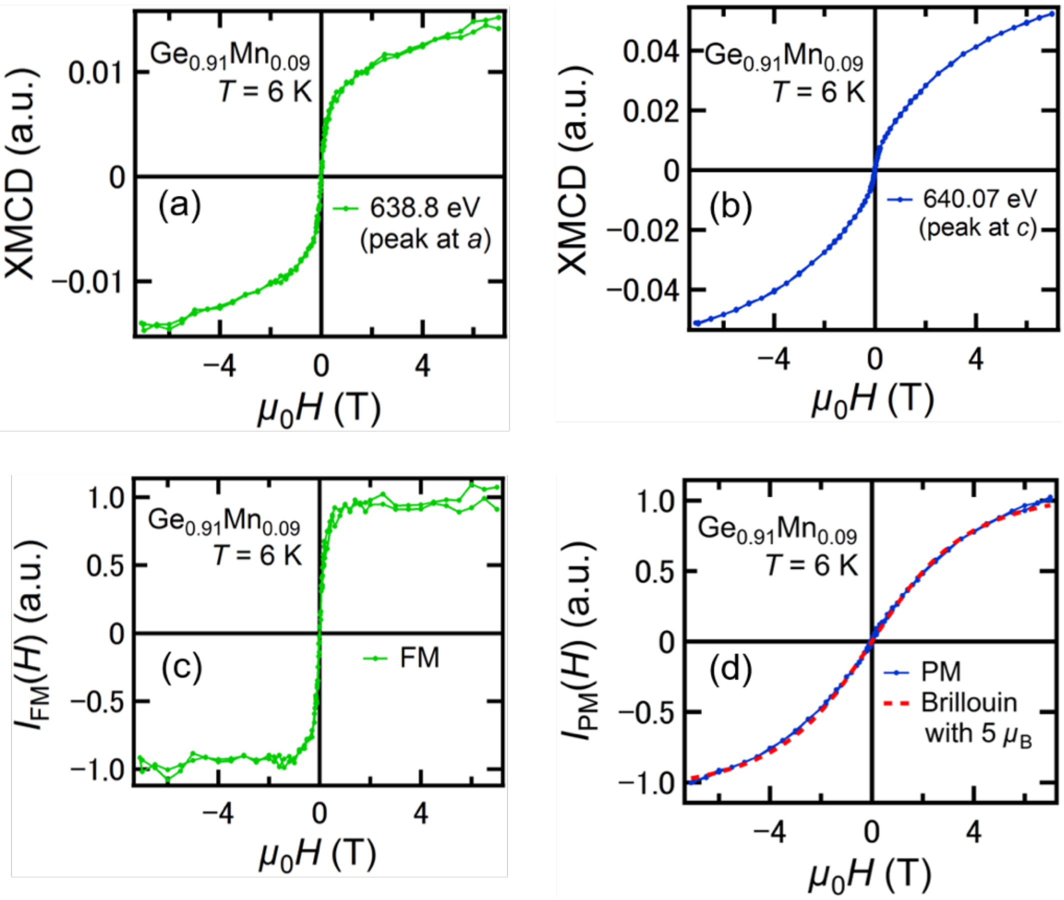

Fig. 51. (a),(b) *H* dependence of the XMCD intensities measured at 6 K for the $Ge_{0.91}Mn_{0.09}$ film at (a) 638.8 eV (peak at *a*) and (b) 640.07 eV (peak at *c*). (c),(d) Derived (c) FM and (d) PM components of the XMCD-*H* curves for the $Ge_{0.91}Mn_{0.09}$ film. The red dashed curve is the Brillouin function with the magnetic moment of 5 μ_B at 6 K. [Y. K. Wakabayashi *et al.*, Physical Review B **95**, 014417 (2017).]

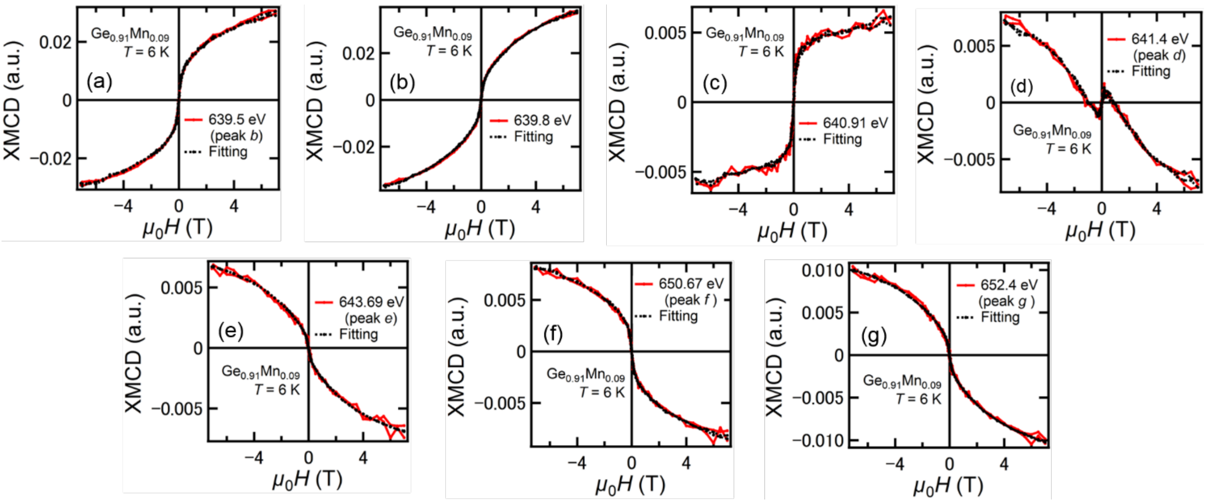

Fig. 52. Experimental XMCD-*H* curves (red solid curves) at various energies at 6 K and the fitting curves (black dashed curves) expressed by the linear combination of $I_{\mathrm{FM}}(H)$ and $I_{\mathrm{PM}}(H)$ for the $Ge_{0.91}Mn_{0.09}$ film. [Y. K. Wakabayashi *et al*., Physical Review B **95**, 014417 (2017).]

One example of the decomposition of the XMCD signal for $Ge_{0.86}Mn_{0.14}$ is shown in Fig. 53. The following results verify our decomposition procedure of the XMCD signals. The Curie plot (*H*/XMCD - *T*) of the derived PM component of the XMCD was linear, which is typical PM behavior and confirms that the PM component is derived correctly in our study (see Fig. 54). In Fig. 53(b), the FM component of the XMCD becomes zero at 200 K, which means that local ferromagnetism appears below 200 K.[14,15,19,20] This result is consistent with previous studies of GeMn granular films. [14,15,19,20] Similar features were also observed in $Ge_{0.91}Mn_{0.09}$ (see Fig. 55)

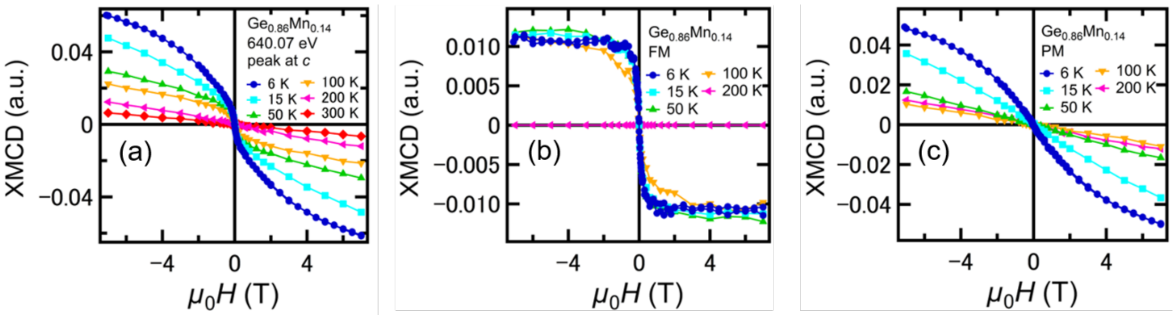

Fig. 53. (a)-(c) Experimentally obtained XMCD-*H* curves (a) and derived FM (b) and PM (c) components of the XMCD-*H* curves for the $Ge_{0.86}Mn_{0.14}$ film at various temperatures. [Y. K. Wakabayashi *et al*., Physical Review B **95**, 014417 (2017).]

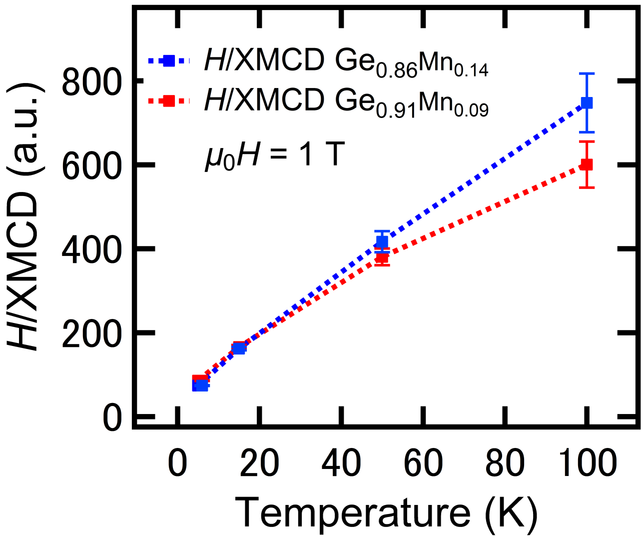

Fig. 54. Temperature dependence of H/XMCD of the PM matrix with $\mu_0 H = 1$ T applied perpendicular to the film surface for the $Ge_{0.86}Mn_{0.14}$ film (blue symbols) and $Ge_{0.91}Mn_{0.09}$ film (red symbols). [Y. K. Wakabayashi *et al.*, Physical Review B **95**, 014417 (2017).]

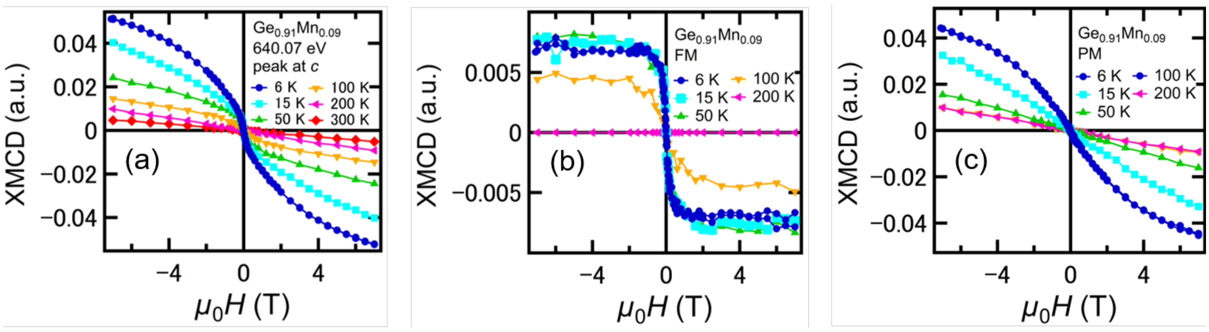

Fig. 55. (a)-(c) Experimentally obtained XMCD-H curves (a), and derived FM (b) and PM components (c) of the XMCD-H curves for the $Ge_{0.91}Mn_{0.09}$ film at various temperatures. [Y. K. Wakabayashi *et al.*, Physical Review B **95**, 014417 (2017).]

From the above analysis, we derived the FM and PM components of the XMCD signal at various energies for both samples, as shown by the green and blue points in Fig. 56, respectively, for both samples. The FM component of the XMCD spectra has a broad single negative peak at the Mn-L_3 edge. This is a typical feature that can be observed for the delocalized 3d electrons of the FM Mn atoms in metallic materials. This result confirms that the FM component indeed originates from the Mn-rich nanoparticles, each of which is locally metallic. The PM component of the XMCD signal is attributed to the Mn-poor matrix. The PM component of the XMCD spectra has three peaks at c, d, and e at the Mn-L_3 edge (Fig. 56), which is a characteristic feature of the localized 3d state of the Mn^{2+} ions with a magnetic moment of $5\mu_B$.[34, 122, 123] From the Brillouin function that expresses the PM component of the XMCD-H curve at 6 K, the magnetic moment of the PM component is also estimated to be $5\mu_B$ [see Figs. 49(d) and 51(d)]. These are characteristic features of the Mn atoms in insulating materials and are consistent with the insulating behavior of the matrix region of GeMn, which is evidenced by the variable range hopping transport observed in GeMn.[15,20]

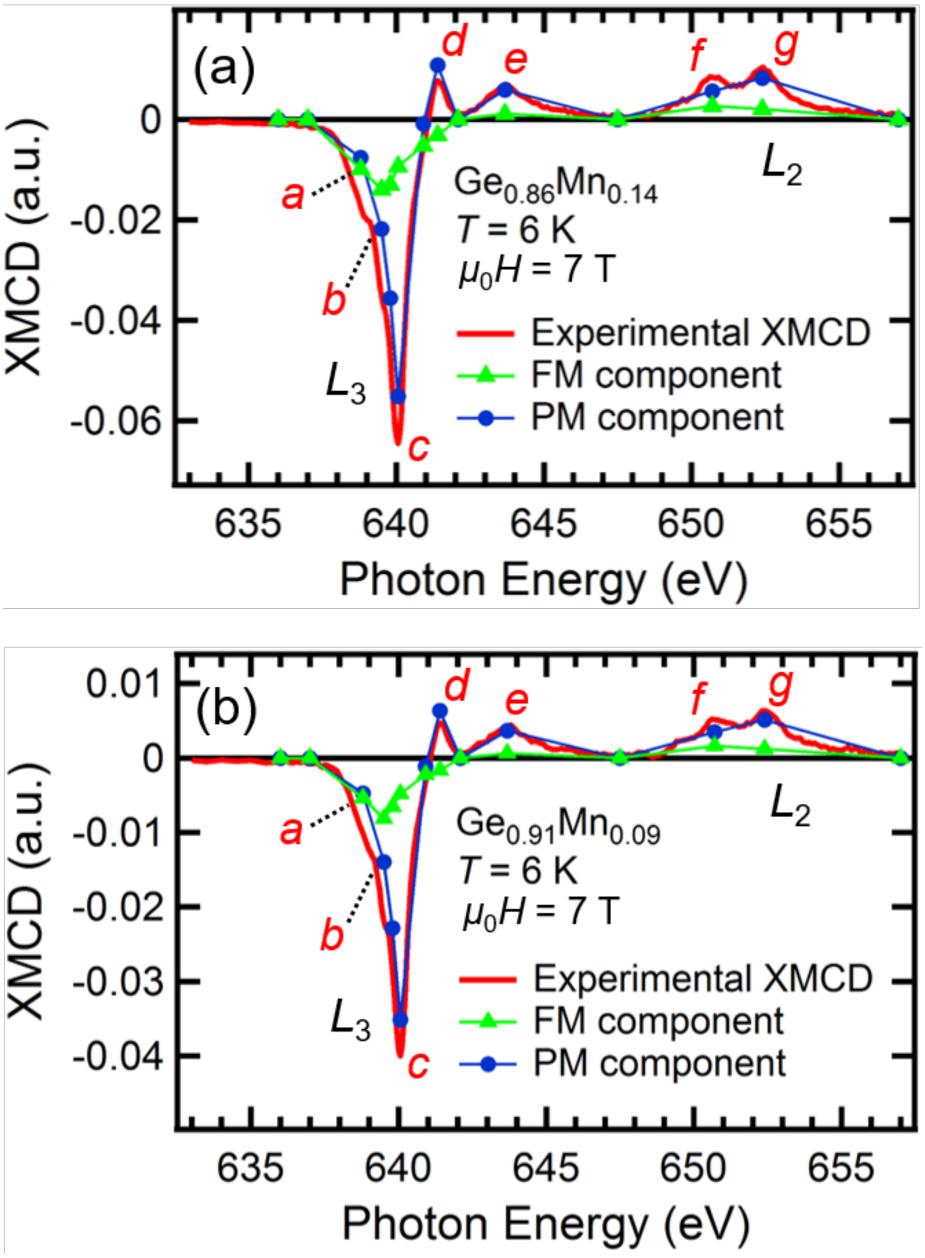

Fig. 56. (a),(b) Experimentally obtained XMCD spectra (red curve) and derived FM (green triangles) and PM (blue circles) components of the XMCD spectra at 6 K with $\mu_0H = 7$ T applied perpendicular to the film surface for the $Ge_{0.86}Mn_{0.14}$ film (a) and $Ge_{0.91}Mn_{0.09}$ film (b). [Y. K. Wakabayashi *et al.*, Physical Review B **95**, 014417 (2017).]

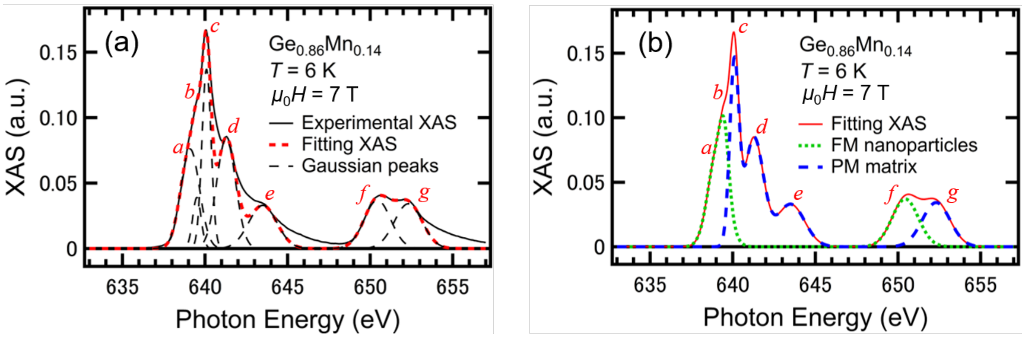

Fig. 57. (a) Experimental XAS spectrum (black curve) measured at 6 K with $\mu_0H = 7$ T applied perpendicular to the film surface for the $Ge_{0.86}Mn_{0.14}$ film, and fitting XAS spectrum (red dashed curve) expressed by the sum of the Gaussian peaks located at *a*-*g* (black dashed curves). (b) Fitting XAS spectrum (red curve) and derived XAS spectra of the FM nanoparticles (green dashed curve) and PM matrix (blue dashed curve). [Y. K. Wakabayashi *et al*., Physical Review B **95**, 014417 (2017).]

In order to derive the XAS spectra of the FM nanoparticles and PM matrix, we fitted the sum of the Gaussian peaks located at *a*-*g* to the XAS spectra measured for the $Ge_{0.86}Mn_{0.14}$ film at 6 K with $\mu_0H = 7$ T applied perpendicular to the film surface [Fig. 57(a)]. Here, we decompose the fitting spectrum into that of the FM nanoparticles and that of the PM matrix. At the Mn L_3 edge, the Gaussian peaks at *a*, *b* are attributed to the FM nanoparticles because the FM component of the XMCD intensity is strongest at *b* and because the FM component of the XMCD intensity is stronger than the PM component at *a* [see Fig. 56(a)]. At the Mn L_3 edge, the Gaussian peaks at *c*, *d*, and *e* are attributed to the PM matrix because the PM component of the XMCD intensity is stronger than the FM component at *c*, *d*, and *e* [see Fig. 56(a)]. At the Mn L_2 edge, the Gaussian peak at *f* (*g*) is attributed to the FM nanoparticles (the PM matrix) because the FM component (PM component) of the XMCD intensity has a peak at *f* (*g*) [see Fig. 56(a)]. Thus, the XAS spectrum of the FM nanoparticles (PM matrix) is expressed as a sum of the Gaussian peaks at *a*, *b*, and *f* (*c*, *d*, *e*, and *g*). Figure 57(b) shows the fitting XAS spectrum [this is the same curve as that shown in Fig. 57(a)], and the derived XAS spectra of the FM nanoparticles and PM matrix for the $Ge_{0.86}Mn_{0.14}$ film. Similarly to the derived FM (PM) component of the XMCD spectra [see Fig. 56(a)], the derived XAS spectrum of the FM nanoparticles has a broad peak composed of the Gaussian peaks at *a* and *b* at the Mn L_3-edge. The derived XAS spectra of the PM Mn atoms have three peaks at *c*, *d*, and *e* at the Mn-L_3 edge, which is consistent with the result of the first-principles calculation of the XAS spectrum of the Mn atoms that substitute for the Ge sites in $Ge_{1-x}Mn_x$.[124] These results indicate that the 3*d* electrons of the FM Mn atoms are *not* localized at each Mn atom and that those of the PM Mn atoms have a localized nature. We also decomposed the XAS spectra into those of the FM nanoparticles and PM matrix for the $Ge_{0.91}Mn_{0.09}$ film using the same procedure. The same features mentioned above were observed for the $Ge_{0.91}Mn_{0.09}$ film as shown in Fig. 58.

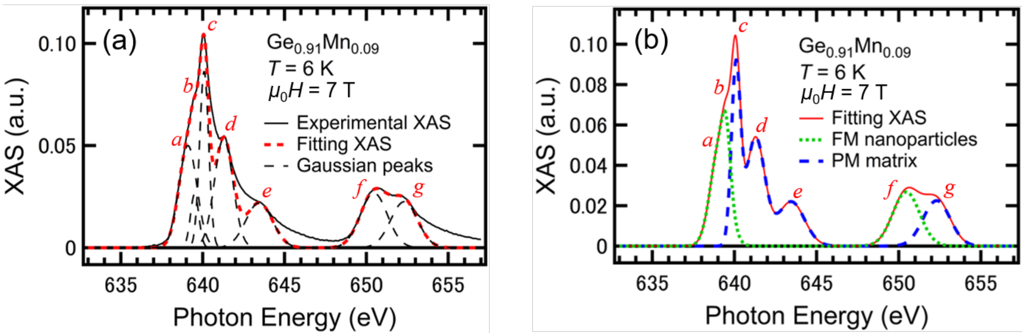

Fig. 58. (a) Experimental XAS spectrum (black curve) measured at 6 K with $\mu_0H = 7$ T applied perpendicular to the film surface for the $Ge_{0.91}Mn_{0.09}$ film, and fitting XAS spectrum (red dashed curve) expressed by the sum of the Gaussian peaks located at *a*-*g* (black dashed curves). (b) Fitting XAS spectrum (red curve) and derived XAS spectra of the FM nanoparticles (green dashed curve) and PM matrix (blue dashed curve). [Y. K. Wakabayashi *et al*., Physical Review B **95**, 014417 (2017).]

We can see characteristic features of the Mn-rich nanoparticles and Mn-poor matrix from the orbital magnetic moment, $m_{\rm orb}$, and the spin magnetic moment, $m_{\rm spin}$, of each region (Table 2), which are obtained by the well-established procedure using the XMCD sum rules separately.[24,94,125] Figure 59(a) shows the derived XAS spectrum of the FM nanoparticles (solid curve) and its integration from 635 eV (dashed curve) for the $Ge_{0.86}Mn_{0.14}$ film. Figure 59(b) shows the derived FM component of the XMCD spectrum (solid curve) and its integration from 635 eV (dashed curve) for the $Ge_{0.86}Mn_{0.14}$ film. Figures 60(a) and 60(b) show the same data for the PM matrix. For the XMCD sum-rules analyses, we define r, p, and q as the following equations.

$$r = \int_{E_3+E_2} \frac{(\mu^+ + \mu^-)}{2} dE, \tag{32}$$

$$p = \int_{E_3} (\mu^+ - \mu^-) dE, \tag{33}$$

$$q = \int_{E_3+E_2} (\mu^+ - \mu^-) dE, \tag{34}$$

where E_3 (635-648 eV) and E_2 (648-665 eV) represent the integration energy ranges for the L_3 and L_2 absorption edges, respectively. We used the XMCD sum rules, which are expressed as follows:

$$m_{\rm orb} = -\frac{2q}{3r}(10 - n_{3d}), \tag{35}$$

$$m_{\rm spin} + 7m_{\rm T} = -\frac{3p-2q}{r}(10 - n_{3d}), \tag{36}$$

where n_{3d} and m_T are the number of $3d$ electrons of the Mn atom and the expectation value of the intra-atomic magnetic dipole operator, respectively. For the Mn^{2+} ions in the Mn-poor matrix, we took n_3d to be 5 and the correction factor for m_spin to be 0.68.[95] We neglected m_T for the PM Mn^{2+} ions in the Mn-poor matrix because it is negligibly small at the T_d symmetry site.[94] For the Mn atoms in the FM nanoparticles, because the valence is unknown, we took n_3d to be 4 – 6 and the correction factor for m_spin to be from –0.5 to 0.5.[95] We neglected m_T for the Mn atoms in the FM Mn-rich nanoparticles because these regions have sphere-like shapes (see Fig. 45).[126] As seen in Table 2, for both samples, the m_spin value of the PM Mn^{2+} ions (~2.4 μ_B) is lower than the ideal m_spin value of Mn^{2+} (i.e. 5 μ_B). This suggests that some of the Mn atoms in the Mn-poor matrix are magnetically inactive.[34,79,80] The large $m_\mathrm{orb}/m_\mathrm{spin}$ (= 0.12 – 0.39) value of the FM Mn atoms is a characteristic property observed in magnetic nanoparticles.[127] By contrast, the m_orb value of the PM matrix vanishes for both samples, confirming that the valence of the PM Mn atoms is 2+ with n_{3d} = 5. The m_spin and m_orb values of the PM Mn^{2+} ions are comparable between $\mathrm{Ge}_{0.91}\mathrm{Mn}_{0.09}$ and $\mathrm{Ge}_{0.86}\mathrm{Mn}_{0.14}$. This indicates that the Mn^{2+} ions in the Mn-poor matrix are isolated and that the localized $3d$ state of the Mn^{2+} ions is not affected by the total Mn concentration x. On the other hand, for the FM nanoparticles, the $\mathrm{Ge}_{0.86}\mathrm{Mn}_{0.14}$ film has slightly larger m_spin and m_orb values than the $\mathrm{Ge}_{0.91}\mathrm{Mn}_{0.09}$ film. This means that the $3d$ electrons in the FM nanoparticles are delocalized and that they are influenced by the surrounding environment (i.e. local concentration of Mn) because each Mn-rich nanoparticle is locally metallic.

Because XMCD preferentially detects Mn atoms located near the top interfaces of the nanoparticles, the magnetic properties obtained via SQUID, which detects the magnetic properties of the entire film, are different from our XMCD results. Whereas we do not see hysteresis in the XMCD-*H* curves (Figs. 49 and 51), it is observed in the SQUID measurements (Fig. 61).[20,128] Thus, in the nanoparticles, the magnetic property of the interface is different from that at the core. As mentioned below, the holes located near these interfaces experience first order magnetic scattering and thus have a key role in causing the large MR. This means that the selective detection capability of XMCD is uniquely suited for investigation of first order magnetic scattering in GeMn.

Table 2. The m_spin, m_orb, and $m_\mathrm{orb}/m_\mathrm{spin}$ values of the Mn atoms in the FM nanoparticles and PM Mn^{2+} ions in the $\mathrm{Ge}_{0.91}\mathrm{Mn}_{0.09}$ film and $\mathrm{Ge}_{0.86}\mathrm{Mn}_{0.14}$ film. [Y. K. Wakabayashi *et al*., Physical Review B **95**, 014417 (2017).]

	FM Mn atoms		**PM Mn^{2+} ions**	
	$\mathrm{Ge}_{0.91}\mathrm{Mn}_{0.09}$	**$\mathrm{Ge}_{0.86}\mathrm{Mn}_{0.14}$**	**$\mathrm{Ge}_{0.91}\mathrm{Mn}_{0.09}$**	**$\mathrm{Ge}_{0.86}\mathrm{Mn}_{0.14}$**
m_spin	0.45-2.05	0.56-2.49	2.45	2.43
m_orb	0.16-0.24	0.22-0.32	0	0
$m_\mathrm{orb}/m_\mathrm{spin}$	0.12-0.36	0.13-0.39	0	0

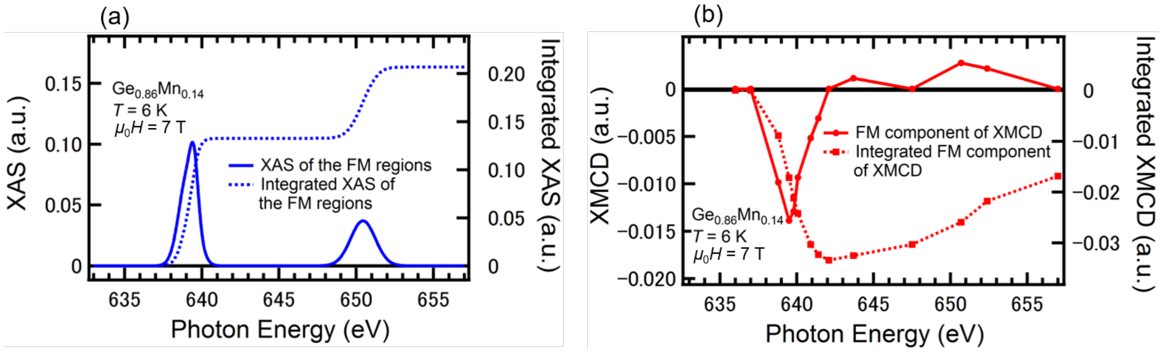

Fig. 59. (a) Derived XAS spectrum of the FM nanoparticles (solid curve) and its integration from 635 eV (dashed curve) for the $Ge_{0.86}Mn_{0.14}$ film. (b) Derived FM component of the XMCD spectrum (solid curve) and its integration from 635 eV (dashed curve) for the $Ge_{0.86}Mn_{0.14}$ film. [Y. K. Wakabayashi *et al.*, Physical Review B **95**, 014417 (2017).]

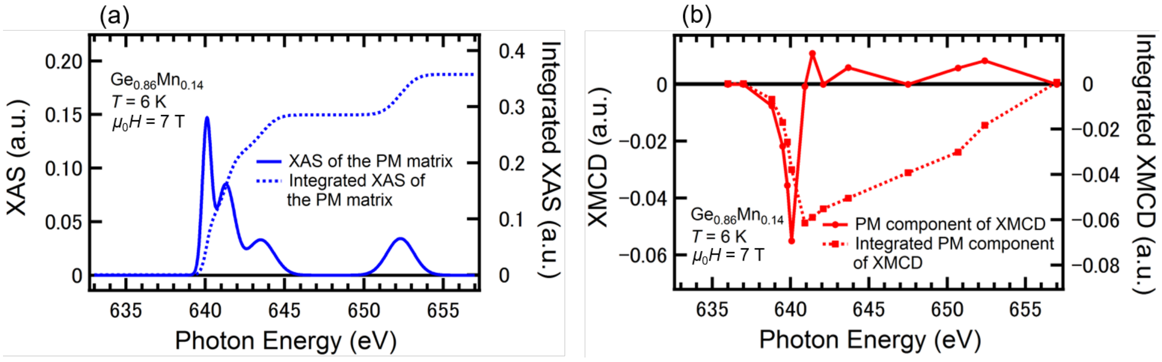

Fig. 60. (a) Derived XAS spectrum of the PM matrix (solid curve) and its integration from 635 eV (dashed curve) for the $Ge_{0.86}Mn_{0.14}$ film. (b) Derived PM component of the XMCD spectrum (solid curve) and its integration from 635 eV (dashed curve) for the $Ge_{0.86}Mn_{0.14}$ film. [Y. K. Wakabayashi *et al.*, Physical Review B **95**, 014417 (2017).]

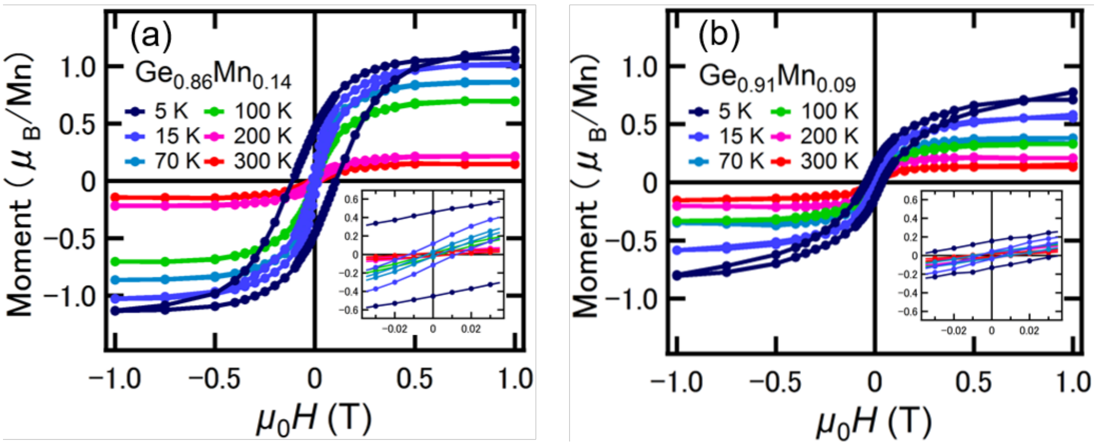

Fig. 61. (a),(b) The *H* dependence of the magnetization measured by SQUID for the $Ge_{0.86}Mn_{0.14}$ film (a) and for the $Ge_{0.91}Mn_{0.09}$ film (b) at various temperatures. [Y. K. Wakabayashi *et al.*, Physical Review B **95**, 014417 (2017).]

5. 4. Spin-dependent transport

The blue, black, and gray curves in Fig. 62(a),(b) show the MR ratio, defined as $[\rho(H) - \rho(0)]/\rho(0)$, of the (a) $Ge_{0.86}Mn_{0.14}$ and (b) $Ge_{0.91}Mn_{0.09}$ films. Here, $\rho(H)$ represents the resistivity of the GeMn films with H applied perpendicular to the film surface. The magnetic field dependence of the product of the FM and PM components of the XMCD intensity is also plotted (red curves). Below the percolation temperature ($T_p \approx 10$ K) of GeMn,[20,129] the MR curves for both samples exhibit a spike-shaped curve, which is specific to the GeMn granular films. Additionally, the MR exhibits a large enhancement below T_p. The MR ratio reaches 199% and 109% at 6 K (< T_p) when $\mu_0 H = 9$ T in $Ge_{0.86}Mn_{0.14}$ and $Ge_{0.91}Mn_{0.09}$, respectively. We see that the MR ratio is proportional to the product of the FM and PM components of the XMCD intensities [Fig. 62(a),(b)]. This means that the MR is induced by first-order magnetic scattering of spin-polarized holes,[130] which is expressed as

$$\mathrm{MR} = -4P_{\mathrm{FM}} \frac{M_{\mathrm{FM}}(H)}{|M_{\mathrm{FM}}(H)|} \frac{J_{\mathrm{pd}}}{g\mu_{\mathrm{B}}V} M_{\mathrm{PM}}(H), \tag{37}$$

where P_{FM}, J_{pd}, g, V, $M_{\mathrm{FM}}(H)$, and $M_{\mathrm{PM}}(H)$ represent the spin polarization of holes in the FM regions, the *p-d* exchange coupling constant between the holes and the PM Mn atoms, the *g*-factor, the field-independent part of the potential, the magnetization of the FM Mn atoms, and the magnetization of the PM Mn atoms, respectively. The sign of the MR depends on the signs of P_{FM} and J_{pd}. Generally, below T_p, spin-polarized holes in the FM Mn-rich regions penetrate into the Mn-poor matrix and overlap with other holes that are extended from different Mn-rich nanoparticles [see Figs. 62(c) and 62(d)]. This induces percolation and long-range FM ordering.[14,15,19,20,129] Thus, our results indicate that the spin-polarized holes, which are extended from the nanoparticles, undergo first order magnetic scattering from the PM Mn atoms in the matrix below T_p and that this scattering induces the large positive MR.[14,15,19,20]

When $T > T_p$, the MR was significantly reduced, and the shape of the MR curve changed to concave [Fig. 62(a)]. This means that the origin of the MR is different between $T > T_p$ and $T < T_p$. The MR above T_P does not follow a parabolic curve, which indicates that it is not a conventional MR that originates from the Lorentz force. In GeMn, the resistivity has a bump at $T = T_p$.[15,20] By increasing H, the spins tend to be aligned, and percolation can occur more easily, which leads to an increase in T_p. Thus, when $T > T_p$, the resistivity increases with increasing H, reflecting the approach of T_p to the measurement temperature.[14,15,20] This induces the small positive MR when $T > T_p$.

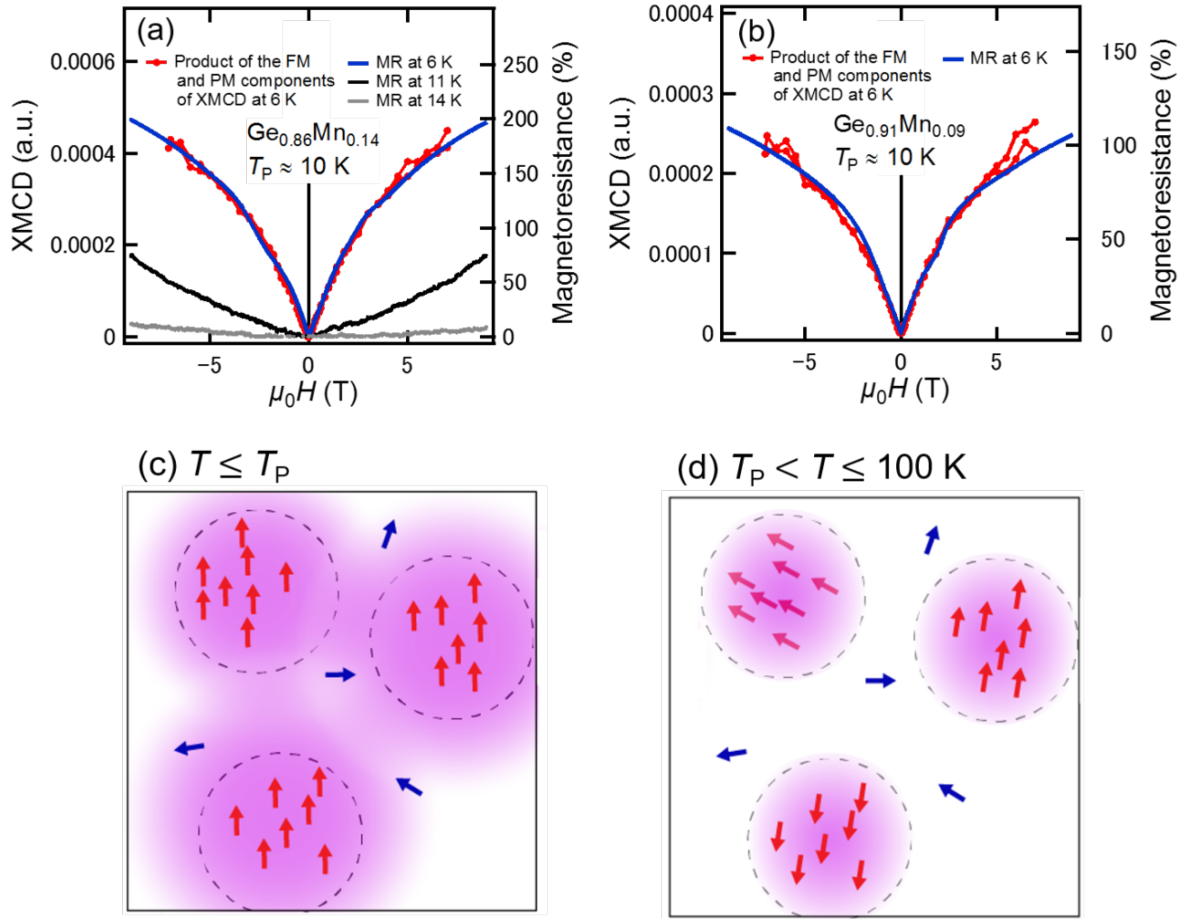

Fig. 62. (a),(b) MR ratio (blue, black, and gray curves) as a function of $\mu_0 H$ applied perpendicular to the film surface for (a) the $Ge_{0.86}Mn_{0.14}$ film and (b) the $Ge_{0.91}Mn_{0.09}$ film. The magnetic field dependence of the product of the FM and PM components of the XMCD intensity is also plotted (red points and curves). (c),(d) Schematic illustration of the spatial distribution of the spin-polarized holes (pink regions) originating from the Mn-rich nanoparticles (black dashed circles) when the temperature (c) $T \leq T_p$ and (d) $T_p < T \leq 100$ K. The red and blue arrows correspond to the magnetic moments of the Mn atoms in the FM nanoparticles and PM matrix, respectively. [Y. K. Wakabayashi *et al.*, Physical Review B **95**, 014417 (2017).]

If we take J_{pd}/V=0.17, as reported in (In,Mn)Sb,[130] the spin polarization of the holes in the FM nanoparticles is estimated to be 64%. This large spin polarization is thought to be the origin of the large MR in GeMn below T_p, making GeMn a promising material for future spintronic applications. Via careful analysis of the XMCD results, we separately obtained the detailed magnetic properties of the Mn-rich nanoparticles and the Mn-poor matrix. This unique method will also be useful for other granular materials and magnetic multilayers and will help to understand the mechanism of the MR and yield insight into how to increase the MR ratios of these systems.

In summary of this chapter, we developed a unique method to investigate the magnetic properties of the FM nanoparticles and the PM matrix in GeMn granular thin films separately by utilizing the extremely high sensitivity of XMCD to the local magnetic state of each atom. We revealed that the MR ratio is proportional to the product of the magnetizations of the FM nanoparticles and the PM matrix when $T < T_{\mathrm{p}}$. Below T_{p}, the spin-polarized holes in the FM nanoparticles penetrate into the Mn-poor matrix. Thus, the large MR can be associated with first order magnetic scattering of these extended spin-polarized holes by the PM Mn atoms in the Mn-poor matrix. The spin polarization of the holes in the FM nanoparticles is estimated to be 64%. The large spin polarization makes $Ge_{1-x}Mn_x$ a promising material for future spintronic applications.

Chapter 6: Summary and Prospect

In this study, we have investigated the nanoscale magnetic properties and spin-dependent transports and their relevance to the non-uniformity of the magnetic atoms in the group-IV-based FMS GeFe and the GeMn granular films, which were epitaxially grown on the Ge substrates by LT-MBE, using XRD, TEM, TED, EDX, c-RBS, c-PIXE, AFM, SQUID, MCD, XMCD, and magnetotransport measurements. To investigate the electronic structure and the origin of the ferromagnetism in GeFe, the ARPES measurements were carried out. We grew MTJs composed of epitaxially grown Fe/MgO/$Ge_{0.935}Fe_{0.065}$ to examine the spin-dependent transports. The existence of the spin-polarized carriers at E_F in both materials was confirmed by the spin-dependent transport measurements.

In section 3.1, we investigated the growth-temperature dependence of the properties of the $Ge_{1-x}Fe_x$ films (x = 6.5% and 10.5%), and revealed the correlation of the magnetic properties with the lattice constant, T_C, non-uniformity of Fe atoms, stacking-fault defects, and Fe-atom locations. While T_C strongly depends on the growth temperature, we found a universal relationship between T_C and the lattice constant, which does not depend on the Fe concentration x. By using TED combined with EDX, we found that the density of the stacking-fault defects and the non-uniformity of the Fe concentration are correlated with T_C. Meanwhile, by using the c-RBS and c-PIXE measurements, we clarified that about 15% of the Fe atoms exist on the tetrahedral interstitial sites in the $Ge_{0.935}Fe_{0.065}$ lattice and that the substitutional Fe concentration is *not* correlated with T_C. Considering these results, we concluded that the non-uniformity of the Fe concentration plays an important role in determining the ferromagnetic properties of GeFe.

In section 3.2, we reported the annealing-induced enhancement of ferromagnetism and nano-particle formation in the GeFe film. We successfully increased T_C of the $Ge_{0.895}Fe_{0.105}$ film up to 210 K while keeping a nearly single FM phase when the annealing temperature is lower than 600°C. In contrast, when it is annealed at 600°C, single-crystal GeFe nano-particles with stacking faults and twins, which have high T_C up to room temperature, are formed in the film. We showed that the non-uniformity of the Fe concentration plays an essential role in determining the ferromagnetism in both cases. Although all the GeFe films show weak spin-glass-like behavior in a very low-temperature region (lower than ~26 K), which is insensitive to the annealing temperature, due to the non-uniform distribution of the Fe atoms, the ferromagnetism is much stronger than the spin glass and it dominates the system.

In section 3.3, we investigated the local electronic structure and magnetic properties of GeFe using XMCD. Our results show that the doped Fe 3*d* electrons are strongly hybridized with the Ge 4*p* states, and have a large orbital magnetic moment relative to the spin magnetic moment; i.e., $m_{\mathrm{orb}}/m_{\mathrm{spin}} \approx 0.1$. We found that nanoscale local ferromagnetic regions, which are formed through FM exchange interactions in the high-Fe-content regions of the GeFe films, exist even at room temperature, well above the T_{C} of 20 – 100 K. We observed intriguing nanoscale expansion of the local FM regions with decreasing temperature, followed by a transition of the entire film into a FM state at the T_{C}.

In section 3.4, we investigated the electronic structure of the GeFe using ARPES measurements. We observed the clear band dispersion in the GeFe and that the E_{F} is located 0.35 eV above the VBM of the host Ge. Furthermore, the RPES spectrum showed that finite Fe 3*d* components contribute to the states at the E_{F}. These results indicate that the impurity band model seems to be applicable for GeFe, and that the FM interaction is mediated by the double-exchange interaction between the Fe 3*d* impurity levels.

In chapter 4, we confirmed the existence of the spin-polarized carriers at E_{F} in GeFe by the first successful observation of the TMR in MTJs containing a group-IV FMS, that is, in MTJs composed of epitaxially grown Fe/MgO/$\mathrm{Ge_{0.935}Fe_{0.065}}$. We found that the p-$d(t_2)$ band in GeFe is mainly responsible for the tunneling transport. Although the obtained TMR ratio is small (~0.3%), the TMR ratio is expected to be enhanced by suppressing a leak current through amorphous-like crystal domains observed in MgO.

In chapter 5, we revealed the origin of the unique large positive MR in GeMn granular films. We developed a unique method to separately investigate the magnetic properties of the nanoparticles and the matrix, utilizing the extremely high sensitivity of XMCD to the local magnetic state of each atom. We found that the MR ratio is proportional to the product of the magnetizations originating from the nanoparticles and the matrix. This result indicates that the spin-polarized holes in the nanoparticles penetrate into the matrix and that these holes undergo first order magnetic scattering by the PM Mn atoms in the matrix, which induces the large MR.

In both group-IV-based FMS GeFe and the GeMn granular films, the non-uniformity of magnetic atoms plays an important role in the nanoscale magnetic properties and spin-dependent transports. In GeFe, the enhancement of the non-uniformity of the Fe atoms enhances the double-exchange FM interactions, which are mediated by the Fe 3*d* impurity levels. The non-uniformity of the Fe atoms determines the T_{C} and intriguing nanoscale expansion of the local FM regions formed in the locally high Fe concentration regions with decreasing temperature. The larger the non-uniformity of the Fe distribution is, the larger each local FM region becomes, and the local FM regions can be more easily connected magnetically, resulting in a higher T_C. Thus, to achieve room-temperature ferromagnetism and realize Si or Ge-based spin devices utilizing spin-polarized carriers, which were confirmed by the TMR effect, adequate enhancement of the non-uniformity of Fe atoms is needed.

The positive MR in the $Ge_{0.86}Mn_{0.14}$ film, in which the local Mn concentration in the FM nanoparticles is ~60%, is twice as large as that in the $Ge_{0.91}Mn_{0.09}$ film, in which the local Mn concentration in the FM nanoparticles is ~40%. This means that the enhancement of the non-uniformity of the Mn atoms enhances the spin polarization of the holes in the FM nanoparticles.

To realize Si or Ge-based spin devices utilizing the unique nanoscale magnetic properties and spin-dependent transports owing to the non-uniformity of the magnetic atoms in the Ge-based ferromagnetic epitaxial films (the group-IV FMS GeFe and the GeMn granular films), adequate enhancement of the non-uniformity of the magnetic atoms is necessary.

Referencens

[1] M. N. Baibich, J. M. Broto, A. Fert, F. Nguyen Van Dau, F. Petroff, P. Eitenne, G. Creuzet, A. Friederich, and J. Chazelas, Phys. Rev. Lett., **61**, 2472 (1988).

[2] G. Binasch, P. Grünberg, F. Saurenbach, and W. Zinn, Phys. Rev. B, **39**, 4828 (1989).

[3] S. Sugara and M. Tanaka, Appl. Phys. Lett. **84**, 2307 (2004).

[4] T. Tahara, H. Koike, M. Kameno, T. Sasaki, Y. Ando, K. Tanaka, S. Miwa, Y. Suzuki, and M. Shiraishi, Appl. Phys. Express **8**, 113004 (2015).

[5] C. H. Lee, T. Nishimura, C. Lu, S. Kabuyanagi and A. Toriumi, IEEE International Electron Devices Meeting (IEDM) 2014 32.5.

[6] M. Kim, Y. Wakabayashi, R. Nakane, M. Yokoyama, M. Takenaka, and S. Takagi, IEEE International Electron Devices Meeting (IEDM) (2014) pp. 331-334

[7] M. Kim, Y. K. Wakabayashi, M. Yokoyama, R. Nakane, M. Takenaka, and S. Takagi, IEEE Trans. on Electron Dev. **62**, 9 (2015).

[8] Y. Shuto, M. Tanaka, and S. Sugahara, Jpn. J. Appl. Phys. **47**, 7108 (2008).

[9] Y. Shuto, M. Tanaka, and S, Sugahara, Appl. Phys. Lett. **90**, 132512 (2007).

[10] Y. Ban, Y. Wakabayashi, R. Akiyama, R. Nakane, and M. Tanaka, AIP Advances **4**, 097108 (2014).

[11] Y. Shuto, M. Tanaka, and S. Sugahara, J. Appl. Phys. **99**, 08D516 (2006).

[12] Y. Shuto, M. Tanaka, and S, Sugahara, Phys. Stat. Sol. (c) **3**, 4110 (2006).

[13] Y. D. Park, A. T. Hanbicki, S. C. Erwin, C. S. Hellberg, J. M. Sullivan, J. E. Mattson, T. F. Ambrose, A. Wilson, G. Spanos, and B. T. Jonker, Science **295**, 651 2002.

[14] A. P. Li, J. Shen, J. R. Thompson, and H. H. Weitering, Appl. Phys. Lett. **86**, 152507 (2005).

[15] A. P. Li, J. F. Wendelken, J. Shen, L. C. Feldman, J. R. Thompson, and H. H. Weitering, Phys. Rev. B **72**, 195205 (2005).

[16] M. Jamet, A. Barski, T. Devillers, V. Poydenot, R. Dujardin, B.-G. Pascale, J. Rothman, Edith B.-A., A. Marty, J. Cibert, R. Mattana, and S. Tatarenko, Nat. Mater. **5**, 653 (2006).

[17] I.-S. Yu, M. Jamet, T. Devillers, A. Barski, P. Bayle-Guillemaud, C. Beigne, J. Rothman, V. Baltz, and J. Cibert, Phys. Rev. B **82**, 035308 (2010).

[18] P. Dalmas de Reotier, E. Prestat, P. Bayle-Guillemaud, M. Boukhari, A. Barski, A. Marty, M. Jamet, A. Suter, T. Prokscha, Z. Salman, E. Morenzoni, and A. Yaouanc, Phys. Rev. B **91**, 245408 (2015).

[19] R. B. Morgunov, A. I. Dmitriev, and O. L. Kazakova, Phys. Rev. B **80**, 085205 (2009).

[20] R. Akiyama, R. Nakane, Y. K. Wakabayashi, and M. Tanaka, unpublished

[21] C. Jaeger, C. Bihler, T. Vallaitis, S. T. B. Goennenwein, M. Opel, R. Gross, and M. S. Brandt, Phys. Rev. B **74**, 045330 (2006).

[22] T. Dietl, K. Sato, T. Fukushima, A. Bonanni, M. Jamet, A. Barski, S. Kuroda, M. Tanaka, P. N. Hai, and H. Katayama-Yoshida, Rev. Mod. Phys. **87**, 1311 (2015)

[23] M. Richardson, Acta Chem. Scand. **21**, 2305 (1967).

[24] C. T. Chen, Y. U. Idzerda, H. -J. Lin, N. V. Smith, G. Meigs, E. Chaban, G. H. Ho, E. Pellegrin, and F. Sette, Phys. Rev. Lett. **75**, 152 (1995).

[25] J. L. Shay and W. E. Spicer, Phys. Rev. **161**, 799 (1967).

[26] L. Ley, R. A. Pollak, F. R. McFeely, S. P. Kowalczyk, and D. A. Shirley, Phys. Rev. B **9**, 600 (1974).

[27] W. S. Fann, R. Storz, H. W. K. Tom, and J. Bokor, Phys. Rev. B **46**, 13592 (1992).

[28] S. Yuasa, T. Nagahama, A. Fukushima, Y. Suzuki, and K. Ando, Nat. Matter. **3**, 868 (2004).

[29] Y. K. Wakabayashi, S. Ohya, Y. Ban, and M. Tanaka, J. Appl. Phys. **116**, 173906 (2014).

[30] K. Ando, T. Hayashi, M. Tanaka, and A. Twardowski, J. Appl. Phys. **83**, 6548 (1998).

[31] K. Ando, H. Saito, V. Zayets and M. C. Debnath, J. Phys.: Condens. Matter **16**, S5541 (2004).

[32] Y. K. Wakabayashi, Y. Ban, S. Ohya, and M. Tanaka, Phys. Rev. B **90**, 205209 (2014).

[33] H. Saito, V. Zayets, S. Yamagata, and K. Ando, Phys. Rev. Lett. **90**, 207202 (2003).

[34] Y. Takeda, M. Kobayashi, T. Okane, T. Ohkochi, J. Okamoto, Y. Saitoh, K. Kobayashi, H. Yamagami, A. Fujimori, A. Tanaka, J. Okabayashi, M. Oshima, S. Ohya, P. N. Hai, and M. Tanaka, Phys. Rev. Lett. **100**, 247202 (2008).

[35] S. Kuroda, N. Ozaki, N. Nishizawa, T. Kumekawa, S. Marcet, and K. Takita, Sci. Technol. Adv. Mater. **6**, 558 (2005).

[36] E. H. C. P. Sinnecker, G. M. Penello, T. G. Rappoport, M. M. Sant' Anna, D. E. R. Souza, and M. P. Pires, Phys. Rev. B **81**, 245203 (2010).

[37] A. Lemaitre, A. Miard, L. Travers, O. Mauguin, L. Largeau, C. Gourdon, V. Jeudy, M. Train and J. -M. George, Appl. Phys. Lett. **93**, 021123 (2008).

[38] S. W. Jung, S. -J. An, G. -C. Yi, C. U. Jung, S. -L. Lee, and S. Cho, Appl. Phys. Lett. **80**, 4561 (2002).

[39] L. C. Feldman, J. W. Mayer, and S. T. Picraux, *Materials Analysis by Ion Channeling* (Academic, New York, 1982).

[40] H. Krause, M. Lux, E. Nowak, J. Vogt, R. Flagmeyer, G. Kuhn, and G. Otto, Phys. Stat. Sol. (a) **132**, 295 (1992).

[41] S. Kuroda, S. Marcet, E. B. –Amalric, J. Cibert, H. Mariette, S. Yamamoto, T. Sakai, T. Ohshima, and H. Itoh, Phys. Stat. Sol. (a) **203**, 1724 (2006).

[42] T. Niermann, D. Mai, M. Roever, M. Kocan, J. Zenneck, J. Malindretos, A. Rizzi, and M. Seibt, J. Appl. Phys. **103**, 073520 (2008).

[43] B. B. Nielsen, J. U. Anderson, and S. J. Pearton, Phys. Rev. Lett. **60**, 321 (1988).

[44] B. B. Nielsen, Phys. Rev. B **37**, 6353 (1988).

[45] V. V. Beloshitsky, F. F. Komarov, and M. A. Kumakhov, Phys. Rep. **6**, 293 (1986).

[46] M. A. Kumakhov, Phys. Lett. **32**, 538 (1970).

[47] B. Domeij, G. Flada, and N. G. E. Johanson, Rad. Eff. **6**, 155 (1970).

[48] R. B. Alexander, P. T. Callaghan, and J. M. Poate, Phys. Rev. B **9**, 3022 (1974).

[49] K. M. Yu, W. Walukiewicz, L. Y. Chan, R. Leon, E. E. Haller, J. M. Jaklevic, and C. M. Hanson, J. Appl. Phys. **74**, 86 (1993).

[50] K. M. Yu, W. Walukiewicz, T. Wojtowicz, I. Kuryliszyn, X. Liu, Y. Sasaki, and J. K. Furdyna, Phys. Rev. B **65**, 201303 (2002).

[51] K. M. Yu, W. Walukiewicz, T. Wojtowicz, J. Denlinger, M. A. Scarpulla, X. Liu, and J. K. Furdyna, Appl. Phys. Lett. **86**, 042102 (2005).

[52] L. X. Zhao, C. R. Staddon, K. Y. Wang, K. W. Edmonds, R. P. Campion, B. L. Gallagher, and C. T. Foxon, Appl. Phys. Lett. **86**, 071902 (2005).

[53] M. S. Paterson, J. Appl. Phys. **23**, 805 (1952).

[54] S. K. Pradhan and M. De, J. Appl. Phys. **64**, 2324 (1988).

[55] D. Rafaja, C. Krbetschek, D. Borisova, G. Schreiber, and V. Klemm, Thin Solid Films **530**, 105 (2013).

[56] L. Bergqvist, O. Eriksson, J. Kudrnovsky, V. Drchal, P. Korzhavyi, and I. Turek, Phys. Rev. Lett. **93**, 137202 (2004).
[57] K. Sato, H. Katayama-Yoshida, and P. H. Dederichs, Jpn. J. Appl. Phys. **44**, L948 (2005).
[58] S. Hibert and W. Nolting, Phys. Rev. B **70**, 165203 (2004).
[59] G. Bouzerar, T. Ziman, and J. Kudrnovsky, Europhys. Lett. **69**, 812 (2005).
[60] F. Xiu, Y. Wang, X. Kou, P. Upadhyaya, Y. Zhou, J. Zou, and K. L. Wang, J. Am. Chem. Soc. **132**, 11425 (2010).
[61] P. N. Hai, S. Ohya, and M. Tanaka, Nat. Nanotech. **5**, 593 (2010).
[62] P. N. Hai, S. Ohya, M. Tanaka, S. E. Barnes, and S. Maekawa, Nature **458**, 489 (2009).
[63] K. W. Edmonds, P. Bogusławski, K. Y. Wang, R. P. Campion, S. N. Novikov, N. R. S. Farley, B. L. Gallagher, C. T. Foxon, M. Sawicki, T. Dietl, M. Buongiorno Nardelli, and J. Bernholc, Phys. Rev. Lett, **92**, 037201 (2004).
[64] M. Malfait, J. Vanacken, V. V. Moshchalkov, W. Van Roy, and G. Borghs, Appl. Phys. Lett. **86**, 132501 (2005).
[65] T. J. Konno and R. Sinclair, Mater. Chem. Phys. **35**, 99 (1993).
[66] K. Ando, H. Saito, K. C. Agarwal, M. C. Debnath, and V. Zayets, Phys. Rev. Lett. **100**, 067204 (2008).
[67] K. Hamaya, T. Watanabe, T. Taniyama, A.Oiwa, Y. Kitamoto, and Y. Yamazaki, Phys. Rev. B **74**, 045201 (2006).
[68] V. Cannella and J. A. Mydosh, Phys. Rev. B **6**, 4220 (1972).
[69] J. R. L. de Almeida and D. J. Thouless, J. Phys. A **11**, 983 (1978).
[70] B. Martinez, X. Obradors, Ll. Balcells, A. Rouanet, and C. Monty, Phys. Rev. Lett. **80**, 181 (1998).
[71] S. Tardif, V. Favre-Nicolin, F. Lancon, E. Arras, M. Jamet, A. Barski, C. Porret, P. Bayle-Guillemaud, P. Pochet, T. Devillers, and M. Rovezzi, Phys. Rev. B **82**, 104101 (2010).
[72] E. Arras, F. Lancon, I. Slipukhina, E. Prestat, M. Rovezzi, S. Tardif, A. Titov, P. Bayle-Guillemaud, F. d'Acapito, A. Barski, V. Favre-Nicolin, M. Jamet, J. Cibert, and P. Pochet, Phys. Rev. B **85**, 115204 (2012).
[73] B. Shin, J. P. Leonard, J. W. McCamy, and M. J. Aziz, Appl. Phys. Lett. **87**, 181916 (2005).
[74] T. Fukushima, K. Sato, H. Katayama-Yoshida, and P. H. Dederichs, Phys. Stat. Sol. (a) **203**, 2751 (2006).
[75] K. Kanematsu, K. Yasukochi, and T. Ohoyama, J. Phys. Soc. Japan **18**, 920 (1963).
[76] E. Adelson and A. E. Austin, J. Phys. Chem. Solids **26**, 1795 (1965).
[77] K. Yasukochi and K. Kanematsu, J. Phys. Soc. Japan **16**, 429 (1961).
[78] D. P. DiVincenzo, O. L. Alerhand, M. Schlüter, and J. W. Wilkins, Phys. Rev. Lett. **56**, 1925 (1986).
[79] Y. K. Wakabayashi, S. Sakamoto, Y. Takeda, K. Ishigami, Y. Takahashi, Y. Saitoh, H. Yamagami, A. Fujimori, M. Tanaka, and S. Ohya, Sci. Rep. **6**, 23295 (2016).
[80] S. Ahlers, P. R. Stone, N. Sircar, E. Arenholz, O. D. Dubon, and D. Bougeard, Appl. Phys. Lett. **95**, 151911 (2009).
[81] D. J. Keavney, D. Wu, J. W. Freeland, E. J. Halperin, D. D. Awschalom, and J. Shi, Phys. Rev. Lett. **91**, 187203 (2003).
[82] K. W. Edmonds, N. R. S. Farley, T. K. Johal, G. V. D. Laan, R. P. Campiom, B. L.

Gallegher, and C. T. Foxon, Phys. Rev. B **71**, 064418 (2005).

[83] D. J. Keavney, S. H. Cheung, S. T. King, M. Weinert, and L. Li, Phys. Rev. Lett. **95**, 257201 (2005).

[84] V. R. Singh, K. Ishigami, V. K. Verma, G. Shibata, Y. Yamazaki, T. Kataoka, A. Fujimori, F. -H. Chang, D. -J. Lin, C. T. Chen, Y. Yamada, T. Fukumura, and M. Kawasaki, Appl. Phys. Lett. **100**, 242404 (2012).

[85] S. Kuroda, N. Nishizawa, K. Takita, M. Mitome, Y. Bando, K. Osuch, and T. Dietl Nat. Phys. **6**, 440-446 (2007).

[86] D. Bougeard, S. Ahlers, A. Trampert, N. Sircar, and G. Abstreiter, Phys. Rev. Lett. **97**, 237202 (2006).

[87] Y. Saitoh, Y. Fukuda, Y. Takeda, H. Yamagami, S. Takahashi, Y. Asano, T. Hara, K. Shirasawa, M. Takeuchi, T. Tanaka, and H. Kitamura, J. Synchrotron Rad. **19**, 388 (2012)

[88] T. J. Regan, H. Ohldag, C. Stamm, F. Nolting, J. Luning, J. Stohr, and R. L. White, Phys. Rev. B **64**, 214422 (2001).

[89] R. Kumar, A. P. Singh, P. Thakur, K. H. Chae, W. K. Choi, B. Angadi, S. D. Kaushik, and S. Panaik, J. Phys. D: Appl. Phys. **41**, 155002 (2008).

[90] E. Sakai, K. Amemiya, A. Chikamatsu, Y. Hirose, T. Shimada, and T. Hasegawa, J. Magn. Magn. Mater, **333**, 130 (2013).

[91] G. V. D. Laan and I. W. Kirkman, J. Phys.: Condens. Matter **4**, 4189 (1992).

[92] I. A. Kowalik, A. Persson, M. A. Nino, A. Na, A. Navarro-Quezada, B. Faina, A. Bonanni, T. Dietl, and D. Arvanits, Phys. Rev. B **85**, 184411 (2012).

[93] K. Mamiya, T. Koide, A. Fujimori, H. Tokano, H. Manaka, A. Tanaka, H. Toyosaki, T. Fukumura, and M. Kawasaki, Appl. Phys. Lett. **89**, 062506 (2006).

[94] J. Stohr and H. Konig, Phys. Rev. Lett. **75**, 3748 (1995).

[95] C. Piamonteze, P. Miedema, and F. M. F. de Groot, Phys. Rev. B **80**, 184410 (2009).

[96] Y. Park, S. Adenwalla, G. P. Felcher, and S. D. Bader, Phys. Rev. B **52**, 12779 (1995).

[97] K. M Chowdary and S. A. Majetich, J. Phys. D: Apple. Phys. **47**, 1750001 (2014).

[98] Y. K. Wakabayashi, R. Akiyama, Y. Takeda, M. Horio, G. Shibata, S. Sakamoto, Y. Ban, Y. Saitoh, H. Yamagami, A. Fujimori, M. Tanaka, and S. Ohya, Phys. Rev. B, in press.

[99] T. Dietl, Nat. Mater. **9**, 965 (2010).

[100] T. Jungwirth, J. Sinova, J. Ma_sek, J. Ku_cera, and A. H. MacDonald, Rev. Mod. Phys. **78**, 809 (2006).

[101] J. Okabayashi, A. Kimura, O. Rader, T. Mizokawa, A. Fujimori, T. Hayashi, and M. Tanaka, Phys. Rev. B **64**, 125304 (2001).

[102] S. Ohya, K. Takata, and M. Tanaka, Nat. Phys. **7**, 342 (2011).

[103] S. Sakamoto, Y. K. Wakabayashi, Y. Takeda, S.-i. Fujimori, H.Suzuki, Y. Ban, H. Yamagami, M. Tanaka, S. Ohya, and A. Fujimori, arXiv:1605.05275.

[104] T. Hayashi, H. Shimada, H. Shimizu, and M. Tanaka, J. Crystal. Growth **201/202**, 689 (1999).

[105] M. Tanaka and Y. Higo, Phys. Rev. Lett. **87**, 026602 (2001).

[106] P. Torelli, M. Sperl, R. Ciancio, J. Fujii, C. Rinaldi, M. Cantoni, R. Bertacco, M. Utz, D. Bougeard, M. Soda, E. Carlino, G. Rossi, C. H. Back, and G. Panaccione, Nanotechnology **23**, 465202 (2012).

[107] W. Han, Y. Zhou, Y. Wang, Y. Li, J. J. I. Wong, K. Pi, A. G. Swartz, K. M. McCreary, F. Xiu, K. L. Wang, J. Zou, and R. K. Kawakami, J. Crystal Growth **312**, 44 (2009).

[108] D. Petti, M. Cantoni, C. Rinaldi, S. Brivio, R. Bertacco, J. Gazquez, and M. Varela, J. Appl. Phys. **109**, 084909 (2011).
[109] M. Cantoni, D. Petti, C. Rinaldi, and R. Bertacco, Appl. Phys. Lett. **98**, 032104 (2011).
[110] W. Wulfhekel, M. Klaua, D. Ullmann, F. Zavaliche, J. Kirschner, R. Urban, T. Monchesky, and B. Heinrich, Appl. Phys. Lett. **78**, 509 (2001).
[111] M.Bowen, V. Cros, F. Petroff, A. Fert, C. M. Boubeta, J. L. C. Kramer, J. V. Anguita, A. Cebollada, F. Briones, J. M. D. Teresa, L. Morellon, M. R. Ibarra, F. Guell, F. Peiro, and A. Cornet, Appl. Phys. Lett. **79**, 1655 (2001).
[112] W. Shen, B. D. Schrag, A. Gridhar, M. J. Carter, H. Sang, and G. Xiao, Phys. Rev. B **79**, 014418 (2009).
[113] M. Julliere, Phys. Lett. A **54**, 225 (1975).
[114] Y. K. Wakabayashi, K. Okamoto, Y. Ban, S. Sato, M. Tanaka, and S. Ohya, Appl. Phys. Express **9**, 123001 (2016).
[115] J.-Q. Wang and G. Xiao, Phys. Rev. B **49**, 3982 (1994).
[116] H. Akinaga, M. Mizuguchu, K, Ono, and M. Oshima, Appl. Phys. Lett. **76**, 357 (2000).
[117] M. Yokoyama, T. Ogawa, A. M. Nazmul, and M. Tanaka, J. Appl. Phys **99**, 08D502 (2006).
[118] R. Nakajima, J. Stohr, and Y. U. Idzerda, Phys. Rev. B **59**, 6421 (1999).
[119] N. Sircar, S. Ahlers, C. Majer, G. Abstreiter, and D. Bougeard, Phys. Rev. B **83**, 125306 (2011).
[120] A. Jain, M. Jamet, A. Barski, T. Devillers, I.-S. Yu, C. Porret, P. Bayle-Guillemaud, V. Favre-Nicolin, S. Gambarelli, V. Maurel, G. Desfonds, J. F. Jacquot, and S. Tardif, J. Appl. Phys. **109**, 013911 (2011).
[121] P. Gambardella, L. Claude, S. Rusponi, K. J. Franke, H. Brune, J. Raabe, F. Nolting, P. Bencok, A. T. Hanbicki, B. T. Jonker, C. Grazioli, M. Veronese, and C. Carbone, Phys. Rev. B **75**, 125211 (2007).
[122] G. van der Laan and B. T. Thole, Phys. Rev. B **43**, 13401 (1991).
[123] C. Hirai, H. Sato, A. Kimura, K. Yaji, K. Iori, M. Taniguchi, K. Hiraoka, T. Muro, and A. Tanaka, Physica B **351**, 341 (2004).
[124] S. Picozzi, L. Ottaviano, M. Passacantando, G. Profeta, A. Continenza, F. Priolo, M. Kim, and A. J. Freema, Appl. Phys. Lett. **86**, 062501 (2005).
[125] B. T. Thole, P. Carra, F. Sette, and G. van der Laan, Phys. Rev. Lett. **68**, 1943 (1992).
[126] O. Sipr, H. Ebert, and J. Minar, J. phys.: Condens. Matter **27**, 056004 (2015).
[127] K. W. Edmonds, C. Binns, S. H. Baker, S. C. Thornton, C. Norris, J. B. Goedkoop, M. Finazzi, and N. B. Brookes, Phys. Rev. B **60**, 472 (1999).
[128] S. Yada, R. Okazaki, S. Ohya, and M. Tanaka, Appl. Phys. Exp. **3**, 123002 (2010).
[129] A. Kaminski and S. Das Sarma, Phys. Rev. Lett. **88**, 247202 (2002).
[130] M. Csontos, T. Wojtowicz, X. Liu, M. Dobrowolska, B. Janko, J. K. Furdyna, and G. Mihaly, Phys. Rev. Lett. **95**, 227203 (2005).

Acknowledgments (謝辞)

本研究を行うにあたり、田中大矢中根研究室の皆様、東京大学物理学専攻 藤森研究室の皆様、日本原子力研究開発機構の皆様に大変お世話になりました。心より感謝と御礼を申し上げます。

田中雅明教授には素晴らしい研究環境を与えていただき、またミーティング等において様々なアドバイスを頂き、大変感謝しております。ご専門の半導体スピントロニクスはもちろんのこと、その他の様々な研究トピックにも精通されており、どのような研究に対しても鋭い指摘をされる姿勢は大変勉強になりました。私も、自らの研究領域だけでなく、広く興味を持って視野の広い研究者になれるよう精進します。

大矢忍准教授には、指導教官として日々議論していただき、研究に関する多くのことを教えて頂きました。本研究において主に使用していたIV族MBE装置の改造やメンテナンスなどの実験技術に関することはもちろんのこと、科学的な文章の書き方や、いかにして分かりやすく意義や論理を相手に伝えるかといった、研究者として必要なライティング、プレゼン技術についても非常に多くのことを学ばせて頂きました。この5年間で頂いた大量の赤ペンの数々は、研究者としての血肉となっていると思います。

藤森淳教授にはSPring-8における放射光測定において、大変お世話になりました。また、放射光測定の実験データの解釈に対する議論おいては、物性物理の専門家がどのように現象を理解していくのかに触れる大変貴重な機会となり、自分の不勉強を痛感いたしました。物理現象を正しく理解するためには、実験と理論両面からのアプローチが重要であると学ばせて頂きました。

中根了昌特任准教授にはプロセスや測定に用いる様々な装置の使い方から、実験家としての心構えなどを教えて頂きました。真摯にデータと向き合い、検証を重ねる姿勢を見習い、私も誠実な研究者でありたいと思います。

また、普段から議論を行い、助言を下さった田中大矢中根研究室の全てのメンバーに感謝します。ありがとうございました。

Publications, awards, and presentations

Publications related to this study (1st author)

[1]（Refereed）Y. K. Wakabayashi, S. Ohya, Y. Ban, and M. Tanaka, “Important role of the non-uniform Fe distribution for the ferromagnetism in group-IV-based ferromagnetic semiconductor GeFe”, Journal of Applied Physics **116**, 173906 (2014).

[2]（Refereed）Y. K. Wakabayashi, Y. Ban, S. Ohya, and M. Tanaka, “Annealing-induced enhancement of ferromagnetism and nano-particle formation in the ferromagnetic semiconductor GeFe”, Physical Review B **90**, 205209 (2014).

[3]（Refereed）Y. K. Wakabayashi, S. Sakamoto, Y. Takeda, K. Ishigami, Y. Takahashi, Y. Saitoh, H. Yamagami, A. Fujimori, M. Tanaka, and S. Ohya, “Room-temperature local ferromagnetism and nanoscale domain growth in the ferromagnetic semiconductor GeFe”, Scientific Reports **6**, 23295 (2016).

[4]（Refereed）Y. K. Wakabayashi, K. Okamoto, Y. Ban, S. Sato, M. Tanaka, and S. Ohya, “Tunneling magnetoresistance in trilayer structures composed of group-IV ferromagnetic semiconductor $Ge_{1-x}Fe_x$, MgO, and Fe”, Applied Physics Express **9**, 123001 (2016). Selected as Spotlights.

[5]（Refereed）Y. K. Wakabayashi, R. Akiyama, Y. Takeda, M. Horio, G. Shibata, S. Sakamoto, Y. Ban, Y. Saitoh, H. Yamagami, A. Fujimori, M. Tanaka, and S. Ohya, “Origin of the large positive magnetoresistance in $Ge_{1-x}Mn_x$ granular thin films”, Physical Review B **95**, 014417 (2017).

Other related publications (coauthor)

[6]（Refereed）Y. Ban, Y. Wakabayashi, R. Akiyama, R. Nakane, and M. Tanaka, “Carrier transport properties of the Group-IV ferromagnetic semiconductor $Ge_{1-x}Fe_x$ with and without boron doping”, AIP advances **4**, 097108 (2014).

[7]（Refereed）S. Sakamoto, Y. K. Wakabayashi, Y. Takeda, S.-i. Fujimori, H. Suzuki, Y. Ban, H. Yamagami, M. Tanaka, S. Ohya, and A. Fujimori, “Electronic Structure of Ferromagnetic Semiconductor Fe-doped Ge Revealed by Soft X-ray Angle-Resolved Photoemission Spectroscopy”, Physical Review B, in press.

[8]（In preparation）R. Akiyama, R. Nakane, Y. K. Wakabayashi, and M. Tanaka, “Structural and magnetic properties of epitaxial $Ge_{1-x}Mn_x$ thin films grown on Ge(111) substrates”, in preparation.

[9]（In preparation）Y. Ban, Y. K. Wakabayashi, R. Nakane, and M. tanaka, “Carrier transport in group-IV ferromagnetic semiconductor $Ge_{1-x}Fe_x$ with nanoscale fluctuations in Fe concentration”, in preparation.

Other publications

[10]（Refereed）M. Kim, Y. Wakabayashi, R. Nakane, M. Yokoyama, M. Takenaka, and S.

Takagi, “High Ion/Ioff Ge-source ultrathin body strained-SOI Tunnel FETs”, IEEE International Electron Devices Meeting (IEDM) 2014, 331 (2014).

[11] （Refereed） M. Kim, Y. K. Wakabayashi, M. Yokoyama, R. Nakane, M. Takenaka, and S. Takagi, “Ge/Si Hetero-Junction Tunnel Field-Effect Transistors and Their Post Metallization Annealing Effect”, IEEE Trans. on Electron Dev. **62**, 9 (2015).

[12] （Refereed） H. Fujiwara, T. Kiss, Y. K. Wakabayashi, Y. Nishitani, T. Mori, Y. Nakata, S. Kitayama, K. Fukushima, S. Ikeda, H. Fushimoto, Y. Minowa, S. -K. Mo, J. Denlinger, J. W. Allen, P. Metcalf, M. Imai, K. Yoshimura, S. Suga, T. Muro, and A. Sekiyama, “Soft X-ray angle-resolved photoemission with micro-positioning techniques for metallic V2O3”, Journal of Synchrotron Radiation 22 (2015).

[13] （In preparation） S. Sakamoto, T. T. Nguyen, Y. Takeda, S.-i. Fujimori, N. H. Pham, D. A. Le, Y. K. Wakabayashi, G. Shibata, M. Horio, K. Ikeda, Y. Saitoh, H. Yamagami, M. Tanaka, and A. Fujimori, “Electronic Structure of the p-type Ferromagnetic Smiconductor (Ga,Fe)Sb”, in preparation.

[14] （In preparation） Y. K. Wakabayashi, Y. Nonaka, Y. Takeda, S. Sakamoto, K. Ikeda, c. Zhendong, Y. Saitoh, H. Yamagami, M. Tanaka, A. Fujimori, and R. Nakane, “Electronic structure and magnetic property of magnetic dead layers in $CoFe_2O_4/Al_2O_3/Si(111)$ films studied by X-ray magnetic circular dichroism (XMCD)”, in preparation.

[15] （In preparation） Y. K. Wakabayashi, Y. Nonaka, Y. Takeda, S. Sakamoto, c. Zhendong, Y. Saitoh, H. Yamagami, M. Tanaka, A. Fujimori, and R. Nakane, “Enhancement of the inversion parameter of ultra thin epitaxial inverse spinel ferrite $Ni_xCo_{1-x}Fe_2O_4$ on Si(111) substrate owing to high site selectivity of Ni”, in preparation.

Review article

[1] （Non-refereed） Y. K. Wakabayashi, “IV 族強磁性半導体 GeFe の物性解明と磁気トンネル接合”, 応用電子物性分科会会誌 **4**, 143 (2016).

Award

[1] 若林勇希, 第62回(2015年春季) 応用物理学会学術講演会 第3回英語講演奨励賞, 2015年3月

[2] Yuki K. Wakabayashi, 9th International Conference on Physics and Applications of Spin-Related Phenomena in Solids (PASPS), Young Researcher Best Poster Award, August 11, 2016.

Invited talks related to this study

[1] ○S. Ohya, Y. K. Wakabayashi, Y. Ban, S. Sakamoto, Y. Takeda, A. Fujimori, and M. Tanaka (invited), “Promising features of the group-IV-based ferromagnetic semiconductor Ge1-xFex”, Energy Materials Nanotechnology (EMN) East Meeting, C08,

Beijing Xijiao Hotel, Beijing, China, April 22, 2015.

[2] ○大矢忍、宗田伊理也、若林勇希、小林正起、坂本祥哉、竹田幸治、伴芳祐、藤森淳、田中雅明, “強磁性半導体の材料開拓と強磁性発現機構の理解”, 第1回放射光連携研究ワークショップ, ステーションコンファレンス東京, 東京, 2015年3月17日.

[3] ○若林 勇希, “IV族強磁性半導体$Ge_{1-x}Fe_x$の物性解明と磁気トンネル接合”, 応用電子物性分科会・スピントロニクス研究会共催「スピントロニクス材料の新展開」, 首都大学東京 秋葉原サテライトキャンパス, 東京, 2016年11月21日

Other invited talks

[3] ○金 閔洙, 若林 勇希, 中根 了昌, 横山 正史, 竹中 充, 高木 信一, “ゲルマニウムソース薄膜ひずみSOIトンネルFETの実現とその電気特性に与えるひずみ、MOS界面、バックバイアスの効果”, 電子情報通信学会シリコン材料・デバイス研究会, 機械振興会館, 東京, 2015年1月27日

[4] ○M. Kim, Y. K. Wakabayashi, R. Nakane, M. Yokoyama, M. Takenaka and S. Takagi, “Effects of strain, interface states and back bias on electrical characteristics of Ge-source UTB strained-SOI tunnel FETs”, 2015年秋季応用物理学会, 18a-1C-1, 名古屋国際会議場, 2015年9月13日-16日

International conferences related to this study

[1] (口頭、査読なし) ○Y. Wakabayashi, Y. Ban, S. Ohya, M. Tanaka, “Annealing-induced enhancement of ferromagnetism and nano-particle formation in ferromagnetic-semiconductor GeFe”, American Physical Society (APS) March Meeting 2014, G8.00009, Colorado Convention Center, Denver, USA, March 3-7, 2014.

[2] (口頭、査読あり) ○Y. Wakabayashi, Y. Ban, S. Ohya, M. Tanaka, “Properties of group-IV based ferromagnetic semiconductor GeFe: Growth temperature, lattice constant, location of Fe atoms and their relevance to the magnetic properties”, International Conference on the Physics of Semiconductors (ICPS) 2014, 15:45-16:00 Oral, Austin Convention Center, Austin, Texas, USA, August 10-15, 2014.

[3] (口頭、査読あり) ○Y. Wakabayashi, Y. Ban, S. Ohya, M. Tanaka, “Properties of group-IV based ferromagnetic semiconductor GeFe: Growth temperature, location of Fe atoms, annealing effect and their relevance to the magnetic properties”, 18th International Conference on Molecular Beam Epitaxy (MBE 2014), ThC2-2, High Country Conference Center, Flagstaff, Arizona, USA, September 7-12, 2014.

[4] (ポスター、査読あり) ○Y. K. Wakabayashi, S. Sakamoto, Y. Takeda, K. Ishigami, Y. Saitoh, H. Yamagami, A. Fujimori, M. Tanaka, and S. Ohya, "Room-temperature local

ferromagnetism and nano-scale domain growth in the ferromagnetic semiconductor $Ge_{1-x}Fe_x$", 17th International Conference on Modulated Semiconductor Structures (MSS-17), Tu-PM-21, Sendai International Center, Sendai, Tokyo, July 26-31, 2015.

[5] (口頭、査読なし) ○Y. K. Wakabayashi, S. Sakamoto, Y. Takeda, K. Ishigami, Y. Saitoh, H. Yamagami, A. Fujimori, M. Tanaka, and S. Ohya, " Observation of the room-temperature local ferromagnetism and its nanoscale growth in the ferromagnetic semiconductor GeFe ", American Physical Society (APS) March Meeting 2016, K19.00011, Baltimore Convention Center, Baltimore, USA, March 14-18, 2016.

[6] (ポスター、査読あり) ○Y. K. Wakabayashi, R. Akiyama, Y. Takeda, M. Horio, G. Shibata, S. Sakamoto, Y. Ban, Y. Saitoh, H. Yamagami, A. Fujimori, M. Tanaka, and S. Ohya, "Origin of the large positive magnetoresistance in $Ge_{1-x}Mn_x$ granular films", P2-15, Kobe International Conference Center, Kobe City, Japan, August 8-11, 2016.

[7] (ポスター、査読あり) ○K. Okamoto, Y. K. Wakabayashi, W. Ashihara, Y. Ban, S. Sato, M. Tanaka, and S. Ohya, "Tunneling magnetoresistance in trilayer structures composed of group-IV ferromagnetic semiconductor $Ge_{1-x}Fe_x$, MgO, and Fe", P1-10, Kobe International Conference Center, Kobe City, Japan, August 8-11, 2016.

[8] (ポスター、査読あり) ○S. Sakamoto, Y. K. Wakabayashi, Y. Takeda, S.-i. Fujimori, H. Suzuki, Y. Ban, H. Yamagami, M. Tanaka, S. Ohya, and A. Fujimori, "Electronic Structure of the ferromagnetic semiconductor $Ge_{1-x}Fe_x$ revealed by soft x-ray angle-resolved photoemission spectroscopy", P2-6, Kobe International Conference Center, Kobe City, Japan, August 8-11, 2016.

[9] (ポスター、査読なし) ○S. Ohya, A. Yamamoto, T. Yamaguchi, R. Ishikawa, R. Akiyama, Y. K. Wakabayashi, S. Kuroda, and M. Tanaka, "Spin injection into the topological crystalline insulator SnTe using spin pumping", International workshop on nano-spin conversion science & quantum spin dynamics, N27, The University of Tokyo, Tokyo, Oct 12-15, 2016.

Other international conferences

[10] (ポスター、査読なし) ○H.Fujiwara, Y.Wakabayashi, 他 10 名,” Metal-insulator transition of LiRh2O4 observed by extremely low energy photoemission and HAXPES”, 12th International Conference Electronic Spectroscopy and structure (ICESS), NE-2-PO-FUJ-02, Palais des Congres-Saint-Maro, France, September 17-19, 2012.

[11] (ポスター, 査読無なし) ○H.Fujiwara, Y.Wakabayashi, 他 12 名, ” Evidence of constant U across metal-insulator transition and Fermi surfaces of V2O3 revealed by HAXPES and micro soft-X-ray ARPES”, 12th International Conference Electronic Spectroscopy and structure (ICESS), NE-2-PO-FUJ-01, Palais des Congres-Saint-Maro, France,

September 17-19, 2012.

[12]（口頭、査読あり）○M. Kim, Y. Wakabayashi, R. Nakane, M. Yokoyama, M. Takenaka and S. Takagi, “Electrical Characteristics of Ge/Si Hetero-Junction Tunnel Field-Effect Transistors and their Post Annealing Effects”, 2013 International Conference on Solid State Devices and Materials (SSDM 2013), B-6-2, Hilton Fukuoka Sea Hawk, Fukuoka, Japan, September 24-27, 2013.

[13]（口頭、査読なし）○M. Kim, Y. Wakabayashi, R. Nakane, M. Yokoyama, M. Takenaka and S. Takagi, “Steep Slope Ge-Source Tunnel FETs with Biaxial Tensile Strain Si Channels”, 7th International Workshop on New Group IV Semiconductor Nanoelectronics and JSPS Core-to-Core Program Joint Seminar, "Atomically Controlled Processing for Ultra large Scale Integration, O-2, Research Institute of Electrical Communication of Tohoku University, Sendai, Japan, January 27-28, 2014.

[14]（口頭、査読あり）○M. Kim, Y. Wakabayashi, R. Nakane, M. Yokoyama, M. Takenaka and S. Takagi, “Effect of in-situ boron doping in germanium source regions on performance of germanium/strained-silicon-on-insulator tunnel field-effect transistors”, 2014 Material Research Society (MRS) Spring Meeting, BB2.01, Moscone West Convention Center, San Francisco, California, USA, April 21-25, 2014.

[15]（口頭、査読なし）○M. Kim, Y. K. Wakabayashi, R. Nakane, M. Yokoyama, M. Takenaka and S. Takagi, “Effects of strain, interface states and back bias on electrical characteristics of Ge-source UTB strained-SOI tunnel FETs", 8th International Workshop on New Group IV Semiconductor Nanoelectronics and JSPS Core-to-Core Program Joint Seminar, "Atomically Controlled Processing for Ultra large Scale Integration", O-01,Tohoku University, Sendai, Jan. 29-30, 2015.

Domestic conferences in Japan related to this study

[1] (口頭、査読なし) ○若林勇希, 伴芳祐, 大矢忍, 田中雅明, “IV族強磁性半導体GeFe薄膜におけるアニールによる強磁性ナノ微粒子の形成”, 第74回応用物理学会秋季学術講演会, , 17a-C15-7, 同志社大学, 2013年9月16日-20日

[2] (ポスター、査読なし) ○若林勇希, 伴芳祐, 大矢忍, 田中雅明, “IV族強磁性半導体GeFe薄膜におけるキュリー温度及び格子定数の成長温度依存性”, PASPS18, P-4 大阪大学, 2013年12月9日-10日

[3] (ポスター、査読なし) ○若林勇希, 伴芳祐, 大矢忍, 田中雅明, “Growth temperature dependence of the properties including the Fe-atom locations in ferromagnetic-semiconductor GeFe”, 第75回応用物理学会春季学術講演会, 17a-E7-56, 青山学院大学, 2014年3月17日-20日

[4] (ポスター, 査読なし) ○若林勇希, 伴芳祐, 大矢忍, 田中雅明, “IV族強磁性半導体

GeFeの特性 ： 成長温度依存性, Fe原子とその磁性への影響”, ナノ量子情報エレクトロニクスの新展開, 東京大学本郷キャンパス, 2014年5月19日-20日

[5] (口頭、査読なし) ○若林勇希, 伴芳祐, 大矢忍, 田中雅明, “Structural analysis of group-IV-based ferromagnetic semiconductor GeFe by MeV-ion channeling”, 第75回応用物理学会秋季学術講演会, 20a-S10-1, 北海道大学 札幌キャンパス, 2013年9月17日-20日

[6] (ポスター、査読なし) ○Y. K. Wakabayashi, S. Sakamoto, K. Ishigami, Y. Takahashi, Y. Takeda, Y. Saitoh, H. Yamagami, A. Fujimori, M. Tanaka, and S. Ohya, “Local magnetic behavior in ferromagnetic semiconductor GeFe studied by soft X-ray magnetic circular dichroism”, 第19回半導体スピン工学の基礎と応用 (PASPS-19), P-7, 東京大学 武田ホール, 2014年12月15日-16日

[7]（口頭、査読なし）○Y. K. Wakabayashi, S. Sakamoto, K. Ishigami, Y. Takahashi, Y. Takeda, Y. Saitoh, H. Yamagami, A. Fujimori, M. Tanaka, and S. Ohya, “Room-temperature local ferromagnetism and its nanoscale domain growth in the ferromagnetic semiconductor $\mathrm{Ge}_{1-x}\mathrm{Fe}_x$”, 2015年春季応用物理学会, 14a-D2-4, 東海大学 湘南キャンパス, 2015年3月11日-14日

[8] (口頭、査読なし) ○坂本祥哉, 若林勇希, 竹田幸治, 藤森伸一, 鈴木博人,伴芳祐, 山神浩志, 田中雅明, 大矢忍, 藤森淳, “軟X線角度分解光電子分光による強磁性半導体$\mathrm{Ge}_{1-x}\mathrm{Fe}_x$の電子構造の解明”, PASPS18, P-4 東北大学, 2015年12月3日-4日

[9] (口頭、査読なし) ○坂本祥哉, 若林勇希, 竹田幸治, 藤森伸一, 鈴木博人,伴芳祐, 山神浩志, 田中雅明, 大矢忍, 藤森淳, “軟X線角度分解光電子分光による強磁性半導体$\mathrm{Ge}_{1-x}\mathrm{Fe}_x$の電子構造の解明”, 第29回日本放射光学会年会放射光科学合同シンポジウム, 6E005 東京大学 柏の葉キャンパス, 2016年1月9日-11日

[10]（口頭、査読なし）○K. Okamoto, Y. K. Wakabayashi, W. Ashihara, Y. Ban, S. Sato, M. Tanaka, S. Ohya, “Observation of tunneling magnetoresistance in trilayer structures composed of group-IV ferromagnetic semiconductor Ge1-xFex, MgO, and Fe”, 2016年春季応用物理学会, 20a-W241-11, 東京工業大学 大岡山キャンパス, 2016年3月19日-22日

[11]（口頭、査読なし）○Y. Wakabayashi, R. Akiyama, Y. Takeda, M. Horio, G. Shibata, S. Sakamoto, Y. Ban, Y. Saitoh, H. Yamagami, A. Fujimori, M. Tanaka, S. Ohya, “Origin of the large magnetoresistance in $\mathrm{Ge}_{1-x}\mathrm{Fe}_x$ granular films”, 2016年秋季応用物理学会, 14p-C41-3, 新潟コンベンションセンター, 2016年9月13日-16日

Other domestic conferences

[12] (口頭、査読無し) ○藤原秀紀, 若林勇希, 他11名, ”軟顕微X線角度分解光電子分光

による V2O3 のバンド構造の観測”, 日本物理学会第 67 回年次大会, 24pPSA-4, 関西学院大学, 2012 年 3 月 24 日

[13]（ポスター、査読なし）○M. Kim, Y. Wakabayashi, R. Nakane, M. Yokoyama, M. Takenaka and S. Takagi, “Electrical Characteristics of Ge/Si Hetero-Junction Tunnel Field-Effect Transistors and their Post Annealing Effects”, 2013 年秋季応用物理学会, 19a-P5-12, 同志社大学京田辺キャンパス, September 16-20, 2013

[14]（ポスター、査読なし）○M. Kim, Y. Wakabayashi, R. Nakane, M. Yokoyama, M. Takenaka and S. Takagi, “Type-II Staggered Hetero-Junction Tunnel FETs with Ge sources and Biaxial Tensile Strain Si Channels”, 2014 年春季応用物理学会, 19p-PG4-4, 青山大学院大学 相模原キャンパス, March 17-20, 2014

[15] (口頭、査読なし) ○M. Kim, Y. Wakabayashi, R. Nakane, M. Yokoyama, M. Takenaka and S. Takagi, “Ge/Si Hetero-Junction TFETs with In-situ Boron-Doped Ge-Source”, 2014 年秋季応用物理学会, 北海道大学 札幌キャンパス, 2013 年 9 月 17 日-20 日

[16]（口頭、 査読なし）○M. Kim, Y. K. Wakabayashi, R. Nakane, M. Yokoyama, M. Takenaka and S. Takagi, “Effects of strain, interface states and back bias on electrical characteristics of Ge-source UTB strained-SOI tunnel FETs”, 2015 年春季応用物理学会, 11a-A23-19, 東海大学 湘南キャンパス, 2015 年 3 月 11 日-14 日

[17]（口頭、査読なし）○Akiyori Yamamoto, Tomonari Yamaguchi, Ryo Ishikawa, Ryota Akiyama, Yuki K. Wakabayashi, Shinji Kuroda, Shinobu Ohya, Masaaki Tanaka, “Spin injection into the topological crystalline insulator SnTe using spin pumping”, 2015 年秋季応用物理学会, 14p-2J-18, 名古屋国際会議場, 2015 年 9 月 13 日-16 日

[18]（口頭、査読なし）○A. Yamamoto, T. Yamaguchi, R. Ishikawa, R. Akiyama, Y. K. Wakabayashi, S. Kuroda, S. Ohya, M. Tanaka, “Temperature dependence of the electromotive force in the topological crystalline insulator SnTe induced by spin pumping”, 2016 年春季応用物理学会, 21p-W241-12, 東京工業大学 大岡山キャンパス, 2016 年 3 月 19 日-22 日

[19]（口頭、査読なし）○芦原 渉, 若林 勇希, 岡本 浩平, 田中 雅明, 大矢 忍, “半導体からのキャリア注入による強磁性量子井戸におけるトンネルキャリアのスピン分極率の変調”, 2016 年春季応用物理学会, 19p-P1-57, 東京工業大学 大岡山キャンパス, 2016 年 3 月 19 日-22 日

[20]（口頭、査読なし）○S. Sakamoto, T. T. Nguyen, Y. Takeda, S.-i. Fujimori, N. H. Pham, D. A. Le, Y. Wakabayashi, G. Shibata, M. Horio, K. Ikeda, Y. Saitoh, H. Yamagami, M. Tanaka, A. Fujimori, “Electronic Structure of the p-type Ferromagnetic Smiconductor (Ga,Fe)Sb”, 2016 年秋季応用物理学会, 14a-C41-10, 新潟コンベンションセンター, 2016 年 9 月 13 日-16 日